

**Transition Metal-based Bimetallic MOFs and MOF-derived Catalysts for Electrochemical Oxygen Evolution Reaction**

Journal:	<i>Energy & Environmental Science</i>
Manuscript ID	EE-REV-11-2020-003697.R1
Article Type:	Review Article
Date Submitted by the Author:	11-Feb-2021
Complete List of Authors:	Li, Songsong; China University of Petroleum Beijing, Gao, Yangqin; China University of Petroleum Beijing, Department of Materials Science and Engineering Li, Ning; China University of Petroleum Beijing, College of New Energy and Material; China University of Petroleum Beijing, State Key Laboratory of Heavy Oil Processing Ge, Lei; China University of Petroleum Beijing Bu, Xianhui; California State University, Long Beach, Dept of Chemistry and Biochemistry Feng, Pingyun; University of California, Department of Chemistry

Transition Metal-based Bimetallic MOFs and MOF-derived Catalysts for Electrochemical Oxygen Evolution Reaction

Songsong Li ^{a,b}, Yangqin Gao ^a, Ning Li ^a, Lei Ge ^{a,*}, Xianhui Bu^c, Pingyun Feng ^{b,*}

^a State Key Laboratory of Heavy Oil Processing, College of New Energy and Materials, China University of Petroleum Beijing, No. 18 Fuxue Rd., Beijing 102249, People's Republic of China.

^b Department of Chemistry, University of California, Riverside, California 92521, United States.

^c Department of Chemistry and Biochemistry, California State University Long Beach, Long Beach, CA 90840 (USA).

Abstract Oxygen evolution reaction (OER) is a critical electrochemical reaction in water-splitting and rechargeable metal-air batteries. It plays a pivotal role in achieving high-efficiency clean-energy production and energy storage in these devices. Transition metal-based bimetallic MOFs (TMB MOFs) with two different metal ions possess specific synergistic effect, which could exhibit OER performance and stability superior to corresponding monometallic MOFs for water oxidation. Benefitting from the diversity of chemical composition and structural type, TMB MOFs can also serve as precursor and template to obtain alloy-particle decorated carbon materials with high surface area, or metal compounds such as bimetallic sulfides, phosphides, and hydroxides with atomic-level mixing of heterometallic elements. These materials with high-density active sites exhibit much improved catalytic activity in water oxidation reaction. This article aims to review the recent progress of TMB MOFs and their derivatives in relation to applications as electrocatalysts in OER, including analysis of mechanism of the OER process with assistance of DFT calculations and *in situ* or *operando* techniques.

1. Introduction

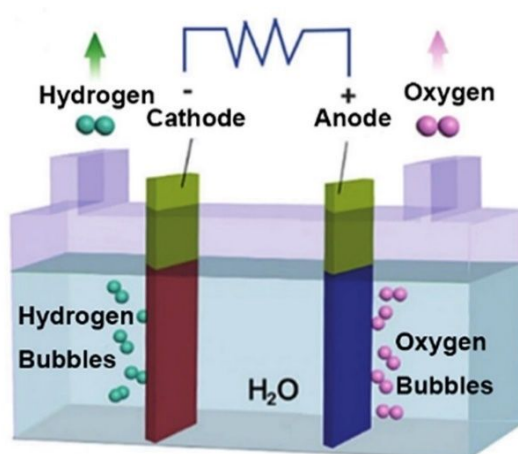


Fig. 1. Schematic illustration of electrocatalytic reactions in water splitting electrolyzer.¹ Copyright © 2018 Elsevier Ltd.

In recent decades, it is extremely urgent to develop clean and sustainable energy on account of the increasing demand for clean energy as well as the solving the worsening environmental problems.² Water-splitting electrocatalysis is among the most effective and sustainable avenue for generating clean and green energy.³ As shown in Fig. 1,¹ water splitting ($\text{H}_2\text{O} \rightarrow \text{H}_2 + 1/2\text{O}_2$) is an important electrochemical reaction, and it encompasses two half electrode reactions: hydrogen evolution reaction (HER) and oxygen evolution reaction (OER). The four-electron-transfer process involved in the OER both in acidic electrolyte and basic electrolyte leads to sluggish reaction kinetics and larger overpotential and it is the bottleneck of the water-splitting reaction.^{4,5}

Many potentially high-efficient electrocatalysts

have been studied for OER with lower energy barriers. At present, noble-metal oxides such as IrO_2 and RuO_2 are state-of-the-art electrocatalysts for OER and show excellent electrocatalytic activity and stability. Nevertheless, the problems such as prohibitive cost, limited durability, natural scarcity, as well as poor resistance to poisoning have restricted their large-scale commercial applications.^{6,7} Although a plethora of efforts have been made to develop cost-effective OER catalysts, current electrocatalysts still do not satisfy the industrial requirements. The development of efficient electrocatalysts for OER, especially the use of non-noble metal electrocatalysts for OER with high catalytic activity and stability, remains challenging. Among different non-noble-metal electrocatalysts, the first-row transition metals, such as Ni, Co, and Fe, have shown great promise for efficient

electrocatalytic activity toward OER and have therefore attracted great attention in recent years.^{8,9}

In the search for efficient electrocatalytic materials for OER, large specific surface area, high porosity, optimized active site (often defined as the intrinsic activity of the catalyst) distribution, and high charge transfer capability are all important factors.¹⁰⁻¹² These factors play important roles in maximizing electron transfer and promoting the mass transport of reactants.¹³ Among various emerging candidates, metal-organic frameworks (MOFs) show great promising. MOFs are a family of porous coordination polymers constructed by organic ligands and metal centers through coordination bonds. MOFs are considered as promising electrocatalytic materials¹³⁻¹⁵ due to their tunable porosity, large surface area and flexibility to be functionalized with various ligands and metal centers.¹⁰ The high porosity and accessible surface area of MOFs can greatly reduce the diffusion distance of charge carriers to the reactants in the process of electrocatalysis.¹⁶ Considering the highly accessible metal-ligand junctions, the interfacial electronic coupling interaction in MOFs has been recognized as one of the important factors for the improvement of efficiency of the redox reaction in water splitting process.¹² Herein, the rational combination of specific redox active metal nodes and organic ligands could furnish a pathway to connect electro-active components and provide the MOFs

with desirable electrocatalytic functionality.

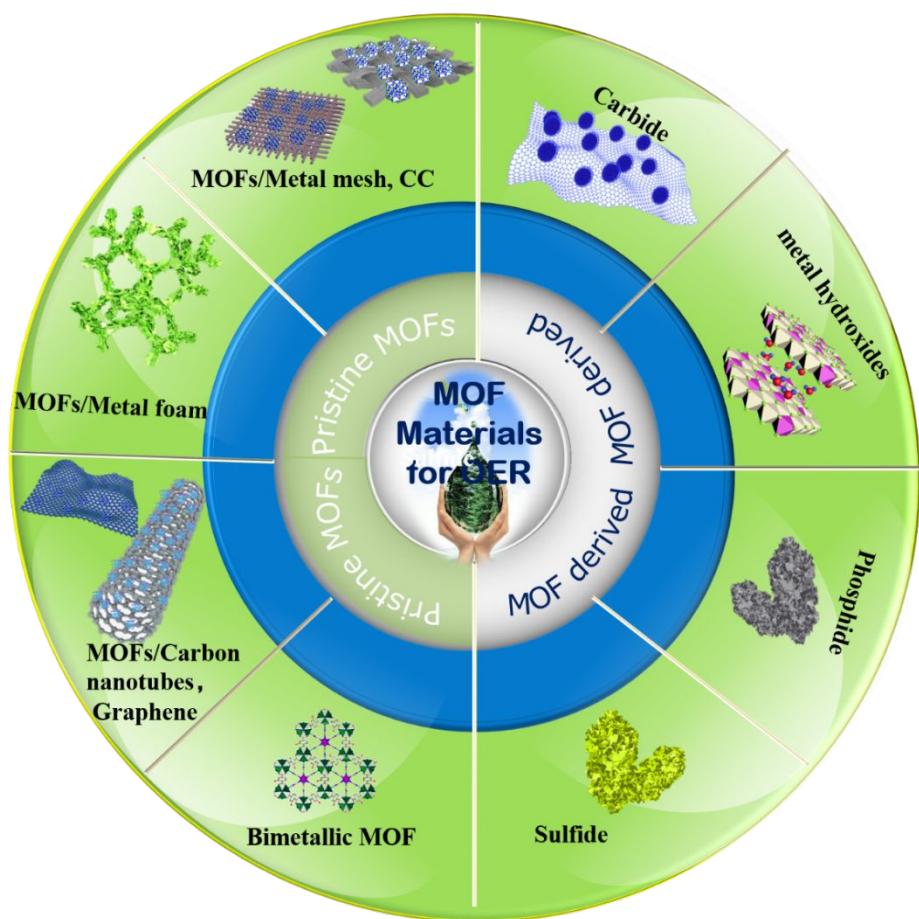
Because of these advantages, MOFs have aroused enthusiastic interest and have been studied as electrocatalytic materials.^{17, 18} Some of the most important strategies to design catalysts from MOFs are illustrated as follows (Scheme 1): (1) increasing the exposure of electrochemical catalytic active sites by engineering the morphology of MOF materials;⁴ (2) in-situ growth of MOFs on the substrate with a high surface area or reducing the size of particles to increase the surface area;¹⁹⁻²¹ and (3) adopting bimetallic or multivariate MOFs.²²

Compared with monometallic MOFs, most of bimetallic MOFs, such as NiFe-MOFs,²³⁻²⁵ NiCo-MOFs,¹⁸ FeCo-MOFs,^{26, 27} exhibit better electrocatalytic oxygen evolution reaction activity which can be ascribed to the synergistic effect between different metals and the adjustable metal node engineering. Metal substitution on the metal nodes in MOFs can have advantages in tuning the materials stability, flexibility, and electronic structures. The formed bimetallic MOFs can strengthen the valence state of metal sites and optimize the e_g orbitals, which plays an important role in improving the catalytic performance.^{28,29} For example, Tang's group reported ultrathin NiCo-MOFs nanosheets as electrocatalyst toward OER in alkaline conditions.³⁰ The valence electronic configuration of Co^{2+} in NiCo-MOFs is $3d^7$ with high-spin state. Theoretically, Co^{2+} has unpaired

electrons in π -symmetry (t_{2g}) d-orbitals, which could interact with the bridging O_2 via π -donation. While, the t_{2g} orbitals of Ni^{2+} are fully occupied, so the e^- - e^- repulsion is the main interaction between O^{2-} and Ni^{2+} . When coupling Ni^{2+} and Co^{2+} together, the π -donation through Co-O can be enhanced by the e^- - e^- repulsion between O^{2-} and Ni^{2+} in NiCo-MOF ultrathin nanosheets, which results in partial charge transfer from Ni^{2+} to Co^{2+} . In addition, the PDOS (partial density of states) of the unfilled $3d e_g$ -orbitals for bimetallic NiCo-MOFs are also changed, which indicates that the electron density of the unoccupied e_g states increases. So the coupling of Ni and Co induces the change of e_g and further improves the OER activities. Similarly, Zhu and co-workers verified this synergistic effect between Fe and Co metal ions in FeCo-MOF nanosheets as well.³¹ The synergistic interaction between Co and Fe atoms also endowed the FeCo-MNS-1.0 with an excellent OER performance. Verified by DFT calculation and experimental results, the coupled metal ions led to efficient orbital hybridization and optimized the electrocatalytic activities. Lou's group³² also revealed the existence of strong synergistic effect of adjacent Ni and Mn nodes within MCCF/NiMn

MOFs by X-ray absorption structure spectroscopy and DFT calculations. According to the DFT calculations, as for mono-metallic Ni-MOFs, there is no electron density around the Fermi level. After incorporation of Mn, obvious electron density around the Fermi level of NiMn-MOFs increases, which mainly due to the hybrid of Ni 3d and O 2p orbits, rather than Mn and O. However, the dominant of 3d orbital band of Mn locates far away from the Fermi level, which implies Mn sites act as favorable electron acceptors. In addition, the formation energy barriers of key *O and *OOH intermediates in NiMn MOFs all are lower than that in Ni-MOFs, indicating that the synergistic effect between neighboring Ni and Mn nodes can accelerate the proton-coupled electron transfer kinetics so as to improve OER activities. Therefore, the introduction of synergistically active sites in MOFs combines with rational architectural design can increase active sites, facilitate the charge transfer, and improve water oxidation efficiency.

It is known that powdery electrodes can only work under a small current density (usually ≤ 100 mA cm⁻²), and cannot meet the requirement of practical application that are often operated under



Scheme 1 An overview of MOF-based materials for oxygen evolution reaction.

high current densities.^{33, 34} One effective strategy is to adopt self-supported electrodes in which catalytically active phase are in-situ grown on the conductive substrates, such as metal foam (e.g., Ni, NiFe, Cu foam), metal mesh (e.g., Ti/Cu mesh), carbon cloth (CC), graphene, metal plates, and fluorine-doped tin oxide (FTO). By growing MOFs directly on the conductive substrates, the seamless contact between MOF catalysts and conductive substrates could ensure rapid charge transfer and prevent the shedding of catalysts as well. Wherein nickel foam has been widely applied as the

conductive and microporous substrate for OER electrocatalysts for its large surface area, superior electroconductivity, and excellent mechanical strength.³⁵ In 2020, Xie's group³⁶ prepared Co/Fe-imidazole-based bimetal-organic framework nanosheet arrays using nickel foam as the substrate to probe its OER activities. Nickel-iron foam (NFF) is considered as an ideal catalyst supporting material, it could be activated by acidification method and then the activated metal ions in NiFe foam can serve as the metal sources for in situ synthesis of NiFe bimetal-organic frameworks.³⁷ The experimental

result suggested that the activated NiFe foam accelerated charge transport and separation efficiency, which can be attributed to its high uniform dispersed metal sites, high porosity, and an ordered 3D skeleton structure, further benefited in improving electrochemical properties. Carbon fibers is a highly conductive carbon-matrix support with multi-channels, and it is a powerful tool for addressing poor electroconductivity of MOFs. In 2020, Lou's group³² developed a transformation method for in situ growing NiMn-based bimetal-organic framework nanosheets array on carbon fibers and supported it as a promising bifunctional oxygen electrocatalyst. Moreover, a novel material of graphene-nanoplates-supported (Ni, Fe) metal-organic frameworks (MOFs) could also be decorated on the carbon-fiber paper electrodes working for alkaline water electrolysis, this work also helped in developing a durable, high-property alkaline anion exchange membrane for water electrolysis and direct solar-to-fuels conversion method to replace the expensive proton-exchange membrane in water electrolysis that worked with ultra-pure water.³⁸ The conductive carbon cloth^{39, 40}, carbon nanotubes⁴¹, and other carbon materials were also been widely applied as the substrates to direct growth of MOF electrocatalysts with high mechanical stability and conductivity.

In addition to many merits of using pristine MOF catalysts in electrocatalysis, these MOFs can

also be used as outstanding precursors for the fabrication of various alloys, metal oxide-carbon composites, metal phosphides, metal selenides or pure carbon materials with rich morphological structures and versatile properties.⁴²⁻⁴⁴ The most dazzling merits of MOF-derived materials is that the carbon skeleton is an essential factor to boost the OER process not only due to the high electroconductivity but also due to the possibility of stabilizing transition metal atoms on the carbon substrates leading to single-atom TM-N-C catalysts (TM = Fe, Co, Ni, *etc.*).^{45, 46}

Recently, remarkable progress has been achieved in the development of bimetallic MOF-based catalysts as electrodes for electrocatalytic oxygen evolution reaction, ranging from pristine MOFs and MOF-derived porous carbons to transition metal-based materials. Although there are a number of reviews summarizing MOFs and their derivatives in terms of the catalytic performance of OER, few of them focuses specifically on the discussion of transitional metal-based bimetallic (TMB) (Ni, Fe and Co) MOFs and provides detailed analysis on the use of advanced techniques to uncover the mechanism toward taking full advantage of active sites. This review will provide an overview of recent advances of using TMB MOFs as OER electrocatalysts, and will mainly focus on their structures, compositions, and OER performances. With the assistance of progressive characterization

techniques and theoretical calculations, mainly based on density functional theory (DFT) and *in situ* or *operando* technique analysis to illustrate the actual active sites, heteroatom doping effect and phase evolution during the process of OER activity have been elucidated to uncover the reaction mechanism. Meantime, the current challenges and obstacles of using TMB MOFs and their derivatives as electrodes will be highlighted. Finally, the future outlooks will be proposed for designing more effective and promising TMB MOF-based materials toward oxygen evolution reactions.

2. Simple Rationale, Evaluation Parameters and Influencing Factors of Oxygen Evolution Reaction.

Before introducing recent progress in the study of TMB MOFs as electrocatalysts, we will first illustrate the reaction mechanism and measurement criteria for OER process, which can provide an in-depth understanding of OER process and a standard protocol of measurements. The detailed mechanism will be discussed in part IV and in combination with DFT calculation and *in situ* or *operando* techniques.

2.1 The Simple Reaction Mechanisms and Influencing Factors of OER

Oxygen evolution is a result from the oxidation reaction of hydroxide group in alkaline solution or water molecule under the acid electrolyte.³⁴ The

pathways in acidic and alkaline media including elementary steps are different according to different mechanisms. Yet both conditions involve the adsorption and desorption of intermediates, such as HO*, O* and HOO*.⁴⁷

In the research of Rossmeisl et al., the free energies of adsorption of the OER intermediates at select electrodes of Pt (111), Au (111), and other metals were discussed in detail in acidic environment. The most difficult step in the OER process is the formation of HOO* by splitting water on an adsorbed O*. This step is downhill in free energy at high electrode potentials, however, at the lower potentials, the OER is triggered only on the oxidized surface even though the water can dissociate to O*. This is why this step is slower than that of O* formation step.³

Electricity is commonly used as energy input to drive the electrochemical reaction for OER since OER is an electron-coupled uphill reaction due to every O₂ molecule generation requires transfer of four electrons. This multiple electron transfer process is not kinetically favorable.⁴⁸ The accumulation of energy barriers in each step results in a sluggish kinetics of OER, and as a result, it needs to overcome the large overpotential. The standard potential of OER under the condition of pH=0 is 1.23 V vs. NHE, and E is proportional to the pH by shifting 59 mV for per pH unit increase.

Since OER is the bottleneck reaction of

electrocatalytic water splitting, unremitting efforts have been made in order to acquire the lower overpotential electrocatalysts. So far, the intrinsic properties affecting OER efficiency often refer to some extrinsic and intrinsic properties of materials. The extrinsic properties mainly refer to the morphology of the catalysts, state of electrolyte and the choice of the substrates.⁴ In order to achieve the ideal properties, for example, researchers tend to construct nano-sized, layered or highly open structure in order to expose more active sites for activity improvement.⁴⁹ Moreover, other methods to improve the electroconductivity of the catalysts include dispersion of the catalysts onto high surface area substrates to enhance the catalytic activity, for example, in-situ growth of the catalysts on the conductive and porous substrates such as Ni foam, carbon cloth, metal plates, and carbon nanotubes⁵⁰⁻⁵². Such approaches can effectively enhance the stability of the strong bonding between the catalysts and substrates to accelerate the electron transfer during reactions.

The intrinsic properties involve the number of active sites, charge transfer capability and electroconductivity.^{3, 4} However, the intrinsic properties are usually largely dependent on the extrinsic properties. The number of active sites can be increased by constructing high-surface-area structures, using preparation methods such as annealing, acid leaching, ball-milling, as well as

plasma etching to fabricate the nanostructured electrocatalysts. It is also helpful to synthesize 2D and 3D porous materials to increase and expose more active sites.⁵³⁻⁵⁶ Moreover, apart from the extrinsic properties discussed above, the charge transfer ability and electronic electroconductivity of materials are also essential for achieving high electrocatalytic property for water splitting. Therefore, the extrinsic and intrinsic properties should both be considered in the design of the highly efficient electrocatalysts.

2.2 The Electrocatalytic Kinetics Parameters for OER

The benchmarking methodologies to evaluate the OER electrocatalytic activity mainly based on some specific kinetic parameters, such as: overpotential (η), Tafel slope (b), exchange current density (i_0), electrochemically active surface area (ECSA) and so on.⁵⁷ These parameters play vital roles in elucidating and understanding the reaction mechanism to a certain extent. A summary of these kinetic parameters is provided in the following subsections.

2.2.1 Overpotential (η)

Overpotential (η) is one of the most important descriptors to evaluate the OER performance of the target electrocatalyst under the same test conditions. It is defined as the potential gap between the

electrode potential and the equilibrium potential (1.23 V vs. RHE) of the electrode reaction when the electrode reaction is out of equilibrium. According to the Nernst equation in Eqn. (2.3),⁵⁸ where E is the real applied potential, E^0 is the standard electrode potential, R is gas constant (8.31441J/(mol * K)), T is the absolute temperature, n is the number of transferred electrons in a battery reaction, C_O and C_R stand for the concentrations of the oxidized and reduced reagents, respectively, the overpotential (η), is the gap of E and equilibrium potential E_{eq} , which is illustrated in Eqn. (2.4). The value of η is a benchmark to evaluate the performance of the catalysts under a specified current density, and commonly, a lower value indicates better electrocatalytic activity. Universally, the specific current density is 10 mA cm⁻² (indicated as i_{10}), which is the current density normalized to the geometric area of the electrode, and the overpotential value is defined as η_{10} . The historical origin of η_{10} is that the current density expected in solar water-splitting cells that possess a solar-to-fuel conversion efficiency of 10% under 1 sun illumination is approximate to 10 mA cm⁻² and it is also considered as the benchmark for evaluating solar-to-fuel device performance.⁵⁹ However, η_{10} is not considered as an absolute accurate activity metric of reflecting the intrinsic electrocatalytic performance for the following reasons. First, η_{10} is predominantly dependent on the catalysts loading mass. It is widely

proved that the higher loading mass gives an earlier onset potential, corresponding to the obtainment of 10 mA cm⁻² at a smaller overpotential. Secondly, the value of η_{10} is also based on the current density normalized to the geometric area of electrode. However, the experimental process usually neglects that the electrocatalysis reaction is just a surface process, which means that only surface atoms can participate in the activity. So it is necessary to normalize the electrocatalyst loading mass and a quantified parameter about the catalyst surface.⁶⁰⁻⁶³

$$E = E^0 + \frac{RT}{nF} \ln \frac{C_O}{C_R} \quad (2.3)$$

$$\eta = E - E_{eq} \quad (2.4)$$

2.2.2 Exchange Current Density (i_0) and Tafel Slope (b)

The other two substantive indicators for electrocatalytic kinetics are exchange current density (i_0) and Tafel slope (b). The exchange current density reflects the intrinsic transfer efficiency of electrons between electrode and electrolyte.⁶⁴ A specific electrochemical reaction consists of two-half reactions, which are cathode and anode reaction, respectively. In this regard, the overall current (j) is composed of anodic (j_a) and cathodic (j_c) current, the Eqn (2.5) is presented below.

$$j = j_a + j_c \quad (2.5)$$

j_0 is the magnitude of intercepts when the reaction is at the equilibrium condition, i.e., the value of $\eta=0$ and $E=E_{eq}$ (Eqn. 2.4). In this case, the absolute value

of anodic (j_a) and cathodic (j_c) current is equal, and obviously the overall current is zero without net electrolysis. Normally, the exchange current density (i_0) is the ratio of the current (j_0) to the electrode area (s), which is presented in Eqn. (2.6)

$$i_0 = j_0/s \quad (2.6)$$

The i_0 cannot be obtained by the electrochemical method, but it can be calculated by the Tafel equation as illustrated in Eqn. (2.11). Notably, the higher i_0 corresponding to the better electrocatalyst. The Butler-Volmer equation (Eqn. 2.7) in the following shows an in-depth understanding of the current density and the applied overpotential.

$$i = i_0 \left[\exp\left(\frac{\alpha_a n F E}{RT}\right) + \exp\left(\frac{\alpha_c n F E}{RT}\right) \right] \quad (2.7)$$

Where i_0 is the exchange current density, α_a and α_c represent the anodic and cathodic current transfer coefficient, respectively. The parameters of n , F , E , R , T are the same as those in Eqn. 2.3 and 2.4.

Furthermore, the overall current in the high anodic overpotential is mostly from the anodic current, and so the cathodic current is approximate to 0. Logically, Butler-Volmer equation can be depicted as Eqn. 2.8, which is the famous Tafel equation.⁶⁵

$$i \approx i_0 \exp\left(\frac{\alpha_a n F \eta}{RT}\right) \quad (2.8)$$

The Tafel equation in Eqn. (2.8) can be simplified using the logarithmic function, which is presented as Eqn. (2.9) below:

$$\log i = \log i_0 + \frac{\alpha_a n F \eta}{RT} \log(e) \quad (2.9)$$

$$\log i = \log i_0 + \frac{\eta}{b} \quad (2.10)$$

Because α_a , n , F , R , T are constants, $2.303RT/\alpha_a F$ can be simplified as a constant b . The Eqn. (2.9) can be re-written as Eqn. (2.10), and the Eqn. (2.10) can be further converted to another form as Eqn. (2.11).

$$\eta = a + b \log(i) \quad (2.11)$$

Where $a=2.303RT \log i_0/\alpha_a F$, $b=2.303 RT/\alpha_a F$. We can clearly see that the b is inversely proportional to the current (i), and is proportional to overpotential (η). Logically, when at the same current density, the smaller value b , corresponds to the lower overpotential (η), which indicates the higher electrocatalytic kinetics.⁴⁸ What's more, the polarization of the electrode reflects the obstruction of the electrode process, which correlates with the overpotential and the current density in a logarithmic manner. Indeed, the Tafel slope is an indicator implying the rate-determining step especially in the range of onset overpotential.⁴⁸ For example, usually if the first step in OER procedure is the rate-determining step, the corresponding Tafel slope will be around 120 mV dec⁻¹, which indicates the rate-controlling step in the electrocatalytic reaction is decided by one-electron transfer step. And the second step will be more complicated, if it is the chemical step, the calculated value of Tafel slope will be about 60 mV dec⁻¹, while if it is an electron-proton reaction, the value maybe approximately to 40 mV dec⁻¹. The condition will be further complicated for the third and the fourth step in the

existing models.⁶⁶

2.2.3 Turnover Frequency (TOF) and Electrochemically Active Surface Area (ECSA)

Using Tafel slope (b) only to evaluate the performance of electrocatalysts would be inaccurate because the value obtained by calculation from the plot tends to have non-negligible errors. The turnover frequency (TOF) represents the intrinsic catalytic activity of the catalyst, which is defined as the number of conversions at per unit catalytic active sites of the reactant molecule. TOF can be calculated by the *Eqn. 2.12* for an electrocatalytic reaction:

$$TOF = j * N_A / AnF\Gamma \quad (2.12)$$

Where j is the current, N_A is the Avogadro constant (6.02×10^{23}), A is the geometrical surface of the electrode, n represents the number of electrons involved in the reaction, F is Faraday constant, Γ is the surface concentration. It is necessary to note that the nature of the active sites of the electrocatalysts have not been clearly understood especially in solid-state heterogeneous electrocatalysts. In these cases, only the metal sites directly involved in the in situ redox reaction are considered as active sites.^{67, 68}

Before introduction of electrochemically active surface area (ESCA), we need to know that the OER catalysts can act as capacitors at the film/electrolyte interface.⁶⁹ Therefore, it is a valid method by measuring the value of the double-layer capacitances

C_{dl} to obtain the electrochemically active surface area, which is generally proportional to the C_{dl} of the electrocatalysts. This method can only be used under the condition that the catalyst is electrically conductive with a well-defined solid/electrolyte interface or when an alternate technique is viable for confirming the amount of electrochemically active materials.⁶⁹ The most prevalent strategy to measure the C_{dl} is cyclic voltammogram (CV) measurements.^{24, 70} The C_{dl} can be defined as the following *Eqn. 2.13*:

$$C_{dl} = \frac{dQ}{dE} = \frac{i_{dl}}{\nu} \quad (2.13)$$

Where ν is the scan rate, i_{dl} is the double-layer charging current. Notably, in order to avoid the Faraday current, it is necessary to choose the voltage range in which no redox reaction occurs when testing the cyclic voltammetry. And the obtained CV curve should be a rectangular shape.^{71, 72} The evaluation method and the result of ECSA often depend on electrochemical reactions and the materials, so it cannot be used as an accurate metric to compare different electrocatalysts under the different conditions. Instead, it is feasible to use it to evaluate the performance of a series of similar materials under the same conditions.

2.2.4 Stability

For the electrocatalysts, besides super activity, excellent stability is also a significant metric for evaluating the quality of catalysts.⁷³ Most of the

reported non-noble-metal-based materials show excellent stability in alkaline solutions.^{74, 75} According to literatures, there are about three common methods to measure the stability of the electrocatalysts. One is cyclic voltammetry (CV) cycling (usually over 1000 cycles)⁷⁶ which (after rapid CV cycling) compare the shift of the overpotential at a specific current density over the linear sweep voltammetry (LSV) curve with the original one. The other two methods are chronoamperometry ($I-t$ curve at a constant potential) and chronopotentiometry ($E-t$ curve at a fixed current density), respectively.

3. Recent Research Progress in TMB-MOF Based Catalysts for OER

In recent years, MOFs materials have attracted substantial research attention as OER catalysts owing to their outstanding features such as tunable pore sizes, rich morphology structures, high surface area, diverse chemical compositions and interesting optical and physical properties. In terms of these advantages, MOFs materials, especially transition-metal such as Ni, Co, Fe-based MOFs and MOF-based composite materials have experienced a fast growth as electrocatalysts for OER and other reactions, because they can provide abundant active sites to accelerate the electrocatalytic activity.³ Nevertheless, the inferior electroconductivity is still the bottleneck of the monometallic MOF materials

in the applications of electrocatalysis. One proven method of improving its performance is to modify their metal centers by introducing the secondary metal, which can also increase the electrochemically active areas, strengthen the valence state of metal sites and optimize the e_g orbitals, change charge transfer path, as well as modulate the electronic structure so as to enhance the catalytic performance toward OER.²⁴ Moreover, the incorporation of secondary metal nodes into the structure of MOF can induce abundant defects, and the synergistic effects between two different metal indeed enhance electroactive redox reaction. Besides, bimetallic MOFs with tunable chemical compositions and diverse structures can also be used as precursors or templates for synthesis of a variety of nanostructured materials. So, burgeoning efforts have been devoted to synthesizing bimetallic MOFs by engineering various fabrication methods. To synthesize bimetallic MOFs, two common strategies, one-step and the post-treatment method, have been adopted.⁷⁷⁻

80

3.1 Synthesis strategies of Bimetallic MOFs

For the synthesis of bimetallic MOFs, a convenient one-pot reaction method, which is the mixing of different metal salts during the solvothermal synthesis, has been used to prepare diverse forms of bimetallic MOFs. The possible disadvantages of the one-pot method could be the

unpredictable topologies and functions due to the uncontrollable random incorporation of the secondary metal into the MOFs. And this method is no guarantee for the formations of a solid-solution bimetallic MOF because of different reaction kinetics of different metals. So the accurate control of solubility, reactivity and coordination sphere of metal ions and pH value of reaction precursors are all important.⁸¹

Nevertheless a variety of bimetallic MOFs have been successfully obtained by the one-pot method. Fan's group successfully synthesized a series of functionalized bimetallic MOF catalysts by one-pot reflux method with various $\text{Al}^{3+}/\text{Fe}^{3+}$ molar ratio. The obtained bimetallic MOFs were assembled by 2-amine-1,4-benzenedicarboxylate ligands and trimeric $\text{Al}^{3+}/\text{Fe}^{3+}$ octahedral clusters. Serre and co-workers first synthesized mixed Fe(III)/M(II) (M=Ni, Co, Mg) polycarboxylate porous MOFs based on the Secondary Building Unit (SBU) approach. By using oxo-centered trimeric mixed $\text{Fe}^{3+}/\text{M}^{2+}$ as building blocks, various mixed-metal MIL-127 MOFs with tailored properties were prepared.⁸² In addition, in order to regulate and control the metal stoichiometry, a series of bimetallic MOFs that used In-M (M= Co, Mg, V, etc.) clusters as inorganic building blocks have also been synthesized, which exhibit different metal-to-metal ratios, morphologies, and charges.⁸³

The post-synthesis modification aims to insert a functional group or make selective exchange of

metal ions in the framework to improve their specific properties or broaden their application with slightly change of the lattice structure.⁸⁴⁻⁸⁵ Bimetallic MOFs have been fabricated by post-synthetic metal ions exchange in many cases.^{86,87} However, the synthesis rate of bimetallic MOFs by post-synthesis method is much lower than that the direct one-pot synthesis process. Specifically, the mono-metallic MOFs should be prepared with high crystallinity in advance, following by the metal exchange procedure. The bimetallic MOFs are usually obtained by soaking the synthesized mono-metallic MOFs in the second metal solution for several days or by disposing the activated crystalline MOFs solvothermally in the suitable solution that contains the second metal.⁸⁸ Of course, the metal exchange happening between different metals must satisfy a condition that two metal ions have the similar ionic radius and coordination geometries.⁸⁹ Nevertheless, the post-treatment method is difficult to control the molar ratio of two metals in the materials. What's more, the exchange or the direct introduction of another metal ion would have to overcome the large kinetic barriers, which could result in incomplete exchange and unevenly distribution of the metals. In 2020, Kaskel and co-workers applied post-synthetic metal exchange method to exchange the metal centers of the paddle-wheel to synthesize DUT-49 (M) frameworks (M=Mn, Fe, Ni, Zn, and Cd).⁹⁰ According to the previous reports about synthesizing

DUT-49 (Cu), it seems there is a great challenge to direct fabricate DUT-49 framework with other bivalent metal nodes. Fortunately, DUT-49 (Co) could be synthesized easily. Authors take DUT-49 (Co) as the starting point, and further synthesize other DUT-49 (M) by post-synthetic metal exchange method. After activated cubic crystals of DUT-49 (Co) with NMP, then it is dipped into the solution that contains the corresponding metal salts. Based on the kinetics of the exchange, the second metal ions can be exchanged into the crystal, which can be verified by the visible color change of crystals. Liao's group also synthesized a water-, and alkaline-stable MOF [$\{\text{Fe}_2(\mu_3\text{-O})(\text{bdc})_3\}_4\text{-Co}_2(\text{na})_4(\text{L}^{\text{T}})_2$] crystals after two-step, single-crystal to single crystal and post-synthetic modification.⁹¹ In principle, the hypothetical metal carboxylate frameworks (MCFs), such as $\text{Fe}_3(\mu_3\text{-O})(\text{bdc})_3 (\text{L}^{\text{T}})_3$ isomers with 6-connected acs (MIL-88) and mtn-e (MIL-101) topology possess excellent chemical stability.^{92 93} However, their open metal sites (OMSs) have the ability to fix the multiple monodentate guests when properly arrange the clusters of $\text{Fe}_3(\mu_3\text{-O})(\text{RCOO})_6 (\text{L}^{\text{T}})_3$, so as to facilitate special chemical reactions or adjust multi-dentate ligand/metallo-ligands to prepare structurally decorated MOFs.⁹⁴ Herein, authors prepared a hybrid MOF [$\{\text{Fe}_2(\mu_3\text{-O})(\text{bdc})_3\}_4\text{-Co}_2(\text{na})_4(\text{L}^{\text{T}})_2$] by crossing-link the flu-e type $\text{Fe}_3(\mu_3\text{-O})(\text{bdc})_3 (\text{L}^{\text{T}})_3$ and $\text{Co}_2(\text{na})_4(\text{L}^{\text{T}})_2$. Rationally, due to the high chemical stability of

$\text{Fe}_3(\mu_3\text{-O})(\text{bdc})_3 (\text{L}^{\text{T}})_3$, $\text{Co}_2(\text{na})_4(\text{L}^{\text{T}})_2$ clusters may act as the electrocatalytic active sites. Actually, bimetallic MOFs can also be synthesized by template synthetic method and seed-induced method as well.

3.2 TMB Pristine MOF materials for OER

Transition metal-based compounds as active OER catalysts have been exploited since the last century. The renewed interest has been witnessed in recent years on developing advanced bimetallic based materials for the state-of-the-art OER catalysts especially on TMB-based MOF materials.⁹⁵ Considering the spatial architectures of MOFs, the high density of active sites could make it possible for reactants to easily transfer along the free energy environment and be converted to the desired products. The interaction energies between reactant, catalyst and product are the major factors to affect the rate of water splitting.¹² So a reasonable combination of redox active metal ions (such as Ni, Fe and Co) and organic linking agents provides a convenient pathway to connect the basic electro-active components into an infinite structure network with ideal electrochemical functions.

3.2.1 NiFe-based Pristine MOF Materials for OER

Many studies revealed that introduction of Fe into the Ni-based MOF materials can not only increase the electrochemical active sites but also

regulate the 3d orbital electron density for Ni ions to accelerate the electron transport, which attributes to improved OER catalytic activities.^{24, 96} For example, MIL-53 (NiFe)/NF (nickel foam) can be successfully synthesized by using the self-template route. As shown in Fig. 2a, the nickel foam serves as a substrate as well as nickel source and Fe ions are added exogenously. Both Fe and Ni ions link with terephthalic acid (TPA) to form MIL-53 (NiFe)/NF.²⁴

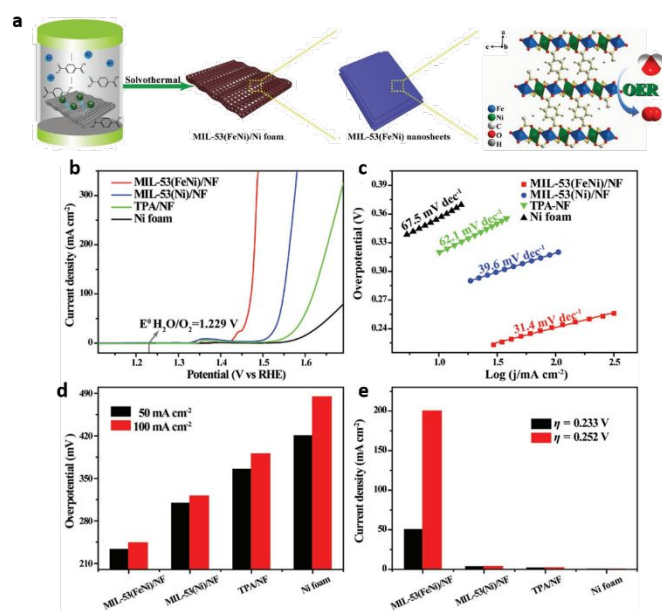


Fig. 2 a) Schematic illustration of the fabrication procedure of MIL-53 (NiFe)/NF. b) Polarization curves, c) corresponding Tafel slopes, d) overpotential required for $j = 50$ and 100 mA cm^{-2} , and e) current densities at $\eta = 233$ and 252 mV of MIL 53(FeNi)/NF, MIL-53(Ni)/NF, TPA/NF, and Ni foam.²⁴ Copyright © 2018 Wiley-VCH.

The as-prepared MIL-53(NiFe) shows excellent

OER performance (Fig. 2 b-e). Compared with the MIL-53(Ni), MIL-53(NiFe) gives a lower overpotential of 233 mV at the current density of 50 mA cm^{-2} in alkaline aqueous solution. As shown in Fig. 3, when integrated to the Fermi level, the density of 3d electrons in MIL-53 (NiFe) is 7.843 , which is higher than MIL-53 (Ni) (7.838). It has been proved that the increase in 3d electrons could effectively benefit the forming of the rate-limiting OOH^* intermediates during the OER process in the alkaline aqueous solution.⁹⁷ In addition, the more exposed carboxyl groups as well as the increased electrochemical active areas all contributed to the OER activity of MIL-53(NiFe).

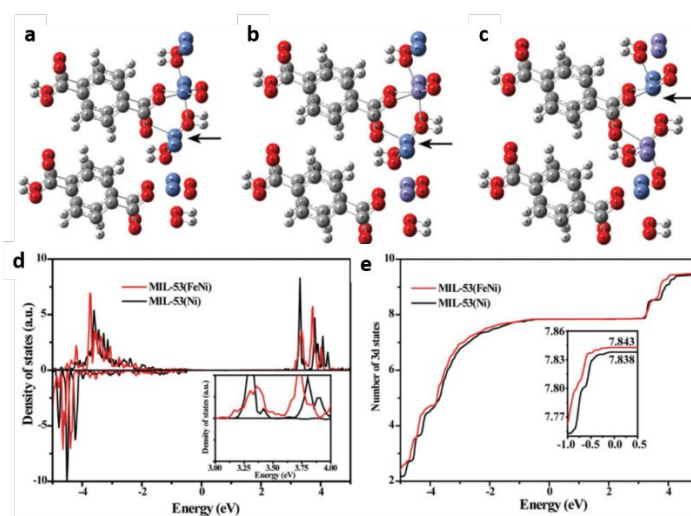
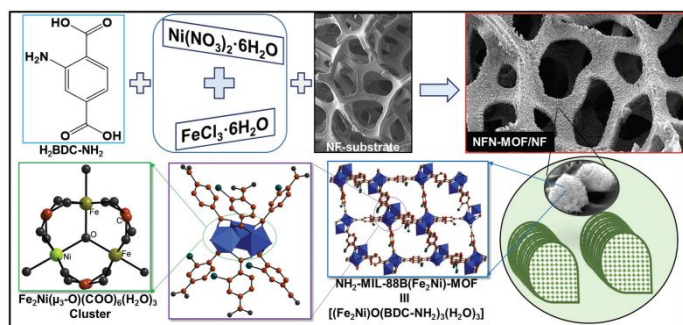


Fig. 3 Optimized geometries of a) MIL-53(Ni) and those of MIL-53(FeNi) with initial penta-coordinated b) Ni and c) Fe atoms. The penta- or hexacoordination of a metal atom is depicted and the metal atoms for foreign atoms' adsorption are indicated by arrows. d) Projected 3d density of states of the penta-coordinated Ni atoms in MIL-53(Ni) and MIL-53(FeNi) (inserts are the magnified

pattern), and e) the numbers of 3d states. Fermi level is set to zero. Copyright © 2018 Wiley-VCH.

The similar phenomenon is also observed in the water stable $\text{NH}_2\text{-MIL-88B}$ (Fe_2Ni) MOF (NFN-MOF), which is synthesized by the *in situ* growth on the surface of nickel foam (Scheme 2).²³



Scheme 2 Schematic illustration of synthetic process for *in situ* growth of micro-bundles of $\text{NH}_2\text{-MIL-88B}$ (Fe_2Ni)-MOF nanosheets on nickel foam (NF). Iron and nickel salts, $\text{H}_2\text{BDC-NH}_2$ ligand, minor amount of acetic acid as modulator, and NF are simply mixed together in DMF solution, and then heated to 125°C for 5 h, yielding uniformly grown MOF on backbone surfaces of NF.²³ Copyright © 2018 Wiley-VCH.

The macroporous and highly conducting properties of nickel foam (NF) are favorable for improving the overall charge transport of electrodes, mass transport of electrolytes, and mass transport of the produced bubbles (H_2 and O_2). $\text{NH}_2\text{-MIL-88}$ (B) is quite stable in water, which is essential for electrocatalytic activities. Compared with the corresponding bulk MOF phases, the nanosheet

morphology coupled with the nanopores in NFN-MOF can provide the vast and readily accessible metal cluster centers as the highly active sites for electrocatalytic reactions. In addition, there are three coordinated water molecules in each Fe_2Ni ($\mu_3\text{-O}$) cluster, which could offer catalytically active coordinatively unsaturated metal centers after the water molecules on the clusters are released from an ongoing process of OER. As a result, the NFN-MOFs achieved outstanding electrocatalytic activities at the high current density (500 mA cm^{-2}) and showed distinguished durability. This design concept could shed light on other electrocatalytic applications, such as, electrocatalytic reduction CO_2 and oxygen reduction.

In general, 2D materials tend to be more coordinatively unsaturated and are easier accessible to reactants, which ensure maximum utilization of electrocatalytic active sites and maximize the electrocatalytic reaction rates as well.⁶ To further elucidate the 2D materials, ultrathin MOF nanosheets (Ni-Fe-MOF NSs) with a thickness of a few nanometers have been synthesized in large-scale by a bottom-up solvothermal method.⁹⁸ As a proof of concept, the lamellar MOF with the formula of $[\text{Ni}_3(\text{OH})_2(1,4\text{-BDC})_2\text{-(H}_2\text{O)}_4] \cdot 2\text{H}_2\text{O}$ was selected and synthesized by solvothermal method. The ultra-stable Ni-Fe-MOF NSs can be directly obtained by replacing one third Ni atoms with Fe atoms and used as the efficient electrocatalysts

towards OER reaction, which display remarkable activities. The optimized Ni-Fe-MOF NSs (in Fig. 4) yield the highest OER performance with an overpotential of 221 mV at current density of 10 mA cm^{-2} . Notably, the rational utilization of the mixed solvents DMA/water with the ratio of 1:1 is crucial for the successful synthesis of gram-scale ultra-thin MOF nanosheets.

In addition, vertically inlaying ultrathin bimetallic NiFe MOF nanosheets grown on the surface of 3D ordered macroporous hydroxide are also demonstrated to be an effective method to explore the OER activity of electrocatalysts.⁹⁹ As depicted in Scheme 3, the assembled polystyrene (PS) spheres act as the soft template, and NiFe hydroxide is introduced into the void space of 3D ordered PS by the forced impregnation method, followed by the removal of PS templates to prepare macro-porous OM-NFH (macro-porous-NiFe hydroxide). After that, the NiFe MOF precursors are introduced and NiFe MOF/OM-NFH composite was synthesized by a simple solvothermal treatment. The typical morphology of the as-prepared NiFe MOF/OM-NFH is shown in Fig. 5, which is the 3D ordered skeleton structure composed of well-arranged spherical macropores and the interconnected walls. With this method, the obtained macro-porous OM-NFH provides the continuous channels for in-situ growth of NiFe MOF nanosheets on the external and internal surfaces. The open hierarchical structure

immobilized with the NiFe nanosheets provides abundant active sites, which is the substantial factor attributes to enhance the OER activity. This strategy could offer a new pathway for developing the nanostructures with controllable morphology and functionality for electrolysis.

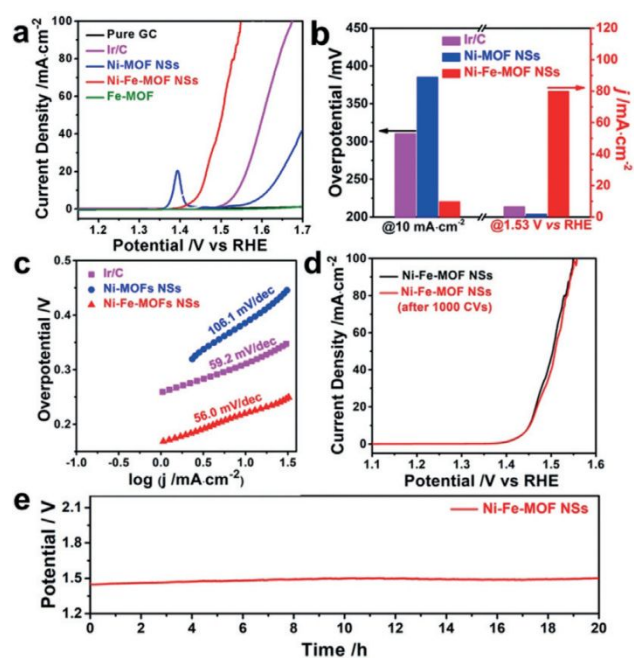
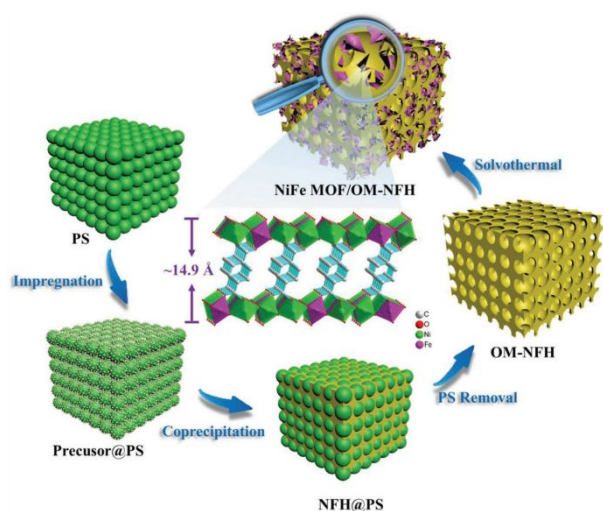


Fig. 4 a) Linear sweep voltammetry OER curves of pure GC, commercial Ir/C, Ni-MOF NSs, Fe-MOF, and Ni-Fe-MOF NSs. b) The corresponding overpotentials and current densities of different catalysts at 10 mA cm^{-2} and 1.53 V versus RHE. c) Tafel plots of different catalysts. d) Polarization curves of Ni-Fe-MOF NSs before and after 1000 CV cycles. e) Chronopotentiometry curves of the Ni-Fe-MOF NSs at 10 mA cm^{-2} .⁹⁸ Copyright © 2019 Wiley-VCH.



Scheme 3 Schematic representation for the preparation of NiFe MOF/OM-NFH.⁹⁹ Copyright © 2019 Wiley-VCH.

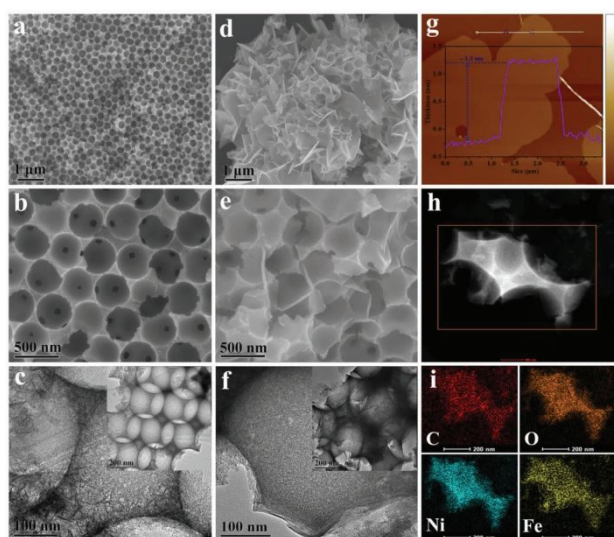


Fig. 5 a,b) SEM and c) TEM images of OM-NFH; d,e) SEM and f) TEM images of NiFe MOF/OM-NFH; g) AFM image of NiFe MOF nanosheets peeled from NiFe MOF/OM-NFH; and h) TEM image and i) corresponding EDX mapping images of NiFe MOF/OM-NFH for C, O, Ni, and Fe elements.⁹⁹ Copyright © 2019 Wiley-VCH.

Lattice strain in noble-metal-free MOFs also plays crucial roles in boosting electrocatalytic activities.⁵⁰ As illustrated by Qinghua Liu, *et al.*, as to synthesize the lattice-strained NiFe MOF, the pristine NiFe MOF nanosheets arrays supported on Ni foam was irradiated under the ultraviolet-light treatment for a series of times. After various times ultraviolet irradiation, the fringe lattice parameter of the NiFe MOF along the [100] direction was enlarged from 11.6 Å to 11.8 Å, 12.0 Å and 12.1 Å, which corresponded to the different lattice expansion ratios of 1.7%, 3.6% and 4.3%, respectively. And the structural characterizations of lattice-strained MOFs are shown in Fig. 6. The advanced operando SR-FTIR and XAS techniques revealed that the lattice strained MOF nanosheets showed excellent 4e⁻ pathway for electrocatalytic OER and ORR activity compared with the pristine MOFs, which contributed to the emergence of a key intermediate superoxide *OOH on the available Ni⁴⁺ active sites. This new strategy could serve as a tool for improving and optimizing the materials' electrocatalytic activities while preserving a high performance and stability for OER. Ji and co-workers also proposed a rational linker scission method to introduce lattice strain by partially replacing BDC with monocarboxylic organic linkers.¹⁰⁰ Owing to the infinite periodic repetition topology properties of MOFs, the substituted linker could introduce weaker interlayer interaction and result in interlayer expansion.

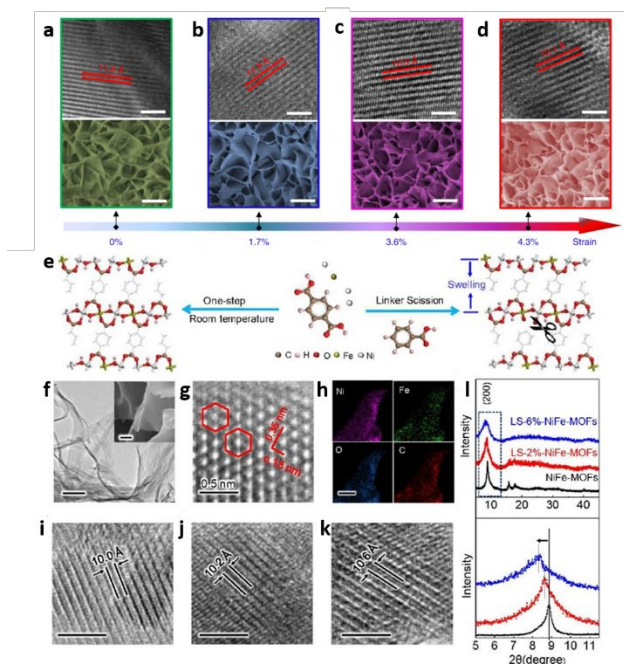


Fig. 6 Structural characterizations of lattice-strained MOFs. a–d, HRTEM (top) and SEM (bottom) images of the pristine (a), 1.7%- (b), 3.6%- (c) and 4.3%- (d) MOFs. Scale bars, 5 nm for HRTEM and 200 nm for SEM.⁵⁰ Copyright © 2019 Springer Nature. e) Schematic illustration of the synthesis of NiFe-MOFs and LS-NiFe-MOFs via a room temperature hydrothermal method. f) TEM and SEM images g) HRTEM images of the (200) planes of LS-NiFe-MOFs. h) Corresponding elemental mapping images of LS-NiFe-MOFs. Scale bars, 100 nm. (i–k) HRTEM images for NiFe-MOFs, LS-2%-NiFe-MOFs and LS-6%-NiFe-MOFs, respectively. l) Top panel: XRD patterns of NiFe-MOFs and LS-NiFe-MOFs crystal. Bottom panel: enlarged XRD patterns.¹⁰⁰ Copyright © 2020 American Chemical Society.

As observed from HRTEM and XRD image in Fig. 6 (i–l), the interlayer spacing of LS-2%-NiFe-MOFs

and LS-6%-NiFe-MOFs are enlarged to 10.2 Å and 10.6 Å compared with the pristine NiFe-MOFs (10.0 Å), respectively. And XRD pattern in Fig. 6l with significantly shifted downwards of diffraction after the introduction of 10% and 20% monocarboxylic acid could further confirm the existence of lattice strain. The optimal sample is LS-NiFe-MOFs with 6% lattice expansion, which exhibits a low overpotential of 230 mV at 10 mA cm⁻² in alkaline solution. Meanwhile, this study observed the formation of active species of HOO* intermediate on the high-valence Ni^{3+/4+} by using the cutting-edge operando X-ray absorption spectroscopy (XAS) and Fourier transform infrared (SR-FTIR) spectroscopy during water oxidation process. DFT calculations also confirm that the rate-determining step is the formation of HOO* and reveal that the introduced lattice strain can regulate the electronic structure of the Ni active sites in MOFs, further adjust the OER activities of NiFe-MOFs.

3.2.2 NiCo-based Pristine MOF Materials for OER

In addition to NiFe MOFs, other hetero-metal units have also been applied in the synthesis of MOFs materials for OER catalysis study and exhibit superior OER performance. For example, Tang's group reported NiCo bimetallic MOF nanosheets with high OER activity and further explored the relationship of structure-performance at the atomic

level.¹⁰¹ From then on, numerous of studies on the bimetallic MOFs used for electrocatalytic OER have emerged. For instance, Dong's group¹⁰² have first prepared the ultrathin Co_9Ni_1 nanosheets arrays on the CoNi foam by the universal one-pot building-up method, then through gradual oxidation-dissociation of NiCo foam by the polar solvent together with benzenedicarboxylic acid (BDC), MOF nanosheets are obtained by in-situ self-assembly of BDC molecules with the dissociated cations on the surface of the NiCo substrate. The electrode exhibits excellent electrocatalytic activity and long-term stability with the fast $4e^-$ pathway. The electron-coupling synergistic effects between the metals of Ni, Co and coordinatively unsaturated atomic active sites could have contributed to the excellent electrocatalytic performance.

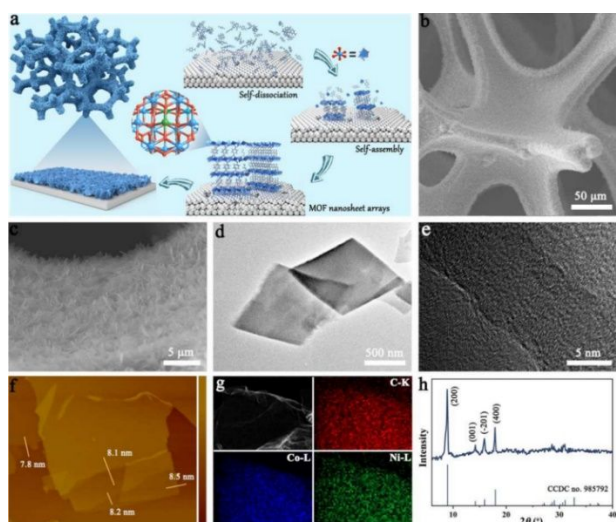
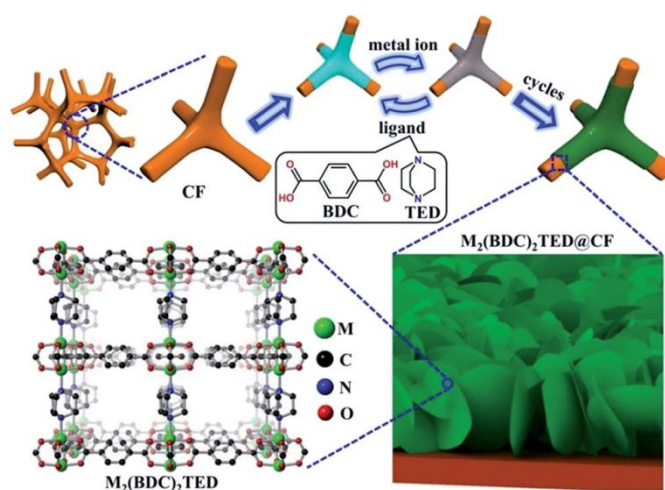


Fig. 7 Synthesis and characterization of CoNi-MOFNA. (a) Schematic illustration of SDA strategy for the synthesis of CoNi-MOFNA. The blue, green and red balls represent the Co^{2+} , Ni^{2+} and O atoms, respectively. The silver balls represent the Co_0 or Ni_0

atoms of Co_9Ni_1 metal foam substrate. (b, c) SEM images, (d) TEM image, (e) HRTEM image, (f) AFM image, (g) EDX elemental mapping images, and (h) XRD pattern of CoNi-MOFNA.¹⁰² Copyright © 2020 Elsevier B.V.



Scheme 4 The preparation process of the 3-D thin film of $\text{M}_2\text{-(BDC)}_2\text{TED}$ nanosheet arrays grown on Cu foam by the liquid-phase epitaxial method.¹⁰³ Copyright © 2019 The Royal Society of Chemistry.

Higher porosity and multiple organic components 3D MOFs with ultrathin nanosheets are some of the important factors for enhancing materials' OER electrocatalytic activities. In addition, in order to address drawbacks of the poor electroconductivity and instability of MOFs, in-situ growth MOFs on metal foam have been proved to be an effective pathway for high performance OER materials. This strategy could also play significant role in preventing catalyst aggregation and shedding,

exposing more active sites and lessening the resistance of charge transfer.^{104, 105} As shown in Scheme 4, the 3D thin film MOF $M_2(\text{BDC})_2\text{TED}$ ($M=\text{Co}$, Ni and Ni/Co ; $\text{BDC}=1,4\text{-benzenedicarboxylate}$; $\text{TED}=\text{triethylenediamine}$) nanosheets was synthesized on the surface of Cu foam by a layer-by-layer method with a mixed organic ligands (BDC/TED) and metal salts.¹⁰³ Notably, by adjusting the thickness and the Ni/Co ratio, the performance of the OER electrocatalyst could be optimized. For example, $\text{Co/Ni}(\text{BDC})_2\text{TED}$ after 40 liquid-phase epitaxial cycles with Co/Ni ratio of 1/1 shows the highest OER activity which exhibits a low overpotential of 260 mV at 10 mA cm^{-2} current density. The DFT calculation result has verified that the Ni nodes are easier to be triggered at the beginning of the OER step whilst the Co nodes are more dynamic in the electron transfer and desorption processes. Therefore, combining Ni and Co nodes is an effective way to reduce the energy barriers and boost the OER performance.

TEM, d) HRTEM of NiCo-BDC BMNS. Electrochemical properties of NiCo-BDC BMNSs array for OER. e) Polarization curves, f) the overpotential comparison at the current density of 10 and 100 mA cm^{-2} , g) the corresponding Tafel plots, h) Cdl calculations¹⁰⁶ Copyright © 2019 WILEY-VCH.

Layered double hydroxides (LDHs) are a promising class of catalysts in the water splitting due to their flexible chemical compositions.^{106, 107} One way to synthesize ultrathin bimetal-MOF nanosheets (BMNS) is to start with the as-prepared layered double hydroxides NSs arrays and through in-situ transformation process, the released metal ions could coordinate with the organic ligands to form the MOF nanosheets until the LDH NSs were consumed completely. Based on this assumption, Zhang's group has prepared ultra-thin MOF nanoribbons by using the metal hydroxide nanostructures as the metal source and sacrificial template.¹⁰⁸ Apparently, the synthetic strategy is an excellent option to obtain the specific morphology MOF materials. Liu's group transformed the NiCo layered double hydroxides to the NiCo MOFs nanosheets to further explore the OER performance. As shown in Fig. 8, the resultant product exhibits a hierarchical structure with specific ultrathin BMNSs. This unique nanoarray architecture resulted in the better activity and durability toward OER performance than that of other NiCo -based MOFs materials. Moreover, the

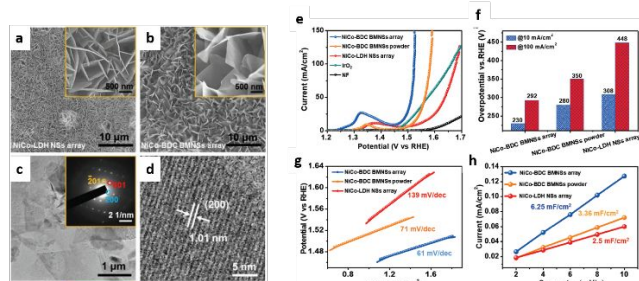


Fig. 8 Morphological and phase characterization of NiCo-BDC BMNSs array. SEM images of a) NiCo-LDH NSs and b) NiCo-BDC BMNSs arrays (the inset shows the high magnification SEM images). c)

excellent 3D architecture assembled from the nanosheets also contributed to the fast ion diffusion, efficient charge transfer with small charge transfer resistance and more exposed active sites. Such a general strategy to fabricate the MOF electrocatalysts on the conductive substrates should be widely used for enhancing the activities in energy conversion and storage.

Converting the bulk MOF crystals into 2D nanosheets is another effective way to address low electroconductivity, small mass permeability and chemical stability drawbacks, which have limited the application of MOFs as electrocatalysts in the harsh conditions.¹⁰⁹⁻¹¹¹ Designing the hierarchical nanostructures at the atomic level could have the potential to deal with the encounter problems of intrinsic restacking and low yield resulting from the synthesis process.

Li's group¹⁸ fabricated a novel isostructural transition-metal MOFs $[\text{NH}_2(\text{CH}_3)_2][\text{M}_3(\mu_3\text{-OH})(\text{H}_2\text{O})_3(\text{BHB})]$ ($\text{M}_3 = \text{Co}_3, \text{Co}_2\text{Ni}, \text{CoNi}_2, \text{Ni}_3$; named CTGU-10a1, b1, c1, d1, respectively) composed of the hexacarboxylic acid 4,4',4''-benzene-1,3,5-triyl-hexabenzoic acid (H_6BHB). These are highly desirable for their adjustable Co and Ni ratios and specific nanobelts morphology.

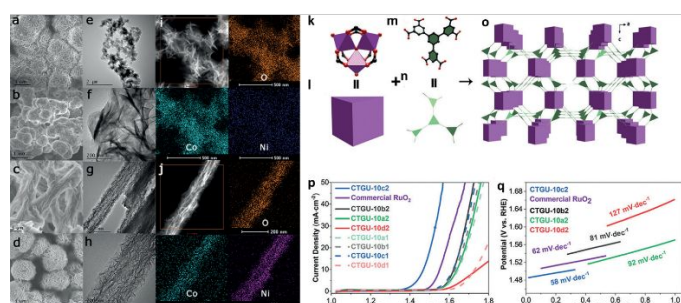


Fig. 9 SEM images of a) CTGU-10a2, b) CTGU-10b2, c) CTGU-10c2, and d) CTGU-10d2; e),f) High-resolution TEM images of CTGU-10b2; g), h) High-resolution TEM images of CTGU-10c2; i),j) HAADF-TEM images and TEM-EDS mapping images of i) CTGU-10b2 and j) CTGU-10c2. k) Metal trimers in CTGU-10a1 (C: black, O: red, Co: purple). l) Polyhedral representation of the trigonal prismatic geometry. m) Structure of the BHB ligand. n) Hexatopic BHB ligand. o) Framework of the nia topology. p) LSV curves and q) Tafel plots of RuO₂ and the CTGU electrocatalysts in the OER in 0.1M KOH.¹⁸ Copyright © 2019 Wiley-VCH.

The hierarchical structure, as shown in Fig. 9, adopts a $\text{M}_3(\mu_3\text{-OH})$ cluster as the SBU and each cluster is composed of three M^{II} ions and a $\mu_3\text{-OH}$ and then coordinated by six carboxylate groups and three H_2O molecules, which attribute to different morphologies acquired according to the different Co/Ni ratio. Notably, the CTGU-10c2 with the Co/Ni molar ratio about 1:2 shows the superior OER performance with a lower overpotential of 240 mV at 10 mA cm^{-1} in the 0.1 M KOH electrolyte.

3.2.3 FeCo-based Pristine MOF Materials

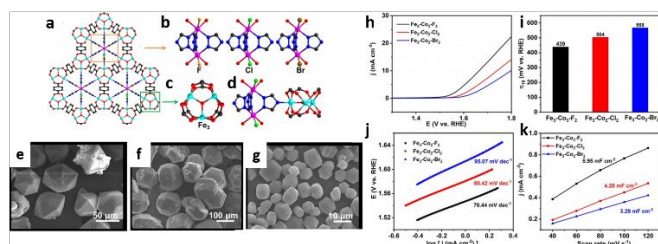


Fig. 10 3D framework of a) $\text{Fe}_3\text{-Co}_n\text{-X}_2$, b) the cobalt clusters with different halogen atoms, c) the Fe_3 trinuclear cluster, and d) the connection of the Fe_3 trinuclear cluster and the $\text{Co}_2\text{-X}_2$ dinuclear cluster. Color code: red, O; blue, N; black, C; light blue, Fe; pink, Co; yellow, F; green, Cl; brown, Br. SEM images of e) $\text{Fe}_3\text{-Co}_3\text{-F}_2$, f) $\text{Fe}_3\text{-Co}_3\text{-Cl}_2$, g) $\text{Fe}_3\text{-Co}_3\text{-Br}_2$. h) LSV curves of $\text{Fe}_3\text{-Co}_n\text{-X}_2$ for OER in 0.1M KOH. i) A comparison of the overpotential at current density of 10 mA cm^{-2} . j) Corresponding Tafel plots of $\text{Fe}_3\text{-Co}_n\text{-X}_2$ for OER in 0.1M KOH. k) Plots used for evaluating the Cdl of $\text{Fe}_3\text{-Co}_n\text{-X}_2$.¹¹² Copyright © 2019 Wiley-VCH.

Pore-space partitioning is an effective strategy to construct the stable crystalline porous materials (CPMs) with flexible chemical compositional including homo- or hetero-metallic clusters and diverse organic ligands.^{15, 113} Based on this premise, Lan's group reported a series of stable MOFs with the formulas of $[\text{Fe}_3(\mu_3\text{-O})(\text{bdc})_3][\text{Co}_{2.34}(\text{trz})_3\text{F}_2(\text{H}_2\text{O})_{3.32}(\text{OH}^-)_{0.68}]$ (named $\text{Fe}_3\text{-Co}_3\text{-F}_2$, $\text{trz}=1,2,4\text{-triazole}$) and $[\text{Fe}_3(\mu_3\text{-O})(\text{bdc})_3][\text{Co}_2(\text{trz})_3\text{X}_2(\text{H}_2\text{O})_4]$ (named $\text{Fe}_3\text{-Co}_3\text{-X}_2$, $\text{X}=\text{Cl}, \text{Br}$) to systematically investigate the impact of

the coordination environment of catalytic centers by coordinated with different electronegative coordination halogen atoms on the OER activity.¹¹² Under the theory of the electronegativity, the F shows the highest electron-withdrawing ability due to its largest electronegativity, accordingly, it results in smallest coordination with the Co electron density, which has a greater tendency to interact with OH^- . The OER performance results in Fig. 10 (h) show that the $\text{Fe}_3\text{-Co}_3\text{-F}_2$ has the smallest overpotential at a current density of 10 mA cm^{-2} .

In addition to halogen atoms, other functional groups can also effect the electrocatalytic performance because it could introduce the strain to the catalytic active centers and allow optimization of the interactions of the reaction intermediates with the surface of the electrocatalysts to improve the OER activity.¹¹⁴ BDC (terephthalic acid) and functionalized BDC are a family of common ligands used for MOFs synthesis. For example, with $\text{NH}_2\text{-BDC}$ as the organic ligand, Zaheer's group¹¹⁵ has obtained a series of bimetallic metal-organic frameworks (Co/Fe-MOFs) by adjusting the stoichiometric ratio of Fe and Co salts through a one-pot synthesis method. According to the hard and soft acid base (HSAB) theory, Fe^{III} ions prefer to bind with carboxylate (1 in Fig. 11 a)). Whereas Co^{II} ions can bind with either carboxylate or $-\text{NH}_2$ groups (3 in Fig. 11 a)). With this strategy, a series of different stoichiometric ratio of Fe/Co MOFs labeled as A to

F (A=1:0, B=1:1, C=1:3, D=1:9, E=1:19, F=0:1) was synthesized with Fe/Co MOFs A to D taking Fe-MIL-88B spindle-shaped morphology. The materials were studied as catalytic materials for OER. It is believed that the synergy between the two metals in B helped it exhibit smallest overpotential in comparison with the monometallic catalysts of A and F at 10 mA cm⁻² current density. Optimized the electronic structure of the intrinsic catalytic centers in MOF catalysts by engineering the metal nodes and the organic linkers can both help regulating the OER performance.¹¹⁶ For example, Su's group has reported a heterogeneity metal-organic framework (A_{2.7}B-MOF-FeCo_{1.6}) by assembling of metals, terephthalic (A) and 2-aminoterephthalic ligands (B). The different components in the A_{2.7}B-MOF-FeCo_{1.6} have shown great influence on the microstructure of the material.¹¹⁷ So tailoring the metal-containing centers and organic linkers to precisely control the topology, pore environment, and electron property of MOFs at the molecular and atomic level is effective ways to adjust the electroconductivity, pore size and active centers of catalysts.^{29, 118} As reported, the different mixtures of metal (Fe³⁺, Co²⁺) and ligands (A, B) can result in different morphologies, A-MOF-Fe, A-MOF-FeCo_{1.6}, B-MOF-FeCo_{1.6} and A_{2.7}B-MOF-FeCo_{1.6} exhibit the rod-like structures, while the A-MOF-Co is sheet-like shape. As shown in Fig. 11 (e), the optimal heterogeneity bimetallic MOFs A_{2.7}B-MOF-FeCo_{1.6} has the best OER performance

with a lowest overpotential of 288 mV at 10 mA cm⁻² among these MOF materials, which is contributed to the improved intrinsic activity of the catalytic centers by tailoring the electronic structure.

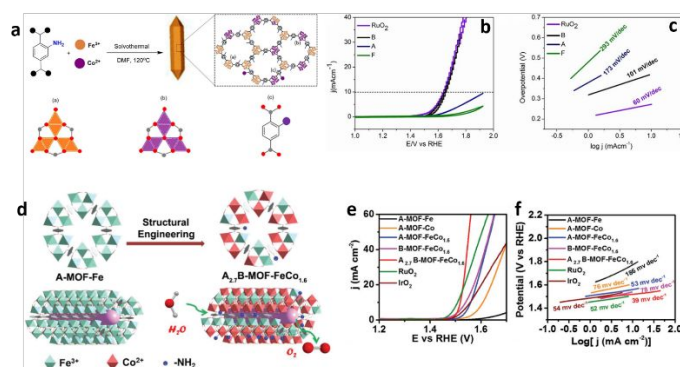


Fig. 11 a) Top: schematic illustration for the synthesis of mixed-metal (Fe/Co) MOFs with NH₂-BDC linker. Various possibilities for the existence of SBUs are shown at the bottom. 1) Individual trinuclear Fe₃(μ₃-O) cluster. 2) Individual Co₃(μ₃-O) cluster. 3) Co coordination with the -NH₂ function of the linker. Color codes: Co (purple), Fe (orange), O (red), C (gray). b) OER polarization curve, c) Tafel plots chronopotentiometry plot for B in comparison with RuO₂ and monometallic A and F catalysts.¹¹⁵ Copyright © 2019 Wiley-VCH. d) The preparation of heterogeneity MOF for electrocatalytic oxygen evolution. e) LSV curves toward OER and f) Tafel plots of A-MOF-Fe, A-MOF-Co, A-MOF-FeCo_{1.6}, B-MOF-FeCo_{1.6}, A_{2.7}B-MOF-FeCo_{1.6}.¹¹⁶ Copyright © 2018 WILEY-VCH.

Apart from the above mentioned strategy of applying LDH as the sacrificial template to synthesize the MOFs with specific morphologies

MOFs, using 2D oxide sacrificial approach (2dOSA) has also been demonstrated as an effective way to facilely obtain the ultrathin MOF-74 and BTC MOF nanosheets. This strategy was reported by the Zhu's group.¹¹⁹ It is well known that BTC MOF nanosheets cannot be obtained by the common method of ultrasonication-assisted exfoliation of the bulk counterparts (top-down) or the solvothermal strategy (bottom-up) without using organic reagents.^{120, 121} So this surfactant-free method (Fig. 12 a)) of using the amorphous metal oxide nanosheets (M-ONS), such as the FeCo nanosheets (FeCo-ONS) as the sacrificial templates to construct the MOF-74 nanosheets with the confined 2,5-dihydroxyterephthalic acid (H_4dobdc) organic ligands is a positive way to synthesize the 2D MOF

ONS with H_4dobdc ligand to form M-MNS. b)–g) TEM images of Co-MNS, Ni-MNS, Cu-MNS, FeCo-MNS, NiFe-MNS, and CoCu-MNS. h) XRD patterns of the synthesized MOF-74 nanosheets. i) OER polarization curves of FeCo-ONS, FeCo-MNS-1.0, FeCo-MB, and Co-MNS in 0.1 M KOH. j) The C.N. for Co-ligand and Fe-ligand of FeCo-MNS-1.0 and FeCo-MB. k) OER curves of FeCo-MNS-1.0, FeCo-ONS, and RuO_2 loaded on Ni foam with the loading amount of 2.0 mg cm^{-2} in 0.1 M KOH.¹¹⁹ Copyright © 2019 Wiley-VCH.

nanosheets. As it can be observed in Fig. 12 (b-g) that after metal in metal-ONS reacted with the H_4dobdc , the flat 2D MOF nanosheets can be obtained by transformation from the amorphous curly morphology. Compared with the bulk MOF-74 (FeCo MOF-74), the surface area of 2D MOF nanosheets is drastically reduced, which indicates that the incorporation of structure defects and coordinatively unsaturated metal sites result in maximizing the metal centers exposure to boost the catalytic activity. As shown in Fig. 12 (i), FeCo-MNS-1.0 ($H_4dobdc/FeCo-ONS=1$) displays a lower overpotential (298 mV) than FeCo-MB (FeCo-MOF bulk) (320 mV) to achieve a current density of 10 mA cm^{-2} . Compared with the bare Co-MNS and Fe-MNS, the overpotential value of FeCo-MNS-1.0 is also lower to generate the current density of 10 mA cm^{-2} , which confirms again the synergistic effect of

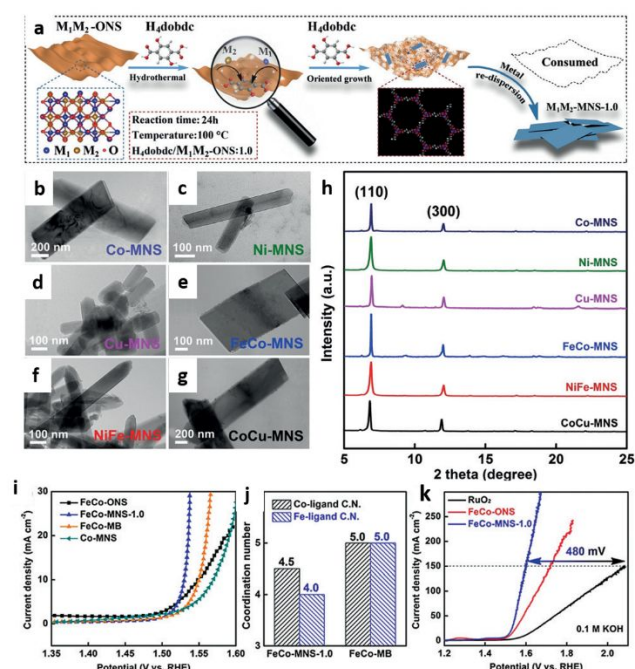


Fig. 12 Preparation and morphology characterization of M-MNS-1.0. a) Schematic illustration of the 2D oxide sacrifice approach (2dOSA) conversion of M-

heteroatom on the electrocatalytic performance of MOFs. This work represents another strategy towards the synthesis of the low-dimensional MOFs with the desired metal sites and modulating the electron structure at the atomic level.

A variety of different types of bimetallic MOF-based electrocatalysts have been reported. These

include the in-situ growth on the conductive substrates as well as pristine MOFs as electrocatalysts with different morphologies. As a summary, these materials and performance of the electrocatalytic properties are listed in Table 1.

Table 1. Summary of select bimetallic MOF-based electrocatalysts for OER activity. NF: nickel foam, CC: carbon cloth.

No.	Electrocatalyst	Substrate	Electrolyte	Overpotential (mV)	Tafel slope (mV dec ⁻¹)	Durability	Ref.
1.	CoNi-BDC	CC	1.0 M KOH	251 mV (10 mA cm ⁻²)	42	12 h	122
2.	Fe _{0.38} Ni _{0.62} -MOF	/	1.0 M KOH	190 mV (10 mA cm ⁻²)	57.4	20 h	123
3.	Fe ₂ Ni MOF	NF	1.0 M KOH	222 mV (10 mA cm ⁻²)	42.39	50 h	124
4.	MIL-53 (Co-Fe)	NF	1.0 M KOH	262 mV (100 mA cm ⁻²)	69	80 h	125
5.	Co ₃ Fe-MOF	/	1.0 M KOH	280 mV (10 mA cm ⁻²)	38	10 h	126
6.	2D CoFe-MOF	/	1.0 M KOH	277mV (10 mA cm ⁻²)	31	2000 s	127
7.	Fe ₁ Ni ₄ -HHTP NWs	CC	1.0 M KOH	213mV (10 mA cm ⁻²)	96	10 h	52
8.	NiFe-UNNs	/	1.0 M KOH	260 mV (10 mA cm ⁻²)	30	10000 s	128
9.	MIL-100(FeNi)	NF	1.0 M KOH	243 mV (100 mA cm ⁻²)	30.4	/	129
10.	Fe _{0.1} Ni-MOF	NF	1.0 M KOH	243 mV (50 mA cm ⁻²)	69.8	55000 s	130
11.	FeNi-MOF	NF	1.0 M KOH	235 mV (50 mA cm ⁻²)	79.5	100 h	28
12.	FeNi-MOF	/	1.0 M KOH	270 mV (50 mA cm ⁻²)	49	12 h	131
13.	FeNi-MOF	NF	1.0 M KOH	150 mV (100 mA cm ⁻²)	38.7	100 h	132
14.	CoFe MOF	/	1.0 M KOH	265 mV (10 mA cm ⁻²)	44	40 h	133
15.	NiFe-MOF/FeCH	NF	1.0 M KOH	200 mV (10 mA cm ⁻²)	51.3	50 h	134
16.	CoNi@HPA-MOF	/	1.0 M KOH	320 mV (10 mA cm ⁻²)	58	/	135
17.	FeNi(BDC)	NF	1.0 M KOH	277 mV (60 mA cm ⁻²)	37.4	30 h	136
18.	FeCo-PBA	NF	1.0 M KOH	256 mV (10 mA cm ⁻²)	54	36 h	137
19.	Fe ₁ Ni ₂ -BDC	/	1.0 M KOH	256 mV (10 mA cm ⁻²)	35	2 h	138
20.	FeCo-2D MOF	/	1.0 M KOH	274 mV (10 mA cm ⁻²)	46.7	/	139
21.	(Co-Ni) MOF/3DG	NF	1.0 M KOH	291 mV (20 mA cm ⁻²)	66.4	18000 s	140

3.3 TMB MOF-derived Materials

A large proportion of MOFs applied as the electrocatalysts suffer from the chemical stability

and poor electroconductivity issues. Owing to the existence of metal ions and different functional organic ligands in its framework, MOFs, especially bimetallic MOFs with controllable compositions in SBUs can be naturally employed as precursors

through self-templating to obtain the MOF derived materials, such as carbon composites (carbon encapsulated atomically dispersed metal, metal nanoparticles, alloy), metal compounds (phosphides and sulfides, and metal hydroxides/oxyhydroxides). These heteroatom doped transition metal-based materials derived from MOF materials could be used as efficient electrocatalysts such as for OER.⁴⁵ In order to serve as efficient OER catalysts, the materials need to provide effective channels for electron and mass transfer. In general, MOF-derived skeleton with plenty of micropores and mesopores could provide the transfer pathway. The transition metal MOFs composite of Ni, Co and Fe that have partially filled d orbitals, which coordinate with variety of organic ligands with various coordination geometries. These properties could provide possibility to obtain MOF-derived catalysts with different characteristic properties that could benefit their electrocatalytic properties.

3.3.1 TMB MOF-derived TMB Particle decorated Carbon Materials

Common synthesis methods for obtaining carbon materials usually include the exfoliation of graphite and graphite-like materials or pyrolysis of carbon containing materials. The MOF-derived carbon materials are typically obtained by pyrolyzing the MOF precursors with well-defined morphology, unique surface chemistry, various chemical

compositions and porosity.^{141, 142} Carbon-based materials derived from MOFs have some merits. By selecting MOFs with different morphologies, surface area and pore sizes, the number of active sites of the materials could be increased. The rates of transfer of substances could also be enhanced. In addition, with MOFs as precursors, the distribution of metal centers at atomic level could be well distributed in the obtained materials. However, the non-noble metals and alloys theoretically need to be stabilized by the hosts (usually is carbon materials) or saturated with high electronegativity elements because they are not stable in the harsh acidic and alkaline conditions.⁵⁷ The encapsulating transition metal-based particles with carbon shells are much more stable in harsh conditions since the carbon shell can protect the transition metal-based particles from directly contact with outside environments. And the high electroconductivity of the carbon skeleton could also help the OER kinetics as well. In addition, with flexible and diverse organic linkers in MOFs, it makes the incorporation of heteroatoms in the formed carbon materials easily. These doped carbon materials could have tunable polarity to further enhance materials electrocatalytic properties. For example, doping and co-doping the MOF-derived metal particles decorated carbon electrocatalytic materials with different heteroatoms, such as N, S, P *et al.*, have been shown to improve the performance of OER.^{27, 54, 143} The difference in electronegativity

between the carbon atoms and the heteroatoms induces the charges transfer from neighbor carbon atoms and therefore accelerating chemisorption of reactants as well as changing the local density of states and electronic structure.¹⁴⁴ The as-prepared MOF derived $M-N_x-C$ species, through the synergetic effect between the metal or bimetallic alloy particles and N-doped graphene shell are in favor the electron transfer from the metallic core to the N-doped graphene on the surface of the alloy particles, especially, when the graphene is single and few-layers.^{27, 145} The above theory was supported by many reported works. For example, Li's group reported that the thermal synthesis of FeNi@N-doped graphene dispersed on N-doped carbon matrix can act as the excellent electrocatalysts to boost the OER performance.¹⁴⁶ In this composite, FeNi alloy nanoparticles were encapsulated by few layers N-doped graphene and uniformly anchored on the conducting carbon matrix. The synergetic effect of the FeNi alloy and fast electron transfer from the FeNi nanoparticles to the N-doped graphene shells resulted in the outstanding OER activity, coupling with the protection of the carbon shells for alloy nanoparticles, the composite showed superior structural stability. The metal- N_x -based materials is conductive and metal- N_x also acts as the active sites affording an excellent electrocatalytic performance.^{147, 148} As depicted in Fig. 13, the carbon fiber derived from pyrolyzing the supporting

material polyacrylonitrile (PAN) fibers shows good electrical conductivity after the high-temperature carbonization process.¹⁴⁹ The co-existence of pyridine-N and NiCo- N_x has been proved to be active sites, and the pyridine-N theoretically locates at the edge of graphene matrix, which inclines to combine with the metal to form the metal-N group acting as the catalytic active site. In addition, the carbon nanofiber framework can also boost the electronic transmission, and the abundant pore structures facilitate the oxygen and the electrolyte contact and diffusion. The result is that, in Fig. 13b, the electrocatalyst of NiCo-0.8@N-CFs-800 presents the lower OER overpotential in 0.1M KOH medium. Prussian blue analogues (PBA) has an advantage of obtaining $M-N_x-C$ moieties by directly pyrolyzing the precursor in the inert atmosphere.¹⁵⁰ However, due to PBA contains fewer carbon and nitrogen elements and results in the calcined products also exhibit low C and N content. So, as we discussed above, the additional C, N-rich carbon nanofibrous materials PAN can be introduced as carbon and nitrogen source during the treatment. And it is the most acceptable method to combine MOFs and PAN to synthesize high electrocatalytic performance catalysts for its merits of commercial viability, high carbon yields, abundant nitrogen sources, and excellent electroconductivity.^{151, 152} As shown in Fig. 13c, the Co-Fe PBA@PAN precursor exhibits a one-dimensional fibrous morphology, and

after the carbonization process under a high-purity Ar atmosphere, the obtained FeCo-NCNFs-Ts ($T=700, 800, 900\text{ }^{\circ}\text{C}$) still kept the web-like fibrous structure encapsulating cubic protuberances. The one-dimensional carbon fibers can provide sufficient contact areas between the electrolyte and reactant, expose large amounts of active sites, and offer an electron transfer pathway to boost the OER process as well. This composite shows fascinating electrocatalytic performance and results from the encapsulated $M-N_x$ moieties in the graphitic carbon

layers, which act as active sites. Most importantly, the FeCo alloy can accelerate and catalyze the graphitization of carbon to obtain the materials with high electroconductivity and charge transfer ability.¹⁵³ In addition, porosity can provide an appropriate surface area to promote the diffusion of O_2 and electrolytes. The results are comparable with reported catalysts. The FeCo-NCNFs-800 shows excellent OER performance and stability in the alkaline solution.

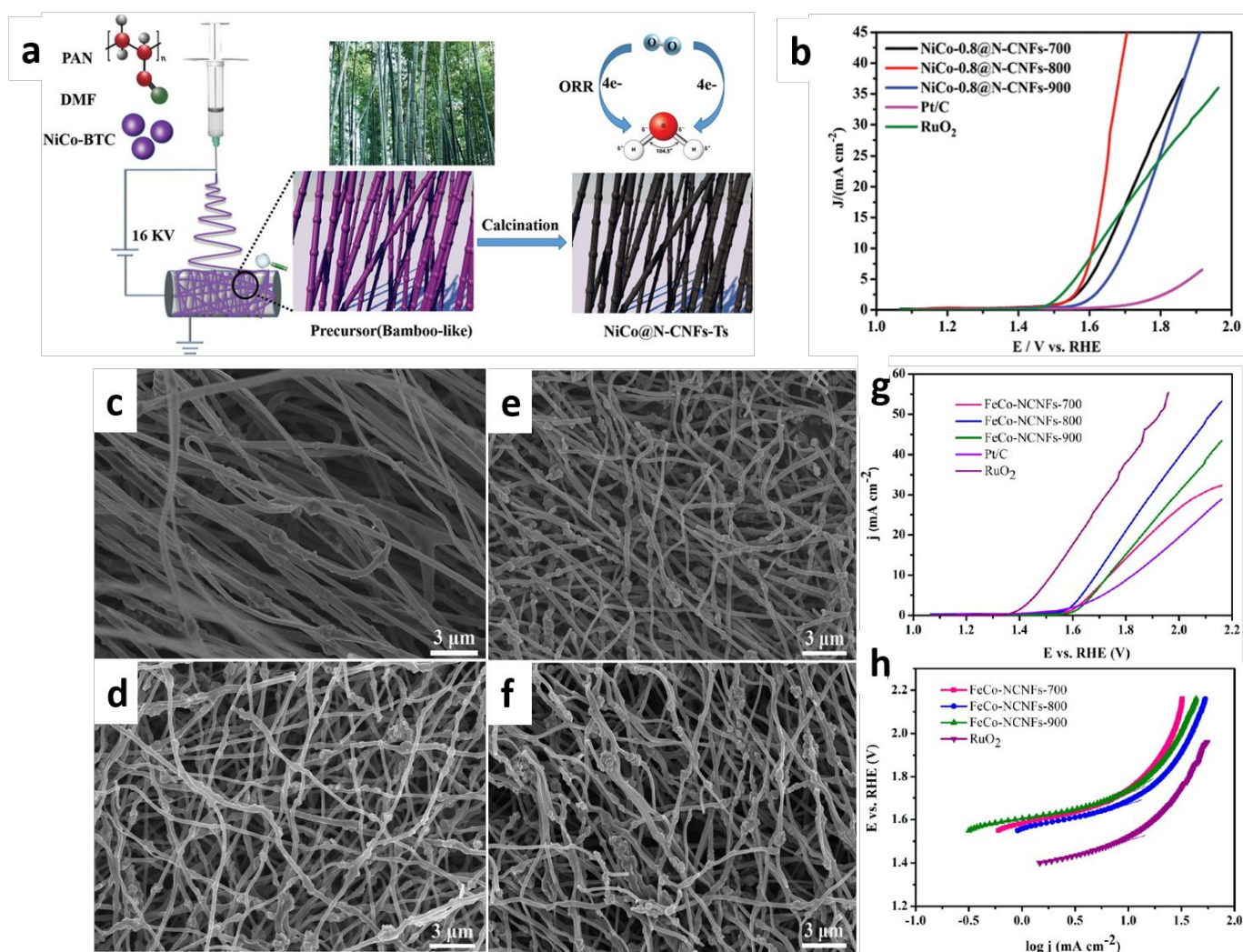


Fig. 13 a) Schematic preparation process for the NiCo@N-CNFs-Ts nanocomposite. b) LSV curves of NiCo-0.8@N-CNFs-Ts, Pt/C and RuO_2 in 0.1 M O_2 -saturated KOH solution at 1600 rpm.¹⁴⁹ Copyright 2020© Royal

Society of Chemistry. c) CoFe PBA@PAN nanofibers. d) FeCo-NCNFs-700. e) FeCo-NCNFs-800. f) FeCo-NCNFs-900. g) LSV curves of FeCo-NCNFs-Ts, Pt/C and RuO₂ in 0.1 M O₂-saturated KOH solution at 1600 rpm. h) Tafel curves of FeCo-NCNFs and RuO₂ electrocatalysts. Copyright © 2019 American Chemical Society.²⁷

Apart from the single non-metallic element doping, recently, the co-doping of N and other heteroatom species, such as: P, S and O, has attracted substantial research attention as well. The synergistic effect of co-doping is that adjacent heteroatoms increase the coordination of reactant molecules near the active site, or contribute electrons or withdraw from the charge density of the active site.¹⁵⁴ Previous works indicated that co-doped N and S had a tendency of promoting the formation of pyridine N preferentially, which was able to promote the HO*, HOO* adsorption, and it was due to the ability to accept electrons from adjacent carbon atoms.¹⁵⁵ This property plays an important role in improving OER performance. Xue and co-workers reported MOF-derived N-doped NiFe-sulfides/carbon hybrid architectures with different Ni and Fe molar ratios by carbonization and sulfurization process of bimetallic NiFe-MOF. The MOF-derived N, S co-doping material can not only enhance electroconductivity and accelerate the electron transformation but also the N doping derived from MOF ligand can tune the electronic properties and enhance the interaction between carbon matrix and active species. Thus, it is no big

surprise that the co-doped NiFe/N-S is reported as an efficient electrocatalysts for OER, with overpotential 232 mV at a current density of 10 mA cm⁻² in 1 M KOH aqueous solution. Another type of co-doping pair is N and P, compared with the single-doped, this co-doping of N and P led to an increase in active surface area and the density of active sites, which are keys for the improved OER activity. With this strategy, 3D hollow barrel-like FeNiP/C-900 co-doped with N and P were prepared through high temperature pyrolysis without the addition of external phosphorous source.¹⁵⁶ The BMM-10 MOF is synthesized by the suitable P-containing ligand and transition metal salt (Fig. 14a). The asymmetric unit of the structure is displayed in Fig. 14b, which consists of 2 Ni(II) cations, 4/3 TPO³⁻ ligands and one dabco linker (define dabco), so the structural formula can be defined as [Ni₂(TPO)_{4/3}(dabco)] • Guest. Through Fe³⁺ etching in the hot ethanol solution, the hollow barrel shape is obtained and it leads to the big difference in reaction kinetics between internal and external coordination bonds within MOFs. After being pyrolyzed at high temperature, the Fe and Ni are coordinated with P derived from ligand to form FeNiP, which exhibits excellent OER catalytic activity reaching a current

density of 10 mA cm^{-2} at an overpotential of 229 mV with a low Tafel slope of 74.5 mV dec^{-1} , it is due to the synergistic effect of Fe and Ni elements together with the N-doped carbon materials. In order to explore the co-doping synergistic effect, Xu and co-workers prepared a series of N and P co-doped FeCo-bimetallic MOF derived $\text{Fe}_x\text{Co}_y\text{-P/C}$ catalysts.¹⁵⁷ The bimetallic FeCo-MOF is synthesized by a simple sodium hydroxide-mediated method after a two-step carbonization and P-doping treatment of these precursors, the mesoporous structure of the $\text{Fe}_x\text{Co}_y\text{-P/C}$ is obtained. According to previous research results, N, P co-doping could decrease the total free energy for the carbon framework¹⁵⁸, which could be attributed to the lower reaction barriers in the process of OER, as a result, the $\text{Fe}_1\text{Co}_2\text{P/C}$ exhibited good OER performance. Therefore, N, S and N, P co-doped MOF-derived electrocatalysts are efficient methods to improve OER activities.

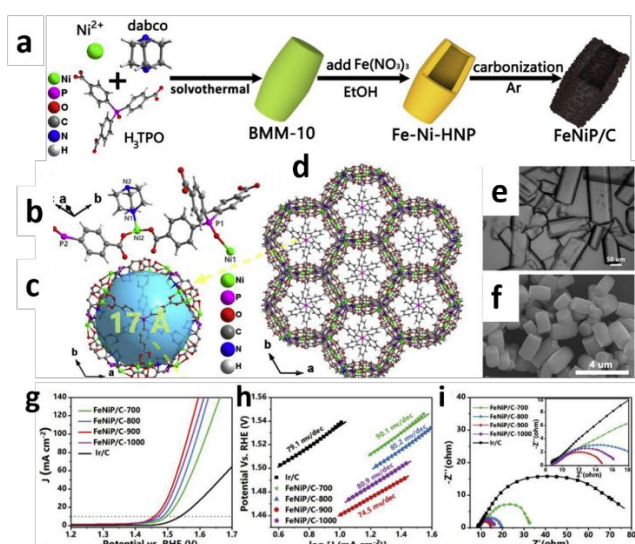


Fig. 14 a) Schematic illustration of the synthesis of in-situ MOF-derived bimetallic phosphide composite. b) The asymmetric unit of BMM-10. c)

A microsized cage consists of six $[\text{Ni}_2(\text{COO})_4\text{N}_2]$ SBU-1's and six $[\text{Ni}(\text{COO})_2(\text{O})\text{P}(\text{N})]$ SBU-2's. d) The dimensions of the 3D BMM-10 framework viewed in the c-axis. e) The photograph of S-BMM-10 and f) the SEM image of M-BMM-10. g) The OER polarization curves and h) the corresponding Tafel plots and h) EIS spectra at $\eta = 300 \text{ mV}$ of FeNiP/C-700, 800, 900, 1000 and Ir/C in 1.0 M KOH electrolyte.¹⁵⁶ Copyright © 2019 Elsevier B.V.

3.3.2 TMB MOF-derived Bimetallic Phosphides and Sulfides

The type of metal compounds (bimetal phosphides and sulfides) can be successfully prepared by the pyrolysis of bimetallic MOFs and introducing additional precursors, such as S or P-containing reagents, before or after the pyrolysis treatment. However, in the respect of solid-state chemistry, metal sulfides show less thermodynamically stability than that of metal oxides, but more than metal phosphides under oxidizing potentials, especially in the strong oxidative conditions of OER. Under this circumstance, metal sulfides and phosphides are more easily transformed into metal oxides or hydroxides. However, it is found that the derived metal oxides/hydroxide usually exhibit apparently better electrocatalytic performance than the corresponding simple metal oxides/hydroxides synthesized by the common method.^{159, 160} The

doping of heteroatoms in MOF-derived sulfides and phosphides, such as P and S, *etc.* play important role in optimizing the electronic structure because P and S show lower electronegativity comparing with oxygen in (oxy)hydroxide. According to the report by Subbaraman and co-workers¹⁶¹, the OER performance of 3d transition metal ions, such as Fe²⁺, Ni²⁺ and Co²⁺, in the oxide condition tend to be more active along with the weaken interaction of OH_{ad}-M²⁺(M=Fe, Co, Ni Mn). The formation of HOO* intermediates from the coordinated HO* can be motivated by the delocalized electrons among the adsorbed oxygen, metal centers and the doping S and P atoms.¹⁶² Therefore, this peculiarity accelerates the oxidation of the HOO* intermediate. It further affects the adsorption energies of OER intermediates and finally boosts OER performance.⁵⁷ Notably, the derived crystalline metal oxide/hydroxide layers on the surface of metal sulfides or phosphides play a vital role in preventing the metal sulfides or phosphides core from further oxidation, the obtained core-shell structure maintains a good stability and boosts the OER performance. This may provide a pathway for calculation or using *in situ* spectroscopic technique to explore the real catalytically active species of metal chalcogenides and phosphides. Transition metal phosphides (TMPs), especially Fe, Co, Ni-based alloying phosphides exhibit great potential as OER electrode materials. Several works demonstrated that TMPs own superior

electroconductivity for its higher metallic properties, which was also convinced by the higher intensity of the electrons near the Fermi level.¹⁶³⁻¹⁶⁵ It is proposed that the real active species of phosphides are surface oxy/hydroxides in situ evolved from metal phosphides during the OER process in the electrochemical oxide micro-environment.^{166, 167} Otherwise, when the electronegative P doping with the nearby active metal species, the localized negative charges of P³⁻ will prevent the coordination of the active sites and the hydroxide, which attributes to the strong 3d-2p repulsion force between d-band center and p-band center of transition metal and oxygen, respectively. It is further resulted in the formation of peroxide intermediate, which is conducive to the delivery of dioxygen molecule that caused by the increased 3p-2p repulsion between P and peroxide.^{13, 161} And the electron configurations and d-band centers of bimetallic MOFs can be tailored by the mix of different metals in the SBUs, which offers more opportunities to boost the electrocatalytic properties.¹⁶⁸ Peng and co-workers have fabricated Fe-doped Ni₂P nanoparticles that embedded in the carbon nanotubes and the MOF arrays were in situ grown on the nickel foam as the structural template.¹⁶⁹

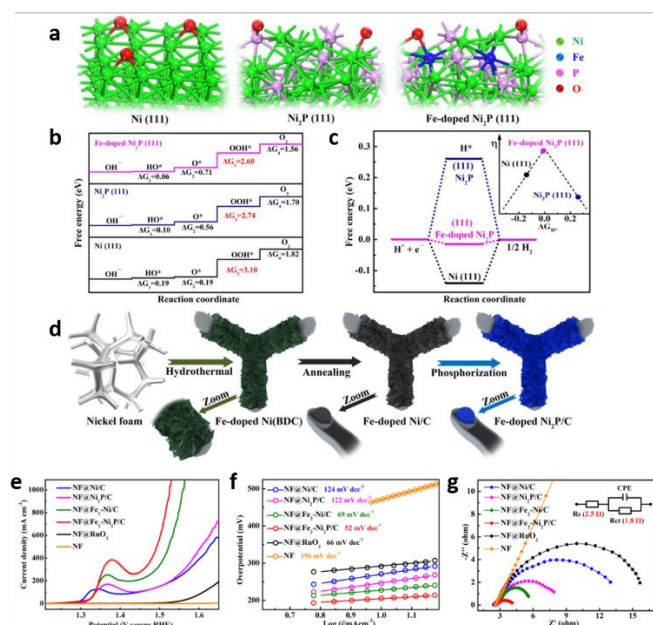


Fig. 15 Theoretical prediction and experimental design. (a) Structure models of Ni(111), Ni₂P(111), and Fe-doped Ni₂P(111) used for DFT calculation. (b) Free energy diagrams of OER intermediates on the above modeled surfaces. (c) Gibbs free energies of adsorbed hydrogen atom (ΔG_{H^*}) for HER. Inset: Volcano plot depicting HER overpotentials as a functional of ΔG_{H^*} . (d) Schematic illustration of catalyst preparation. Electrocatalytic oxygen evolution and hydrogen evolution performances. (e) OER polarization curves of various catalyst samples. (f) OER Tafel plots obtained by chronopotentiometry. (g) EIS spectra of various catalyst samples recorded at a constant potential of 1.53 V.¹⁶⁹ Copyright © 2019 American Chemical Society.

With the Fe doped Ni(BDC) MOF as precursor and after two-step of carbonization and phosphorization, the carbon nanotubes encapsulating metal phosphides nanoparticles were obtained (Fig. 15d). In alkaline electrolyte, OER is a four elementary process as we elucidated in the Reaction Mechanism section. Theoretically, the kinetics of every step of OER can be evaluated by calculating and comparing the free energy value $|\Delta G^*|$.^{170, 171} As depicted in Fig. 15b, the third elementary step is the rate-limiting step with the biggest energy barriers. The doping of Fe into Ni₂P changes the electron structures of Ni₂P, it is reflected by the decreasing of the overall adsorption of reaction intermediates in the optimal binding spot. It also can be explained by the slight downshift of d-band center for the Fe-doped Ni₂P with OOH* binding. So, it tunes the micromorphology of the catalyst, synergistically leading to enhance the OER activity.¹⁶⁹

However, the post-electrolysis characterization of the Fe₂@Fe₂-Ni₂P revealed that Fe/P-doped α -Ni(OH)₂ were formed during OER process, and after that it converted into α -NiOOH, which acted as the real OER active species with high electrochemical activity and stability.

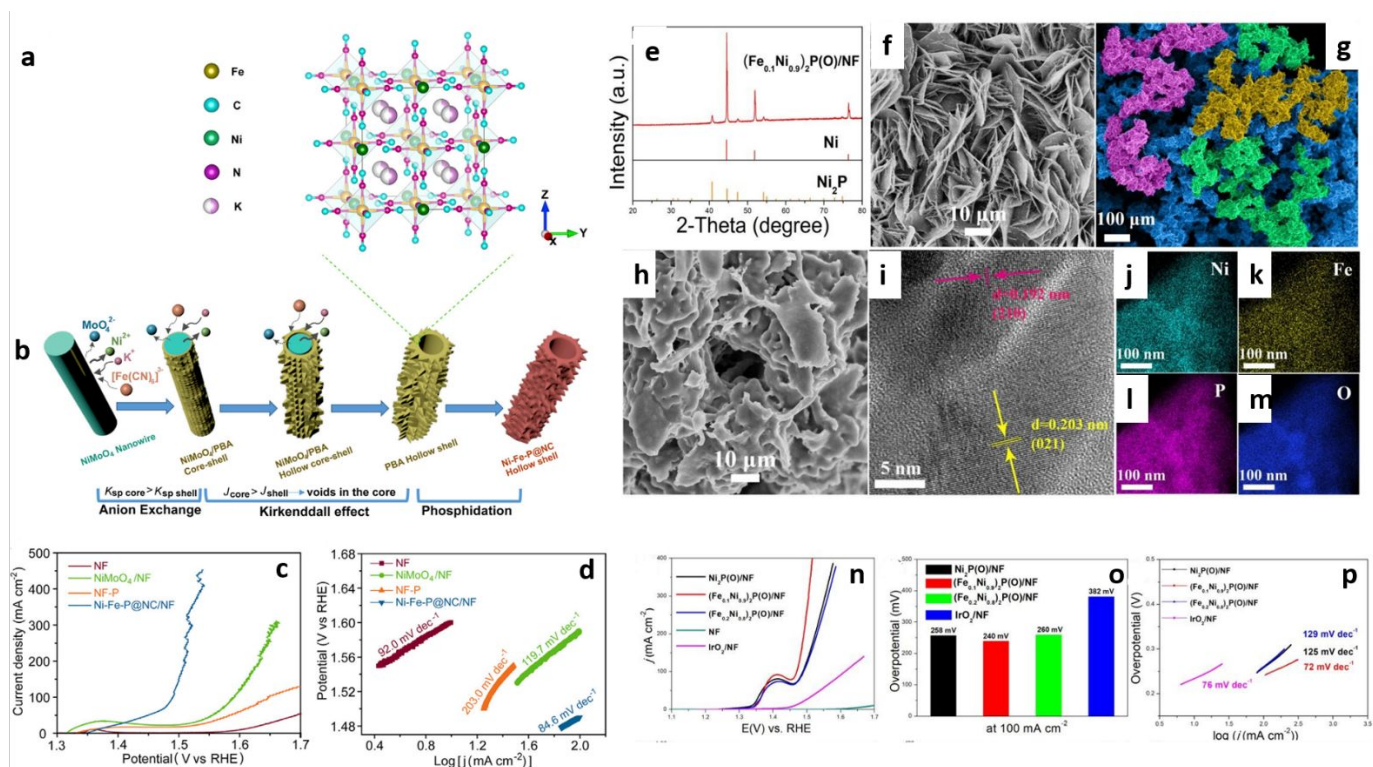


Fig. 16 a) Crystal structure of $\text{KNi}[\text{Fe}(\text{CN})_6]$ (PBA). b) Schematic illustration of the synthesis process of Ni-Fe-P@NC nanotubes (K_{sp} : solubility product; J : ion transfer rate). OER Performance in 1 M KOH c) Linear sweep voltammetry (LSV) and d) Tafel slope of Ni-Fe-P@NC/NF, NiMoO₄/NF, NF-P, and NF.¹⁷² Copyright © 2020 Elsevier. (e) XRD pattern for $(\text{Fe}_{0.1}\text{Ni}_{0.9})_2\text{P}(\text{O})/\text{NF}$. SEM images of (f) $\text{Fe}_{0.1}\text{-Ni}_{0.9}\text{-MOF}/\text{NF}$ and (g-h) $(\text{Fe}_{0.1}\text{Ni}_{0.9})_2\text{P}(\text{O})/\text{NF}$ (Note: image c is only toned). (i) High resolution TEM image of $(\text{Fe}_{0.1}\text{Ni}_{0.9})_2\text{P}(\text{O})/\text{NF}$. (j-m) EDX elemental mapping images for Ni, Fe, P and O in $(\text{Fe}_{0.1}\text{Ni}_{0.9})_2\text{P}(\text{O})/\text{NF}$. (a) OER polarization curves for $\text{Ni}_2\text{P}(\text{O})/\text{NF}$, $(\text{Fe}_{0.1}\text{Ni}_{0.9})_2\text{P}(\text{O})/\text{NF}$, $(\text{Fe}_{0.2}\text{Ni}_{0.8})_2\text{P}(\text{O})/\text{NF}$, NF and IrO_2/NF in 1.0 M KOH obtained at 1 mV s^{-1} . (b) Overpotentials at 100 mA cm^{-2} and (c) Tafel plots for $\text{Ni}_2\text{P}(\text{O})/\text{NF}$, $(\text{Fe}_{0.1}\text{Ni}_{0.9})_2\text{P}(\text{O})/\text{NF}$, $(\text{Fe}_{0.2}\text{Ni}_{0.8})_2\text{P}(\text{O})/\text{NF}$ and IrO_2/NF .¹⁷³ Copyright © 2020 Royal Society of Chemistry.

The hollow structures with high exposed surface area are desirable optional materials for constructing electrocatalysts. The 3D hierarchical structure consists of distributed Ni-Fe-P nanoparticles embedded in N-doped carbons (Ni-Fe-P@NC/NF) is prepared by an anion exchange method and a low-

temperature phosphating of nanotubular PBA, which is presented in Fig. 16b.¹⁷² Apparently, in this process, the NiMoO₄ is used as the template, the Kirkendall effect results in the anion exchange for the fabrication of hollow $\text{KNi}[\text{Fe}(\text{CN})_6]$ nanotubes. The obtained hollow heteroatom-doped carbon nanotubes (Ni-Fe-P@NC/NF) exhibited the most

favorable charge transfer ability among all the controlled electrodes. Notably, although vigorous gas evolution occurs during OER characterization, there are no bubbles accumulated on the surface of electrode for its macro-structure. The synergistic effect between bimetallic metal and P atom has endowed Ni-Fe-P@NC/NF superior electrocatalytic performance, and the active species in Ni-Fe-P@NC/NF are NiOOH or NiFe oxy/hydroxide, which guarantee the stability during OER process.¹⁷⁴ Mu's group¹⁷³ also reported iron and oxygen co-doped nickel phosphide ($\text{Fe}_{0.1}\text{Ni}_{0.9}$)₂P(O) fabricated by phosphating the MOF derivative sheet array on the nickel foam. Among the very limited reports on the synthesis of phosphides by using bimetallic MOF derivatives as precursors, Mu's work displays excellent OER performance at high current density. Wei's group used CoFe bimetal-MOF triangular plate arrays as precursor and obtained Fe-rich macroporous CoFeP triangular arrays. The obtained material was used for overall water splitting.¹⁷⁵ The large interconnected pores in the planes originated from the operation of selectively etching organic ligands from CoFe-MOF TPAs/Ni, and the following by phosphorization process to yield macroporous CoFeP TPAs/Ni. The catalysts exhibit excellent OER performance. For OER current densities of 10, 100 and 700 mA cm⁻², the overpotentials are only 198, 250 and 335 mV, respectively. The performance is even better than

noble-metal based electrocatalysts at large current density. So, MOF-based materials could be promising candidates as alternatives to replace noble-metal based materials for industrial water splitting. More works on bimetallic MOF-derived phosphide are listed in Table 2.

In addition to the TMP, transitional metal sulfide (TMS) have equally emerged as a prominent category material for OER, and they have many similarities. Recent fundamental studies substantiated that the effects of S on their nearby active sites toward OER resemble that of P, as mentioned above.¹⁷⁶ In terms of physical-chemical properties, most of metal sulfides share metal-metalloid bonds (M-S) with a strong covalent component, and couple with strong and highly covalent metalloid-metalloid bonds (S-S), which is similar with metal phosphides.¹⁷⁷ In addition, TMS have some unique properties such as: accessible electronic states, excellent electroconductivity, rich electrochemical redox sites, all lead to their superior OER performance.^{178, 179} To optimize the electrocatalytic activities of transition metal sulfides, Wang¹⁴³ and co-workers reported an economical strategy that applied CoNi-MOF as precursor/template to synthesize Ni-doped CoS₂ nanoparticles grown on the carbon fiber paper (CFP), which reduced the particle size and improved electroconductivity as well. Furthermore, profiting from the synergic effect of Ni doping and the

conductive CFP substrate, catalytic activities of Ni-doped CoS_2 -1/CFP exhibits a very low overpotential of 270 mV at 10 mA cm^{-2} , and great stability in 1M KOH electrolyte. To explore the secondary metal doping effect toward OER activity, the reduced graphene oxide (rGO) wrapped novel $\text{Co}_9\text{-Fe}_x\text{S}_8/\text{Co}$, Fe-N-C was synthesized through a semi-vulcanization and calcination pathway of FeCo-ZIF by Luo's group.¹⁸⁰ The specific hybrid structure could not only improve the generation of dual active sites resulting in highly bifunctional catalytic activity but also the incorporation of Fe could act as Lewis acid building up a higher alkaline environment around Co_9S_8 , which is a crucial factor to accelerate the OER process.¹⁸¹ In addition, the adoption of Fe can also increase the electroconductivity of the active species CoOOH that generate during OER reaction. As a result, combining all these advantages into the material bestows it surprising OER performance and stability which is comparable to that of the IrO_2 catalyst.

Compared with common TMDCs, MOFs-derived TMDCs are extensively studied and used as catalysts for OER electrocatalysis in recent years, which is due to the abundance of their raw materials, environmental-benign features and exceptional performances.

3.3.3 TMB MOF-derived metal hydroxides/oxyhydroxides materials

Currently, structure-engineered metal hydroxides and LDH of 3d transition metals electrocatalysts have attracted great attention in water oxidation applications.¹⁸² The materials with excellent catalytic performance was identified by Dai's group in 2013¹⁸³. Since then various combinations of divalent and trivalent type LDH materials, i.e., NiFe-LDH¹⁸⁴, FeCo-LDH¹⁸⁵, and NiCo-LDH¹⁸⁶ are reported. In these LDH materials, the transition metals in the layers undergo the redox reactions that further enhances the charge transport in the range of applied potential. However, it is still a big challenge to facilely obtain ultrathin metal oxyhydroxides nanosheets with excellent crystallinity and inerratic morphologies. Actually, MOFs can provide us an opportunity to obtain ultrathin metal-hydroxides for enhancing OER property. For example, Hong and co-workers applied electric-field assisted *in-situ* hydrolysis and transformed the MOF bulk into ultrathin metal oxyhydroxide nanosheets, these nanosheets were used as efficient OER electrocatalyts.¹⁸⁷ As exhibit in Fig. 17 a-f, FJI-H25FeCo were synthesized by the reaction of H_2BTTA ((2, 5-di(1H-1, 2, 4-triazol-1-yl) terephthalic acid)) with Fe and Co clusters. After two key processes, i.e., the first one is that metastable FeCo-MOF bulk transformed into hydrolysis products (FeCo-MOF-H) after alkali hydrolysis,

next one is applying electric-field driven reconfiguration FeCo-MOF-H bulk to ultrafast transform into FeCo-MOF-EH ultrathin metal oxyhydroxide nanosheets. The obtained nanosheets significantly enlarge the exposure of active sites, meanwhile, it also highly boosts the mass and charges transfer efficiency as well. It is noteworthy that the *in-situ* obtained FeCo-MOF-EH nanosheets on Ni foam possess excellent OER performance, which displays a low overpotential of 231 mV at the

current density of 10 mA cm^{-2} . It is a mild, fast, efficient and low cost way to synthesize metal hydroxides nanosheets without producing any impurities. As we aforementioned above that the final product and the active species for the majority of MOFs and other electrocatalysts are the corresponding metal hydroxides. Wu and co-workers proposed an efficient strategy to synthesize bimetallic FeCo-PBA nanosheet arrays in the presence of nickel foam.¹³⁷ The optimized PBA

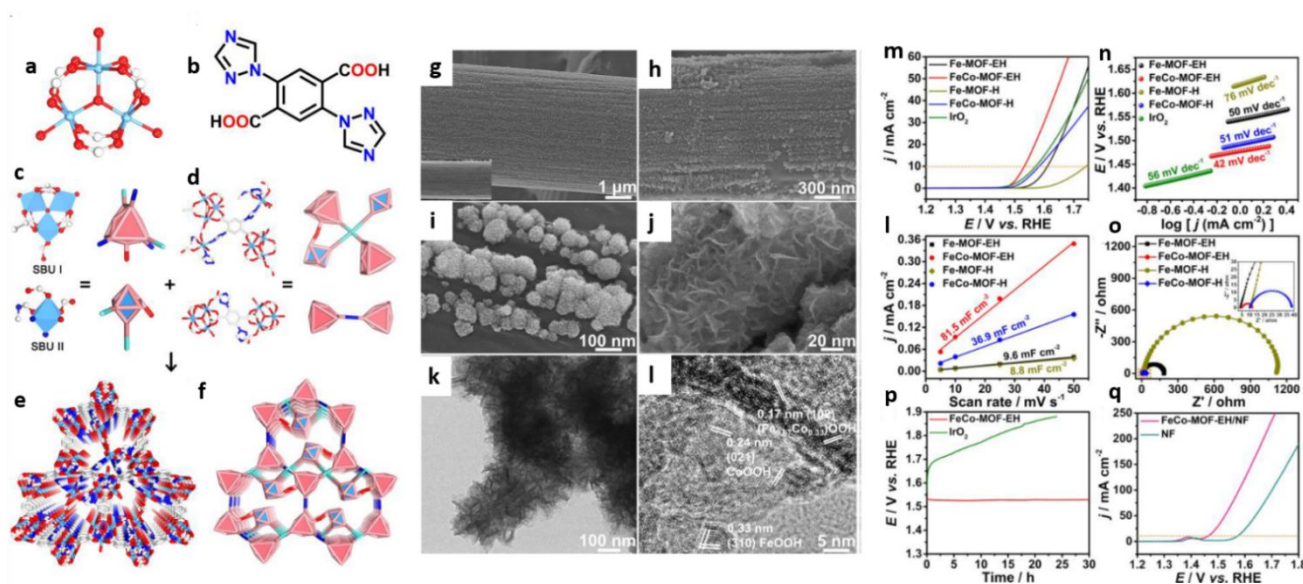


Fig. 17 (a) Structure of the selected metal cluster $[\text{Fe}_2\text{M}(\mu_3\text{-O})(\text{CH}_3\text{COO})_6]$. (b) Structure of the selected H_2BTTA ligand. (c) Trinuclear and mononuclear SBUs of Fe-MOF (FJI-H25Fe). (d) The linking modes of quadridentate and bidentate BTTA^{2-} ligand in Fe-MOF (FJI-H25Fe). (e) The framework of Fe-MOF (FJI-H25Fe). (f) The (3, 4, 6)-connected topology of Fe-MOF (FJIH25Fe). Morphology characterizations. (g, h, i, j) SEM, (k) TEM and (l) HRTEM images of FeCo-MOF-EH. Inset of g: SEM images of pure CFP. OER electrocatalytic performance. (m) LSV curves and (n) Corresponding Tafel plots of Fe-MOF-EH, FeCo-MOF-EH, Fe-MOF-H, FeCo-MOF-H and IrO_2 . (o) Plots used for evaluating the Cdl and (p) Nyquist plots of Fe-MOF-EH, FeCo-MOF-EH, Fe-MOF-H and FeCo-MOF-H. Inset: the enlargement of the orange box region shown in Fig. 4d. (q) Galvanostatic measurements of FeCo-MOF-EH and IrO_2 at a constant current density of 10 mA cm^{-2} . (r) LSV curves of FeCo-MOF-EH on nickel foam and bare nickel foam.¹⁸⁷ Copyright © 2020

Wiley-VCH Verlag GmbH & Co. KGaA, Weinheim.

nanosheet arrays only require 256 mV overpotential to reach 10 mA cm⁻² current density for OER in 1.0 M KOH solution. Combination of experimental result and theoretical calculation analysis unraveled that the favorable energy for OER can be largely due to the transformation to the high active Co/Fe-based (oxy)hydroxides during water electrolysis, in addition, the ultrathin nanosheet morphology, porous surface structure, coordinately unsaturated metal centers, and abundant active sites also play a vital role in accelerating OER activity. Bu's group also obtained NiFe-LDH by mixed Ni-MOF and Fe-

MOF in an optimal ratio (2:1) and then ultrasound in alkaline solution¹⁸⁸ During OER process, the ligand more likely to exchange with hydroxyl ions, so result in the formation of NiFe-LDH and without morphology change. Actually, the derived NiFe-LDH from NiFe-MOFs possesses better electroconductivity and OER performance than the single Ni or Fe hydroxides. MOFs-derived metal hydroxides maybe provide a pathway of maximize the advantages of MOFs and metal-hydroxides materials as OER catalyst. More profoundly, they also supply the basic understanding of the reaction mechanism for MOFs as catalyst for water oxidation.

Table 2 Summary of some typical TMB MOF-derived electrocatalysts for OER activity

No.	Electrocatalyst	Substrate	Electrolyte	Overpotential (mV)	Tafel slope (mV dec ⁻¹)	Durability	Ref.
1	NiFe alloy/N-CNT	N-CNT	0.1 M KOH	290 mV (10 mA cm ⁻²)	79	10 h	189
2	Co ₃ O ₄ /Co-Fe	/	1 M KOH	297 mV (10 mA cm ⁻²)	61	10 h	190
3	CoFeP	/	1 M KOH	235 mV (10 mA cm ⁻²)	34	12 h	191
4	(Fe _{0.1} Ni _{0.9})P(O)/NF	NF	1 M KOH	240 mV (100 mA cm ⁻²)	72	35 h	192
5	Co _{0.7} Fe _{0.3} P/C	/	1 M KOH	270 mV (10 mA cm ⁻²)	27	/	193
6	C-(Fe-Ni)P@PC/(Ni-Co)P@CC.	/	1 M KOH	251 mV (10 mA cm ⁻²)	56	24 h	194
7	CoFeP	NF	1 M KOH	198 mV (10 mA cm ⁻²)	42	100 h	175
8	NiFeP	/	1 M KOH	271 mV (10 mA cm ⁻²)	53	10 h	195
9	FeCoP	NF	1 M KOH	190 mV (10 mA cm ⁻²)	36	30 h	196
10	N-NiFe-S/C@CC	CC	1 M KOH	232 mV (10 mA cm ⁻²)	58	20 h	197

11	NiCo ₂ S ₄	CC	1 M KOH	370 mV (100 mA cm ⁻²)	95.76	20 h	178
12	NiCoS/Ti ₃ C ₂ T _x	Ti ₃ C ₂ T _x	1 M KOH	365 mV (10 mA cm ⁻²)	58.2	20000 s	198
13	NiFe-OH NS/NF	NF	1 M KOH	292 mV (500 mA cm ⁻²)	46.7	30 h	199
14	NiCoS-NS	/	1 M KOH	280 mV (10 mA cm ⁻²)	85	40000 s	200

4. Mechanism Elucidated by DFT and in-situ Experiments for OER

As for most electrocatalysts, a great attention of the OER research has been focused on structural regulation, catalytic performance optimization and morphology characterization. Despite having the detailed crystallographic information data of MOFs, it is hard to envisage the interplay of charges transport and mass transport (pore system), it is also difficult to define the reaction centers, actual active phases or, intermediates and electrochemical behaviors in OER process.¹² Therefore, to understand the reaction mechanism of the OER process is of great importance to direct the design of catalysts. Evidently, the first-principles kinetic model is an essential tool to describe overpotential with thermodynamics of elementary steps, and well explain experimental trends.²⁰¹⁻²⁰³ Such efforts built on the existing calculating models give a deeper insight into fine-tune catalysts performance in an optimal manner and provide a reasonable way to explore the mechanism of catalysts. Moreover, *in situ* experiments (operando) are gaining an

increasing interest as judicious tools in tracking the reconstruction of electrocatalysts, verifying real active sites, and labeling reaction intermediates during OER process.²⁰⁴ Therefore, the mutual support between theoretical calculations and *in-situ* techniques could provide a powerful guide for the interpretation of OER mechanism.

4.1 DFT calculations and mechanism

The following formula is the basis for calculating the adsorption Gibbs free energy of adsorbents (ΔG_{ads}), and it is a key descriptor to estimate whether the reaction could be trigger spontaneously.²⁰⁵

$$\Delta G_{ads} = \Delta E_{ads} + \Delta E_{ZPE} - T\Delta S \quad (4.1)$$

Where E_{ZPE} is zero energy calculated from the vibrational frequencies, ΔS is entropy change, T is the system temperature. The free energy differences of these various oxygenated species can be calculated by the following formula:

$$\Delta E_{OH^*} = E_{OH^*} + 1/2 E_{H_2} - E^* - E_{H_2O} \quad (4.2)$$

$$\Delta E_{O^*} = E_{O^*} + E_{H_2} - E^* - E_{H_2O} \quad (4.3)$$

$$\Delta E_{OOH^*} = E_{OOH^*} + 3/2 E_{H_2} - E^* - 2E_{H_2O} \quad (4.4)$$

$$\Delta E_{O_2} = E_{O_2} + 2 E_{H_2} - E^* - 2E_{H_2O} \quad (4.5)$$

All of the proposed mechanisms begin with an

essential elementary step of hydroxide coordinated to the active sites under alkaline environment²⁰⁶ and based on the four-electron step as we discussed in the part 2.1. The four elemental steps with reaction free energies of 1.23 eV represents the ideal situation that only takes thermodynamic hindrance into account, and the kinetic hindrance has been omitted. So the adsorption energies of intermediate species that involved in four-electron step should be higher in the real situation. At the standard conditions (pH=0, U=0), the Gibbs free energies difference of every step can be calculated as:

$$\Delta G_1 = \Delta G_{OH^*} - \Delta G^* \quad (4.6)$$

$$\Delta G_2 = \Delta G_{O^*} - \Delta G_{HO^*} \quad (4.7)$$

$$\Delta G_3 = \Delta G_{OOH^*} - \Delta G_{O^*} \quad (4.8)$$

$$\Delta G_4 = 4.92 - \Delta G_{OOH^*} \quad (4.9)$$

Here, the highest onset potential of the elementary step is denoted as a potential determining step, which is a decisive descriptor to predict the theoretical overpotential of a specific catalyst.²⁰⁷ However, it is different from the rate-determining step in terms of thermodynamic, while the potential determining step is more tend to describe the binding energy of reaction intermediates, which also can be deduced to estimate which step suffers the most sluggish process during the electrochemical process, and rate-determining step is directly related to experimental kinetics.^{203, 208} The catalytic activity is decided by the maximum difference of Gibbs chemical binding energy between subsequent

absorbed intermediates ($\Delta G_1, \Delta G_2, \Delta G_3, \Delta G_4$).

So the largest ΔG can be depicted as:

$$G_{OER} = \max \{ \Delta G_1, \Delta G_2, \Delta G_3, \Delta G_4 \} \quad (4.10)$$

As illustrated in Fig. 18 b, DFT calculation can elucidate the effect of metal coupling on the catalytic activities of the composite of FeNi-Tan.⁹⁶ For Ni-Tan, in the standard condition, the free energies of each step are -0.06 eV, 2.09 eV, 0.76 eV, and 2.13 eV, respectively. Evidently, the energy of step 4 is the largest among four steps, so it is the rate-determining step. However, when active sites change to Fe atom in (FeNi)-Tan, the Gibbs free energies of every step are 0.51, 1.55, 1.26, and 1.60 eV, respectively. Although the free energy of step 4 is reduced from 2.13 eV to 1.6 eV, it still is the rate-determining step. Therefore, Fe as active sites is favorable for OER activity. This is also supported by spin-polarized DFT calculations on the OER activities of several bimetallic MOFs electrocatalysts.²⁰⁵ In order to systematically compare the free energies of every step for a specific Fe_2M cluster, they first used the computational hydrogen electrode (CHE) model to explore the adsorption free energies of O^* , OH^* and OOH^* intermediate species and used Fe_3 cluster as the benchmark. As depicted in Fig. 18 e, the rate-determining step is the second step that means the intermediate conversion on the surface of Fe_3M cluster is from OH^* to O^* , which is determined by the weaker adsorption of O^* intermediate on Fe site.

Therefore, it could be a meaningful hypothesis to reduce overpotential by strengthening the adsorption energy of O^* . It could be helpful to examine the OER effect of the second metal incorporation (Co, Ni, and Zn) in bimetallic MOFs. As for the bare Fe_3 cluster, the Gibbs free energy of O^* is 3.16 eV, while after introducing the second metal, the ΔG_{O^*} of Fe_2Co , Fe_2Ni and Fe_2Zn are reduced to 2.15, 2.45, and 2.49 eV, respectively. Notably, as shown in Fig. 18 f, the incorporated Co, Ni and Zn have changed the electron structure of Fe_3 cluster, for which the d-band center of Fe_2Co , Fe_2Ni , and Fe_2Zn are closer to the Fermi level. According to the d-band center theory, it can result in stronger M-O adsorption energy between catalyst and adsorbates, so as to achieve the higher OER performance.²⁰⁹ Meanwhile, it has changed the rate-determining step from O^* to OOH^* on the Fe site with the OER overpotential of Fe_2Co (0.41 eV), Fe_2Ni (0.42 eV) and Fe_2Zn (0.59 eV). It also verified that the bimetallic clusters exhibit pronouncedly improved OER activities comparing with the corresponding mono-metallic MOFs. The similar fact is also reported from Luo's study, they applied DFT calculation to verify whether the catalytic reaction of FeNi MOF is thermodynamically feasible.¹³² As depicted in Fig. 18 g and h, compare with Fe-MOF and Ni-MOF, the largest barrier (formation energy of OOH^* is 1.55 eV) of bimetallic NiFe-MOF is the lowest, which means that the potential at approximately 1.55 V all OER

four-step elementary reactions can be triggered. This result is consistent with the Tafel slope result, where the Tafel slope of FeNi-MOF/NF is 39.8 mV dec^{-1} . The value is closer to 40 mV dec^{-1} , which is also verified that the third reaction step is the rate-determining step.²¹⁰

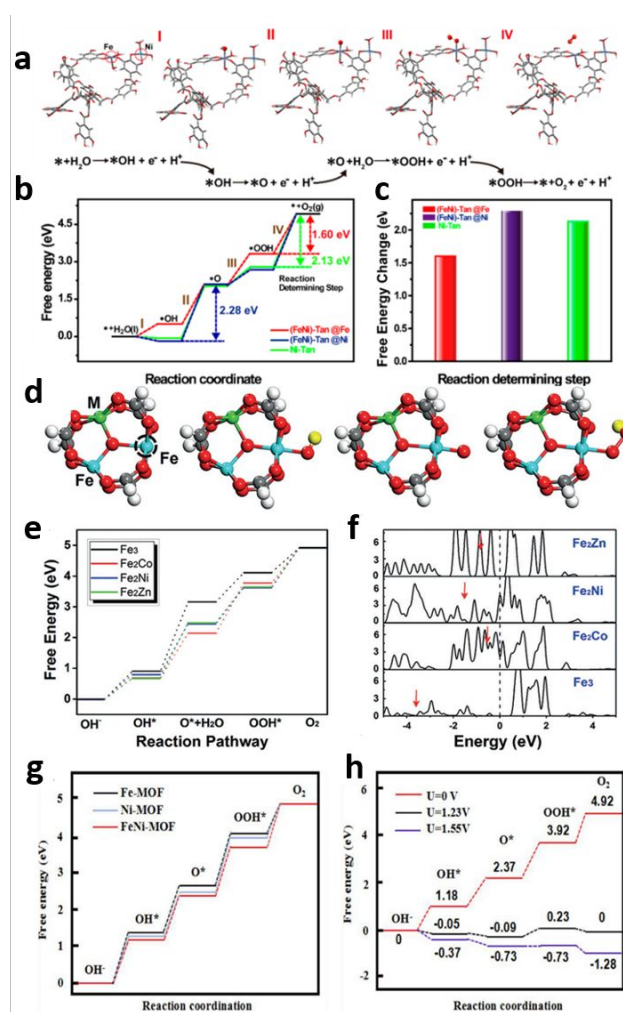


Fig. 18 DFT simulations for understanding the OER catalytic mechanism. (a) Reaction steps involved the adsorption atomic structures during the OER process for (FeNi)-Tan molecules on the Fe site. (b) Reaction free energy diagram of OER at zero electrode potential on Fe and/or Ni sites of the (FeNi)-Tan and Ni-Tan surfaces with the maximum

free energy change highlighted, and the free energies are relative to the starting reactants* and H₂O (l). (c) Corresponding free energy change of the reaction-determining step.⁹⁶ Copyright© 2019 American Chemical Society. d) Initial structure of the Fe₂M cluster, followed by the adsorption of OH*, O*, and OOH* intermediates on the Fe site. The active site is marked by a dashed circle. e) The free energy profile for the OER pathway and f) projected density of states of Fe₂M-cluster. Red arrows denoted the d-band center.²⁰⁵ Copyright © 2018 Wiley-VCH Verlag GmbH & Co. KGaA, Weinheim. (g, h) Free energy for OER on FeNi-MOF structure at different electrode potential U for OER, all water splitting reaction steps become exothermic at potentials above 1.55 V.¹³² Copyright © 2019 Elsevier B.V.

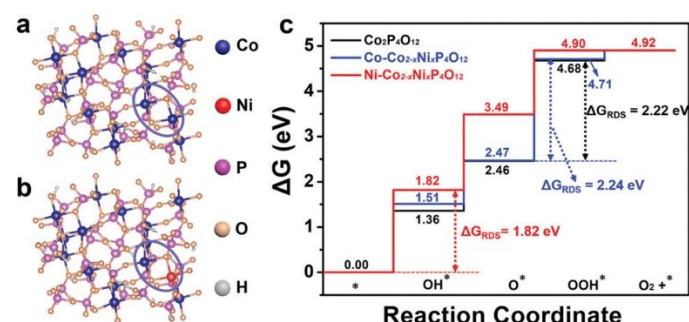


Fig. 19 DFT calculations and current density distribution simulations. a) The crystal structure of Co₂P₄O₁₂ and b) Co_{2-x}Ni_xP₄O₁₂ by substituting one Co site by Ni.²¹¹ Copyright © 2020 WILEY-VCH Verlag GmbH & Co. KGaA, Weinheim.

Apart from the pristine bimetallic MOFs, the synergistic effect between two metals of MOF-

derived electrocatalysts also can be observed by the DFT calculation. As shown in Fig. 19 a and b, the structure of Co-MOF derived Co₂P₄O₁₂ and CoNi-MOF derived Co_{2-x}Ni_xP₄O₁₂ has a little difference, where a portion of Co sites in the former one is substituted by Ni atoms. Apparently, as for Co₂P₄O₁₂, the rate-determining step with an energy barrier of 2.22 eV is to form OOH*. However, once Co acts as the active sites in Co_{2-x}Ni_xP₄O₁₂, the energy barrier (2.24 eV) is higher compare with Co₂P₄O₁₂. Meantime, for Ni site of Co_{2-x}Ni_xP₄O₁₂ (red line), the adsorptions of OH*, O*, and OOH* intermediates are remarkably weakened and the rate-determining step also has changed from the formation of OOH* to OH*. Due to the weaker O affinity to Ni, the barrier on Ni site is 1.82 eV, which is lower than Co site. Therefore, Ni plays a crucial role in improving OER activity by lowering adsorption energy of intermediate. From what we discussed above, ΔG₁ and ΔG₄ rarely act as the rate-determining step in majority OER systems, the difference between ΔG_{O*} and ΔG_{OOH*} is usually applied as a universal descriptor to predict the OER activity.²¹²

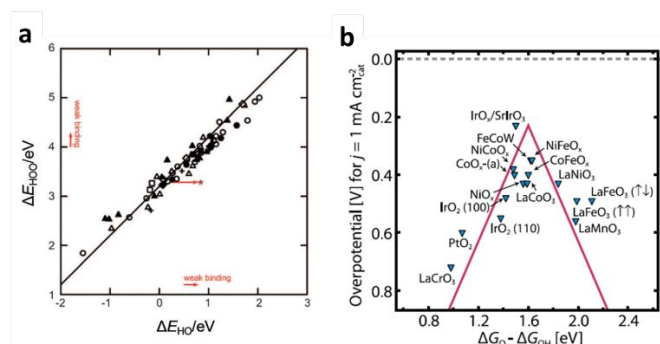


Fig. 20 a) Adsorption energy of HOO^* plotted against the adsorption energy of HO^* on perovskites, rutiles, anatase, Mn_xO_y , Co_3O_4 , and NiO oxides (perovskites (\circ), rutiles (Δ), Mn_xO_y (\square), anatase (\diamond), Co_3O_4 ($+$), NiO).²¹³ Copyright©2011 WILEY-VCH Verlag GmbH & Co. KGaA, Weinheim. b) Volcano plot for metal oxides. The volcano itself corresponds to $\Delta G_{\text{OOH}^*} = \Delta G_{\text{OH}^*} + 3.2 \text{ eV}$.²¹⁴ Copyright © 2017 American Association for the Advancement of Science

In aforementioned, in the ideal circumstance, no overpotential is needed for OER to occur ($\Delta G_1 = \Delta G_2 = \Delta G_3 = \Delta G_4 = 1.23 \text{ eV}$). While in the real condition, the theoretical overpotential, when it is independent of pH, the value can be given by formula (4.11)

$$\eta = \max \{ \Delta G_1, \Delta G_2, \Delta G_3, \Delta G_4 \} / e - 1.23 \text{ V} \quad (4.11)$$

Besides, the values of experiments and theoretical calculation have the large difference, as for the experimental result, the Tafel slope is the most reliable evidence to identify the rate-determining step.²¹⁵

In fact, the scaling relationship of $\Delta G_{\text{OOH}^*} = \Delta G_{\text{OH}^*} + 3.2 \pm 0.2 \text{ eV}$ (Fig. 20a) was found to apply

universally to many four-electron-step electrocatalyst such as metals or oxide surface.^{213, 216} Based on this scaling relationship, the value of ΔG_{OOH^*} and ΔG_{OH^*} can be obtained if one of them has been calculated out. In addition, because the real difference between ΔG_{OOH^*} and ΔG_{OH^*} must be larger than the ideal model ($2.46 \text{ eV}: 2 \times 1.23 \text{ eV}$), the minimum value of overpotential is 0.37 eV , which can be utilized as a rule to construct an activity volcano plot based on the binding strength between catalyst and O^* .²¹³ As we can see from Fig. 20b, the catalysts near the summit of the volcano plot show the smallest overpotential, and the values of ΔG_2 is equal to ΔG_3 ($\Delta G_2 = \Delta G_3 = 1.6 \text{ eV}$). The sample in the left part of the plot, such as PtO_2 , LaCrO_3 , *et al.* possess the stronger binding strength of O^* and it is difficult to form OOH^* . While the samples in the right part is prone opposite to the left part, which exhibit the weaker O^* binding strength compare with OOH^* ($\Delta G_2 > \Delta G_3$). Therefore, as per the Sabatier principle, the adsorption strength of an optimal catalyst for the key intermediate is neither too strong nor too weak.

4.2 In-situ experiments and mechanism

It has been widely acknowledged that the majority of electrocatalysts would undergo a necessary reconstruction process during the four-step reaction of OER. As we mentioned above, understanding and identifying the active sites and

structural information are of vital importance to illustrate the catalytic reaction mechanism. However, the calculation techniques and *ex situ* characterization are not sufficient enough to deduce the accurate results. The main reason is that the *ex situ* is incompetent to detect the progressive changes in reaction kinetics and the existence of instant reactants intermediates during every step of OER reaction. Contrariwise, the *in situ* or operando measurements including, as summary in Fig. 21, X-ray diffraction, X-ray photoelectron spectroscopy²¹⁷, transmission electron microscopy, Fourier-transform infrared spectroscopy and Mössbauer spectroscopy *et al*²⁰⁴ are very powerful tools to track the reconstruction of electrocatalysts by integrating electrochemical measurement systems with spectrometer devices to collect operando spectra for phase, morphology, oxidation states as well as electronic structures in the realistic reaction process, which could be feasible to provide us a preliminary understanding of the pre-catalyst and real active sites.²¹⁸⁻²²⁰

In a representative work conducted by Zhang *et al.*,²²¹ *in situ* X-ray absorption near edge structure (XANES) technique was utilized to identify the information about the electronic/oxidation states of the *in situ* generated active sites. It was performed on the Ni K-edge of NiFe-PBA, NiO and Ni(OH)₂, as depicted in Fig. 22a, it could be clearly seen that the structure of NF-PBA-A is the same with Ni(OH)₂,

yet is quite different with NiO, which indicate that it has an analogous structure of Ni(OH)₂. The O K-edge XAS of NF-PBA-A is showed in Fig. 22d, there is a distinct peak at 533.5 eV, which is corresponding to a characteristic feature of –OH species supporting the above result. While the EXAFS part of the spectrum is more likely to

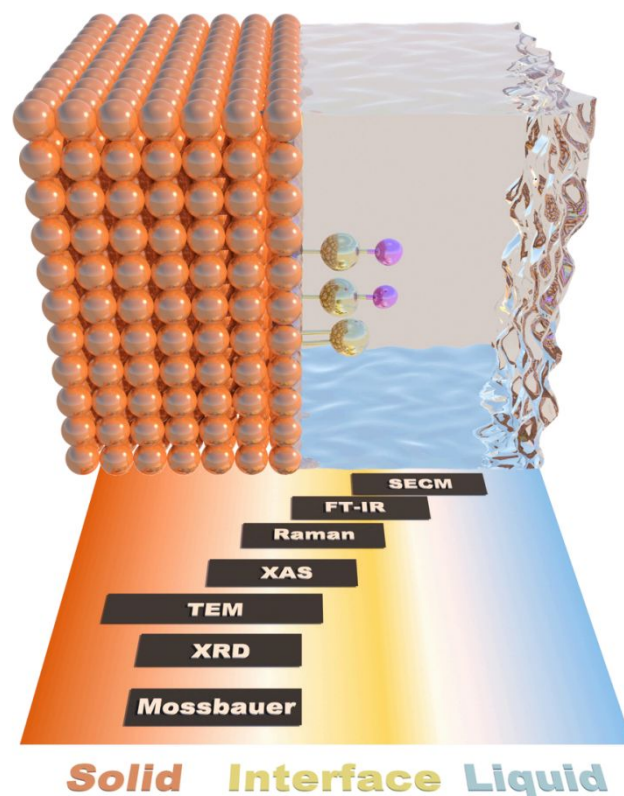


Fig. 21 *In situ* probing map of various representative *in situ* techniques.²⁰⁴ Copyright © 2020 American Chemical Society.

reveal the neighboring environment and coordination geometry of target atoms, as well as probe the nature about short-range order, bond length, and coordination numbers for the nearest neighbors.²⁰⁴ According to the result of FT-EXAFS in Fig. 22e, the coordination number and bond distance of Ni-O are 6.0 and 2.04 Å, yet as for Ni-Ni

are 4.6 and 3.08 Å, respectively. It can be concluded that NF-PBA was totally transformed into Ni(OH)₂ after OER reaction. In order to further understand the mechanism of OER, this work also carried out by operando Ni K-edge XAS to track the detailed changes of geometric and electronic structures with the changes of the applied potential during the oxygen evolution process. As shown in Fig. 22b and c, the adsorption energy edge gradually shifts upwards with the increase of applied potential, which means the oxidation state of Ni²⁺ ions is transforming into the higher valence states and exhibiting more reactivity. It is highly desirable to explore the local structure, i.e. the bond length of Ni during OER process with the technique of FT-EXAFS, as reported by previous studies that the bond distance of the first metal-oxygen shell is characteristic of the oxidation state of the metal ions.²²² In Fig. 22 f, the bond length of Ni-O in the initial NiFe-PBA is 2.04 Å, the valence state of Ni ions is +2 oxidation state, which is the same with the Ni ions in Ni(OH)₂. After a low potential of 1.46 V was applied, the bond distance of Ni-O is decreased to 1.99 Å, which means that the oxidation state of Ni ions both has +2 and +3 valence states. As a consequence, with further increase of the potential, the bond length shrank to 1.89 Å, which confirmed the existence of mix valence state of Ni³⁺ and Ni⁴⁺. The coordination number of the first Ni-O shell remains as a constant throughout the reaction process

that is consistent with the peak characteristic of octahedral units.

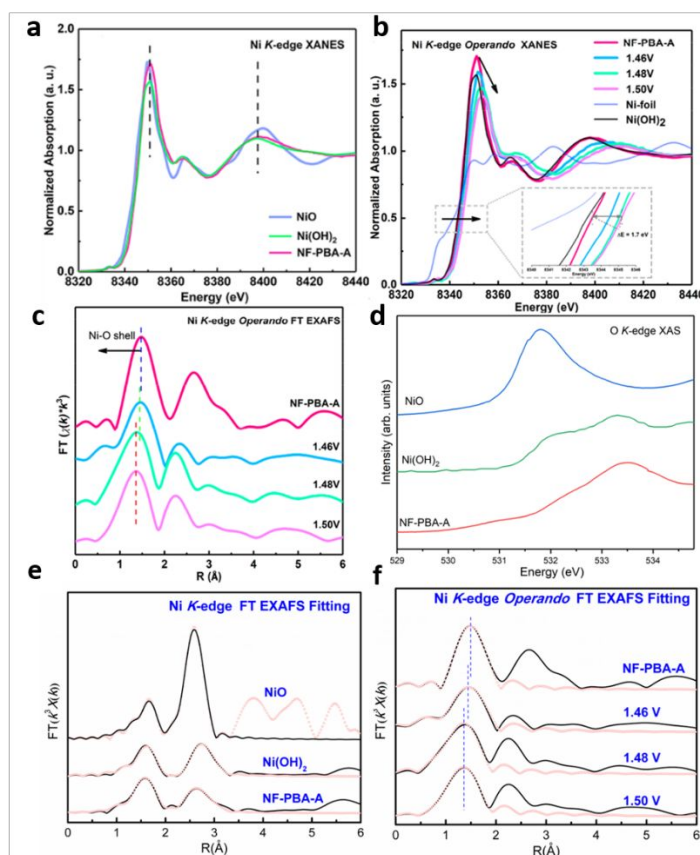


Fig. 22 a) Ni K-edge XANES spectra of NF-PBA-A compared to NiO and Ni(OH)₂. Operando Ni K-edge XAS spectra of NF-PBA-A under different potentials. b) XANES of NF-PBA-A as well as references. Inset shows the shift of Ni K-edge position. c) FT-EXAFS of NF-PBA-A. d) The O K-edge XAS of NF-PBA-A. e) FT-EXAFS fitting of Ni K-edge in NF-PBA-A as well as references. f) FT-EXAFS fitting of operando Ni K-edge in NF-PBA-A.²²¹ Copyright © 2018 American Chemical Society.

As illustrated above, both *in situ* FT-EXANS and FT-EXAFS techniques can be used to probe the underlying mechanism for MOF materials and it

shows that the high oxidation valence metal is formed during OER process and exhibits the excellent OER activity. Tang and co-worker also investigated the active sites and mechanism details with the assistance of X-ray absorption spectra technique.¹⁰¹ The existence of coordinatively unsaturated metal sites on NiCo-UMOFNs surface characterized by EXAFS analysis and XANES simulation are the dominating active centers for the electrocatalytic OER. After applied a given potential, the peaks of Ni as well as Co sites are more readily shifted to higher energy, indicating that the metal sites are prone to be oxidized to its oxy-hydroxide, which are responsible for the improved OER performance. In fact, the majority of non-oxide electrocatalysts are likely to convert pristine catalysts into the corresponding (oxy)hydroxides that plays a vital role as catalytically active sites in boosting the OER process. Besides, Huang *et al.* utilized *in situ* XAS to identify the OER active sites of coordinatively unsaturated metal nodes and revealed the structure evolution of CoNi-MOFNA during OER process.²²³ The result of EXAFS provides information that the coordination number of Co and Ni is approximately to be 5.8, less than 6, which means that the pseudo MO_6 octahedron with coordinatively unsaturated metal nodes has connected with the carboxylate from BDC. The plenty of coordinatively unsaturated metals (CoO_5 and NiO_5) on the surface of ultrathin MOFs

nanosheet can be identified as the intrinsic active sites.³⁰ During the OER process, the pre-edge peak intensity of Co and Ni in XANES spectroscopy has shifted toward higher energy along with an increase of CV cycles. Simultaneously, a new peak has emerged in the FT-EXAFS spectra of Ni K-edge, and the intensity of this peak increases relative to Co K-edge. Just like we discussed above, this characteristic means that part of Ni nodes has transformed into nickel oxyhydroxide and nickel hydroxide, consequently, the coordination environment has changed as well as the electron density has decreased during the electrocatalytic process. The amorphous CoNi-MOF nanosheets integrate with hybrid MOOH contributed to stabilize the spatial structure and provide lots of active sites, which play a decisive role in facilitating water oxidation.

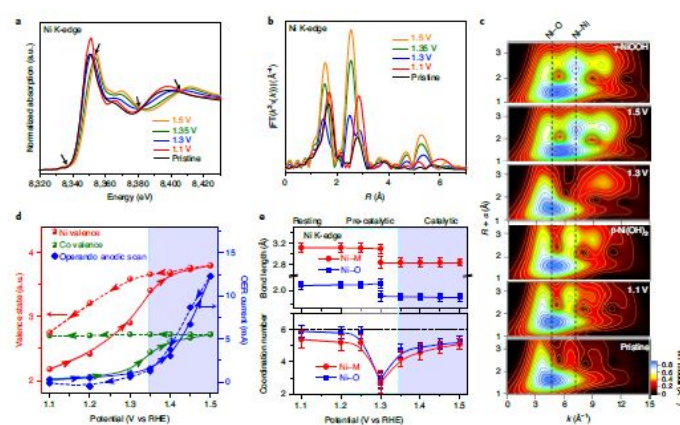


Fig.23 Operando XAS characterization of $\text{Ni}_{0.5}\text{Co}_{0.5}$ -MOF-74. a) and b), Ni K-edge XANES spectra and Fourier-transformed k^3 -weighted EXAFS signals recorded at different potentials in 1 M KOH. c), Comparison of Ni K-edge EXAFS WTs recorded for

the pristine sample, standard references and catalytic materials at 1.1, 1.3 and 1.5 V, with an optimum resolution at 3.0 Å. The vertical dashed lines are drawn to guide the eye. α denotes the phase shift. d), Change in the Ni and Co valence states and OER current as a function of applied potential. e), Changes of bond length and coordination number for the Ni–O and Ni–M coordination shells.²²⁴ Copyright © 2020 Springer Nature.

Interestingly, Tang's group selected NiCo-MOF-74 crystals as the prototypical catalysts and detected the structural transformation process during and after OER reactions by operando X-ray absorption spectroscopy analysis and high-resolution transmission electron microscopy imaging.²²⁴ As depicted in Fig. 23 (a) and (b), the arising potential revolution process can be divided into three sections: stage I is the resting period from 1.1 V to 1.2 V, the stage II is the pre-catalytic state from 1.2 V to 1.35 V, and the last stage (stage III) is the catalytic period from 1.35 V to 1.5 V, of course, the OER current up to the applied potential of 1.35 V could be neglected, which can be detected in the spectrum of synchronous electrocatalytic measurements in Fig. 23 d. After applied a series of potential on the sample, NiCo-MOF-74 has undergone a dynamical two-step reconstruction process during water oxidation, that is from NiCo-MOF-74 to the corresponding metal hydroxide and then to oxyhydroxide analogue. Both the Ni and Co

valence states and OER current display a remarkable increase, this result also indicates that the structure of NiCo-MOF-74 has been transformed into oxyhydroxide analogue during electrocatalysis, which can be attributed to the in situ-generated oxygen vacancies. The abundant oxygen vacancies and high resolution states of the final product oxyhydroxide ($\text{Vo}^{\cdot\cdot}\text{-Ni}_{0.5}\text{Co}_{0.5}\text{OOH}_{0.75}$) is responsible for its excellent OER performance. Notably, a conversion from oxyhydroxide to hydroxide and then to NiCo-MOF-74 can be observed after the potential is removed and transfer the sample to the air. These findings provides a new pathway to understand the relationship between structure conversion and OER activity during electrocatalytic experiments, as such, it also shed a light on developing composite catalysts.

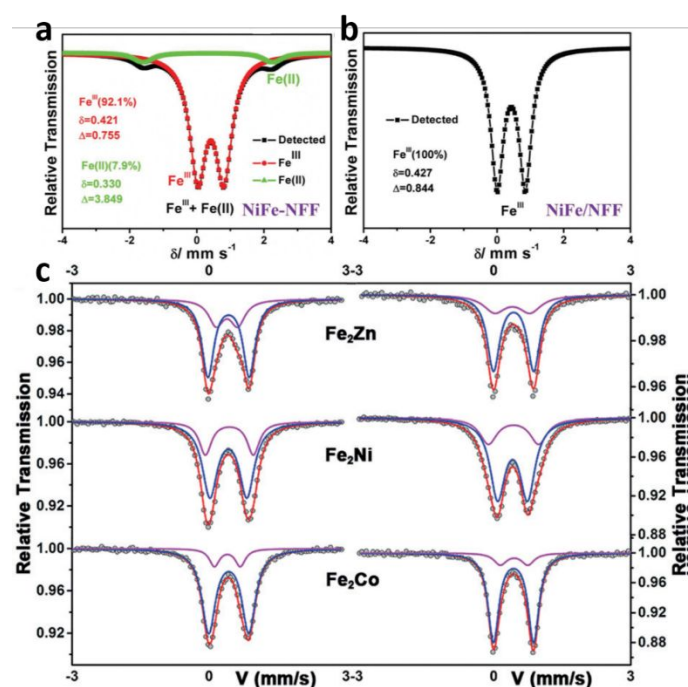


Fig. 23 ⁵⁷Fe Mössbauer spectra of a) NiFe-NFF and b) NiFe/NFF.²²⁵ Copyright © 2019 WILEY-VCH

Verlag GmbH & Co. KGaA, Weinheim. Mössbauer spectra for Fe_2M clusters (left) and the corresponding MOFs (right).²⁰⁵ Copyright © 2018 WILEY-VCH Verlag GmbH & Co. KGaA, Weinheim.

Mössbauer spectroscopy is a powerful tool to clarify the chemical state in some specific elements, such as Fe, Au, Ru, and Ir, *etc.* Zhu and co-workers investigated the electronic states of NiFe-MOF that was *in-situ* grown on nickel foam (NiFe-NFF) by using ^{57}Fe Mössbauer spectroscopy.²²⁵ In Fig. 23a, a double peak at lower velocity could correspond to the Fe ions with +3 oxidation state,²²⁶ while a weaker peak around $2.5 \delta/\text{mm s}^{-1}$ means the existence of the lower valence state Fe ions.²²⁷ Coupled with the *ex situ* XPS characterization result, which convinces that oxidation valence of Fe ions is the mixture of +2/+3, the introduction of Fe into Ni-based MOF electrocatalysts could modulate the electronic structure of 3d orbital with a form of tailoring the orbital electron density and e_g -orbital filling of Ni sites. As a consequence, which has accelerated the formation of OOH^* intermediate, meantime, endowed the NiFe-NFF catalyst superior OER performance. Lan *et al* once applied Mössbauer spectroscopy to confirm the composition of Fe_2M cluster, which still preserves after the formation of Fe_2M -BPTC MOFs, and the d-band center is closer to the Fermi level than that of Fe_3 cluster, i.e., there is a stronger binding interaction between the

adsorbates and catalyst, and further contributes to boost the OER activities.²⁰⁵ In addition, because *in situ* Fourier-transform infrared spectroscopy (FTIR) can dynamically detect function groups of the chemisorbed species on catalysts, it can conveniently be used to observe the formation of crucial intermediates.²²⁸ To study the catalytic mechanism of lattice-stained NiFe-MOF, Liu and co-workers performed *operando* SR-FTIR characterization using D_2O as the solvent.⁵⁰ Notably, a new adsorption peak located at 1048 cm^{-1} emerged in the spectroscopy of lattice-strained MOF during OER process, which can be assigned to the surface intermediate superoxide OOH^* species.²²⁹ Meanwhile, isotope-labeling *operando* SR-FTIR experiment results further confirmed this hypothesis. The XAS measurement results show the existence of Ni^{4+} species, which could coordinate with the adsorbed H_2O^* and generate the superoxide OOH^* intermediate. These could contribute positively toward excellent OER performance of the strain-latticed MOF materials.

5. Summary and Future Perspective

As summarized in this review, transition metal bimetallic MOF-based materials can be rationally fabricated into various electrocatalytic materials to achieve the enhanced OER properties. Meanwhile, the elucidation of oxygen evolution reaction mechanism in alkaline solution could deepen our

understanding of the reaction process when using MOFs or MOF-derived materials as electrocatalysts. As for bimetallic MOFs, the most popular category used as electrocatalysts is the solid solution one, in which two metal ions are delocalized or uniformly distributed in the entire MOF structure. However, many reports, especially those on 2D layer morphology MOFs, usually lack detailed characterizations to identify the accurate structure information and topology of frameworks, i.e., sometimes there is a lack of information of either two metals mixing in one SBUs or separating in different SBUs. Consequently, a thorough understanding of the water oxidation reaction mechanism may suffer some obstacles because the accurate identification of the metal distribution in bimetallic MOFs is important to adjust the electronic structures.

Although most bimetallic MOFs exhibit superior stability than the corresponding monometallic MOFs, the long-term stability still needs to be enhanced, especially in strong alkaline and acidic conditions. The crystals of bimetallic MOFs may disintegrate into discrete complexes in the electrolyte media and eventually change into the corresponding amorphous oxy/hydroxide, making elucidation of the reaction mechanism of MOF catalysts difficult. Thus, exploring stable and highly active MOF-based electrocatalysts for OER in electrolyte with a wide pH range will substantially facilitate the progress of batteries and other catalytic

reactions. It is necessary to systematically investigate the principles of synthesizing chemically and thermally stable MOFs beyond the familiar Hard-Soft-Acid-Base (HSAB) concept or coating of protective layers, which can provide guidance for synthesizing stable bimetallic MOFs.

Both pristine bimetallic MOFs and their derivatives can present good electroconductivity, however, in general, materials under study are still inadequate in terms of the requirements of practical industrial application. The good electroconductivity of electrocatalysts can accelerate the transfer of electrons, so it is urgent to exploit more conductive MOFs. Actually, the charge transport in MOFs depends on the spatial and energetic overlap between orbitals, which means enhancing the orbital overlap can effectively enhance the charge transfer ability within MOFs.²³⁰ In addition, researchers are focusing on several strategies to improve the electroconductivity of MOFs. The first is the *in-situ* growth on the conductive substrates, such as nickel foam, carbon cloth, and metal mesh. This method overcomes the limitation of intrinsic poor electroconductivity and the introduction of binder, for example, Nafion. The next is to design intrinsic electronically conductive MOFs, such as modulating π - π stacking within 3D MOF crystals, introducing redox-active organic ligands or mixed-valence-state metal centers, and constructing 2D π -conjugated MOFs with delocalized electrons.²³⁰ Lastly,

designing nanostructured MOF materials with highly exposed active sites, ultrathin structures, and the enhanced electroconductivity from abundant coordinatively unsaturated sites is necessary to obtain highly active electrocatalysts.

Moreover, bimetallic MOFs are promising precursors or templates that have been used to fabricate MOF-derived materials, including carbon composites, metal compounds and so on. The merits of MOF derivatives include the following: i) easily controlling the distribution of metal ions and doping atoms by specific tuning of structures and composites. ii) The MOF-derived skeleton with plenty of micropores and mesopores provides the transfer pathway for electrons, which is crucially important for electrocatalytic reactions. However, the structural collapse and shrinkage of MOFs during pyrolysis, calcination and other post-treatment, such as phosphorization and sulfuration usually result in the sharp decrease of surface area and pore volume. Therefore, investigating the stable matrix with resistance of various post-treatment is urgent, which will significantly improve the mass transport during OER process. For example, the use of eutectic salts as hard templates during the MOF carbonization can help prevent or reduce the pore collapse of MOF precursors.

A deeper understanding of the OER mechanism of bimetallic MOFs still needs to be pursued. For most reported bimetallic MOF-based

electrocatalysts, the active sites are usually prone to be oxidized or reduced under OER potential. Thus, the *in situ* or *operando* techniques are necessary means to track dynamic reactions during the electrocatalytic process. However, usually, most of the studies applied a single *in situ* approach, which may result in a less accurate understanding of reaction mechanism because each *in situ* operation has a specific probing mechanism and application range. Clearly, the integration of multiple advanced detection technologies, such as *in situ* TEM and XAFS are helpful in providing more information about morphological evolution and electronic structure/chemical state of the catalyst, *in situ* FTIR and Raman spectroscopy can be used to track the structural evolution of electrocatalysts during the water oxidation reaction.

It is necessary to point out that in some cases the synthesis of MOFs requires expensive organic ligands. Although the cost of ligands can sometimes be relatively high, the high cost is mainly due to the currently low market demand for such ligands, and the cost can be dramatically reduced if a large scale application can be developed. The composites of ligand are mainly C, H, O, N, and other non-metallic elements, these elements are in general affordable and readily available. So, with the popularization and application of MOFs and maturity of synthesis technology of ligands, the price of the ligands could be much lower in the near

future. What's more, the advantages of MOF-derived materials make MOFs worth investigating for the development of new functional electrocatalytic materials. In addition, continuous efforts have been made to lower the cost of MOFs and facilitate their large-scale applications. As for noble metal, such as Pt, Ir, the resources of these metals on the earth are scarce and cannot be regenerated in a short period of time, which leads to a relatively high cost of precious metals. Although precious metals are currently the first choice as industrial catalysts, in the long run, it is still necessary to develop and explore catalysts that are abundant in nature with excellent performance and low cost.

Although many challenges remain, the continued research efforts on bimetallic MOFs and their derivatives for the applications in electrocatalysis and the more profound understanding of reaction mechanism will provide an increasing amount of information to guide researchers to better design MOF-related electrocatalytic materials that will hopefully lead to their large scale industry applications.

6. Acknowledgements

The work was supported by the US Department of Energy, Office of Basic Energy Sciences, Materials Sciences and Engineering Division under Award No.

DE-SC0010596 (P.F.). Songsong Li acknowledges the support of the China Scholarship Council (CSC) for the living expenses in US.

7. Author Information

3.4 Corresponding Author

*E-mail: pingyun.feng@ucr.edu

* E-mail: gelei@cup.edu.cn

8. Conflicts of interest

There are no conflicts to declare.

9. References

1. H. Zhang and R. Lv, *Journal of Materiomics*, 2018, **4**, 95–107.
2. N. S. Lewis and D. G. Nocera, *Proceedings of the National Academy of Sciences*, 2006, **103**, 15729.
3. W. Wang, X. Xu, W. Zhou and Z. Shao, *Advanced science*, 2017, **4**, 1600371.
4. Q. Shao, J. Yang and X. Huang, *Chemistry - A European Journal*, 2018, **24**, 15143–15155.
5. Z.-F. Huang, J. Song, S. Dou, X. Li, J. Wang and X. Wang, *Matter*, 2019, **1**, 1494–1518.
6. J. Liu, H. Zhang, M. Qiu, Z. Peng, M. K. H. Leung, W.-F. Lin and J. Xuan, *Journal of Materials Chemistry A*, 2020, **8**, 2222–2245.
7. Z. Zhao, M. Li, L. Zhang, L. Dai and Z. Xia, *Advanced materials*, 2015, **27**, 6834–6840.
8. F. Lu, M. Zhou, Y. Zhou and X. Zeng, *Small*, 2017, **13**, 1701931.
9. M. S. Burke, S. Zou, L. J. Enman, J. E. Kellon, C. A. Gabor, E. Pledger and S. W. Boettcher, *The journal of physical chemistry letters*, 2015, **6**, 3737–3742.

10. W. Xia, A. Mahmood, R. Zou and Q. Xu, *Energy & Environmental Science*, 2015, **8**, 1837–1866.
11. C. Wei, S. Sun, D. Mandler, X. Wang, S. Z. Qiao and Z. J. Xu, *Chemical Society reviews*, 2019, **48**, 2518–2534.
12. H. B. Aiyappa, J. Masa, C. Andronescu, M. Muhler, R. A. Fischer and W. Schuhmann, *Small Methods*, 2019, **3**, 1800415.
13. Q. Shi, S. Fu, C. Zhu, J. Song, D. Du and Y. Lin, *Materials horizons*, 2019, **6**, 684–702.
14. X. Zhao, M. S. Shimazu, X. Chen, X. Bu and P. Feng, *Angewandte Chemie International Edition*, 2018, **57**, 6208–6211.
15. Y. Wang, X. Zhao, H. Yang, X. Bu, Y. Wang, X. Jia, J. Li and P. Feng, *Angewandte Chemie International Edition*, 2019, **58**, 6316–6320.
16. Y.-P. Yuan, L.-S. Yin, S.-W. Cao, G.-S. Xu, C.-H. Li and C. Xue, *Applied Catalysis B: Environmental*, 2015, **168–169**, 572–576.
17. X. Zhao, Y. Wang, D.-S. Li, X. Bu and P. Feng, *Advanced materials*, 2018, **30**, 1705189.
18. W. Zhou, D.-D. Huang, Y.-P. Wu, J. Zhao, T. Wu, J. Zhang, D.-S. Li, C. Sun, P. Feng and X. Bu, *Angewandte Chemie International Edition*, 2019, **58**, 4227–4231.
19. T. Rodenas, S. Beeg, I. Spanos, S. Neugebauer, F. Girgsdies, G. Algara - Siller, P. P. M. Schlekler, P. Jakes, N. Pfänder and M. Willinger, *Advanced Energy Materials*, 2018, **8**, 1802404.
20. X. Gao, S. Delacruz, C. Zhu, S. Cheng, D. Gardner, Y. Xie, C. Carraro and R. Maboudian, *Carbon*, 2019, **148**, 64–71.
21. H. B. Aiyappa, P. Wilde, T. Quast, J. Masa, C. Andronescu, Y. T. Chen, M. Muhler, R. A. Fischer and W. Schuhmann, *Angewandte Chemie International Edition*, 2019, **58**, 8927–8931.
22. Z. Gao, Z. W. Yu, F. Q. Liu, C. Yang, Y. H. Yuan, Y. Yu and F. Luo, *ChemSusChem*.
23. D. Senthil Raja, X.-F. Chuah and S.-Y. Lu, *Advanced Energy Materials*, 2018, **8**, 1801065.
24. F. Sun, G. Wang, Y. Ding, C. Wang, B. Yuan and Y. Lin, *Advanced Energy Materials*, 2019, **11**, 1800584.
25. F. Zheng, Z. Zhang, D. Xiang, P. Li, C. Du, Z. Zhuang, X. Li and W. Chen, *Journal of colloid and interface science*, 2019, **555**, 541–547.
26. X. Fang, L. Jiao, S. H. Yu and H. L. Jiang, *ChemSusChem*, 2017, **10**, 3019–3024.
27. L. Yang, S. Feng, G. Xu, B. Wei and L. Zhang, *ACS sustainable chemistry & engineering*, 2019, **7**, 5462–5475.
28. D. S. Raja, H.-W. Lin and S.-Y. Lu, *Nano Energy*, 2019, **57**, 1–13.
29. E. A. Dolgoplova, A. J. Brandt, O. A. Ejegbavwo, A. S. Duke, T. D. Maddumapatabandi, R. P. Galhenage, B. W. Larson, O. G. Reid, S. C. Ammal and A. Heyden, *Journal of the American Chemical Society*, 2017, **139**, 5201–5209.
30. S. Zhao, Y. Wang, J. Dong, C.-T. He, H. Yin, P. An, K. Zhao, X. Zhang, C. Gao and L. Zhang, *Nature Energy*, 2016, **1**, 1–10.
31. L. Zhuang, L. Ge, H. Liu, Z. Jiang, Y. Jia, Z. Li, D. Yang, R. K. Hocking, M. Li and L. Zhang, *Angewandte Chemie*, 2019.
32. W. Cheng, X. F. Lu, D. Luan and X. W. Lou, *Angewandte Chemie International Edition*, 2020, **59**, 18234–18239.
33. C. G. Morales-Guio, L.-A. Stern and X. Hu, *Chemical Society reviews*, 2014, **43**, 6555–6569.
34. H. Sun, Z. Yan, F. Liu, W. Xu, F. Cheng and J. Chen, *Advanced materials*, 2020, **32**, 1806326.
35. J. Du, F. Li and L. Sun, *Chemical Society reviews*.
36. M. Xie, Y. Ma, D. Lin, C. Xu, F. Xie and W. Zeng, *Nanoscale*, 2020, **12**, 67–71.
37. W. Chen, X. Zhu, Y. Zhang, Y. Zhou and K. K. Ostrikov, *ACS sustainable chemistry & engineering*, 2021, **9**, 4, 1826–1836.
38. P. Thangavel, M. Ha, S. Kumaraguru, A. Meena, A. N. Singh, A. M. Harzandi and K. S. Kim, *Energy & Environmental Science*, 2020, **13**, 3447–3458.
39. Q. Zha, M. Li, Z. Liu and Y. Ni, *ACS sustainable chemistry & engineering*, 2020, **8**, 12025–12035.
40. T. Liu, P. Li, N. Yao, T. Kong, G. Cheng, S. Chen and W. Luo, *Advanced materials*, 2019,

- 31, 1806672.
41. Y. Liu, G. Li, J. Fu, Z. Chen and X. Peng, *Angewandte Chemie*, 2017, **129**, 6272–6276.
 42. Y. Du, Y. Han, X. Huai, Y. Liu, C. Wu, Y. Yang and L. Wang, *International Journal of Hydrogen Energy*, 2018, **43**, 22226–22234.
 43. A. Fan, C. Qin, X. Zhang, X. Dai, Z. Dong, C. Luan, L. Yu, J. Ge and F. Gao, *ACS sustainable chemistry & engineering*, 2018, **7**, 2285–2295.
 44. Y. Li, M. Lu, P. He, Y. Wu, J. Wang, D. Chen, H. Xu, J. Gao and J. Yao, *Chemistry – An Asian Journal*, 2019, **14**, 1590–1594.
 45. L. Du, L. Xing, G. Zhang and S. Sun, *Carbon*, 2020, **156**, 77–92.
 46. A. Zitolo, V. Goellner, V. Armel, M.–T. Sougrati, T. Mineva, L. Stievano, E. Fonda and F. Jaouen, *Nature materials*, 2015, **14**, 937–942.
 47. W. T. Hong, M. Risch, K. A. Stoerzinger, A. Grimaud, J. Suntivich and Y. Shao–Horn, *Energy & Environmental Science*, 2015, **8**, 1404–1427.
 48. N.–T. Suen, S.–F. Hung, Q. Quan, N. Zhang, Y.–J. Xu and H. M. Chen, *Chemical Society reviews*, 2017, **46**, 337–365.
 49. J. D. Benck, T. R. Hellstern, J. Kibsgaard, P. Chakthranont and T. F. Jaramillo, *Acs Catalysis*, 2014, **4**, 3957–3971.
 50. W. Cheng, X. Zhao, H. Su, F. Tang, W. Che, H. Zhang and Q. Liu, *Nature Energy*, 2019, **4**, 115–122.
 51. Q. Wang, F. Liu, C. Wei, D. Li, W. Guo and Q. Zhao, *ChemistrySelect*, 2019, **4**, 5988–5994.
 52. W.–H. Li, J. Lv, Q. Li, J. Xie, N. Ogiwara, Y. Huang, H. Jiang, H. Kitagawa, G. Xu and Y. Wang, *Journal of Materials Chemistry A*, 2019, **7**, 10431–10438.
 53. Z. Shi, Y. Wang, H. Lin, H. Zhang, M. Shen, S. Xie, Y. Zhang, Q. Gao and Y. Tang, *Journal of Materials Chemistry A*, 2016, **4**, 6006–6013.
 54. X. Li, Y. Fang, X. Lin, M. Tian, X. An, Y. Fu, R. Li, J. Jin and J. Ma, *Journal of Materials Chemistry A*, 2015, **3**, 17392–17402.
 55. M. Faraji, M. Yousefi, S. Yousefzadeh, M. Zirak, N. Naseri, T. H. Jeon, W. Choi and A. Z. Moshfegh, *Energy & Environmental Science*, 2019, **12**, 59–95.
 56. S. Dou, X. Wang and S. Wang, *Small Methods*, 2019, **3**, 1800211.
 57. Z. P. Wu, X. F. Lu, S. Q. Zang and X. W. Lou, *Advanced Functional Materials*, 2020, **30**, 1910274.
 58. C. Jiang, S. J. Moniz, A. Wang, T. Zhang and J. Tang, *Chemical Society reviews*, 2017, **46**, 4645–4660.
 59. C. C. L. McCrory, S. Jung, I. M. Ferrer, S. M. Chatman, J. C. Peters and T. F. Jaramillo, *Journal of the American Chemical Society*, 2015, **137**, 4347–4357.
 60. C. Wei and Z. J. Xu, *Small Methods*, 2018, **2**, 1800168.
 61. J.–F. Qin, M. Yang, S. Hou, B. Dong, T.–S. Chen, X. Ma, J.–Y. Xie, Y.–N. Zhou, J. Nan and Y.–M. Chai, *Applied Surface Science*, 2020, **502**, 144172.
 62. Y.–K. Li, G. Zhang, W.–T. Lu and F.–F. Cao, *Advanced science*, 2020, **7**, 1902034.
 63. Y. Ma, Z. Lu, S. Li, J. Wu, J. Wang, Y. Du, J. Sun and P. Xu, *ACS applied materials & interfaces*, 2020, **12**, 12668–12676.
 64. Y. Wan, Z. Zhang, X. Xu, Z. Zhang, P. Li, X. Fang, K. Zhang, K. Yuan, K. Liu and G. Ran, *Nano Energy*, 2018, **51**, 786–792.
 65. J. Tafel, *Z. Phys. Chem*, 1905, **50**, 641.
 66. A. Damjanovic, A. Dey and B. JO’M, *Electrochimica Acta*, 1966, **11**, 791–814.
 67. H. Feng, L. Tang, G. Zeng, J. Yu, Y. Deng, Y. Zhou, J. Wang, C. Feng, T. Luo and B. Shao, *Nano Energy*, 2020, **67**, 104174.
 68. S. Anantharaj, S. Ede, K. Karthick, S. S. Sankar, K. Sangeetha, P. Karthik and S. Kundu, *Energy & Environmental Science*, 2018, **11**, 744–771.
 69. M. B. Stevens, L. J. Enman, A. S. Batchellor, M. R. Cosby, A. E. Vise, C. D. Trang and S. W. Boettcher, *Chemistry of Materials*, 2017, **29**, 120–140.
 70. Q. Qian, Y. Li, Y. Liu, L. Yu and G. Zhang, *Advanced materials*, 2019, **31**, 1901139.
 71. A. Xie, J. Du, F. Tao, Y. Tao, Z. Xiong, S. Luo, X. Li and C. Yao, *Electrochimica Acta*,

- 2019, **305**, 338–348.
72. Y. Tang, T. Chen and S. Yu, *Chemical communications*, 2015, **51**, 9018–9021.
73. L. Dai, Z.-N. Chen, L. Li, P. Yin, Z. Liu and H. Zhang, *Advanced materials*, 2020, **32**, 1906915.
74. H. Feng, L. Tang, G. Zeng, J. Yu, Y. Deng, Y. Zhou, J. Wang, C. Feng, T. Luo and B. Shao, *Nano Energy*, 2019, 104174.
75. X. F. Lu, L. Yu and X. W. Lou, *Science advances*, 2019, **5**, eaav6009.
76. M. Guo, Y. Li, L. Zhou, Q. Zheng, W. Jie, F. Xie, C. Xu and D. Lin, *Electrochimica Acta*, 2019, **298**, 525–532.
77. X. Zhang, J. Luo, K. Wan, D. Plessers, B. Sels, J. Song, L. Chen, T. Zhang, P. Tang, J. R. Morante, J. Arbiol and J. Fransaer, *Journal of Materials Chemistry A*, 2019, **7**, 1616–1628.
78. D. Sun, W. Liu, M. Qiu, Y. Zhang and Z. Li, *Chemical communications*, 2015, **51**, 2056–2059.
79. L. Feng, K.-Y. Wang, G. S. Day and H.-C. Zhou, *Chemical Society reviews*, 2019, **48**, 4823–4853.
80. Q.-G. Zhai, X. Bu, C. Mao, X. Zhao and P. Feng, *Journal of the American Chemical Society*, 2016, **138**, 2524–2527.
81. L. Chen, H.-F. Wang, C. Li and Q. Xu, *Chemical science*, 2020, **11**, 5369–5403.
82. S. Wongsakulphasatch, F. Nouar, J. Rodriguez, L. Scott, C. Le Guillouzer, T. Devic, P. Horcajada, J.-M. Grenèche, P. Llewellyn and A. Vimont, *Chemical communications*, 2015, **51**, 10194–10197.
83. S.-T. Zheng, T. Wu, C. Chou, A. Fuhr, P. Feng and X. Bu, *Journal of the American Chemical Society*, 2012, **134**, 4517–4520.
84. N. Al Amery, H. R. Abid, S. Al-Saadi, S. Wang and S. Liu, *Materials Today Chemistry*, 2020, **17**, 100343.
85. Y. Sun and H.-C. Zhou, *Science and technology of advanced materials*, 2015, **16**, 054202.
86. M. Dinca and J. R. Long, *Journal of the American Chemical Society*, 2007, **129**, 11172–11176.
87. X. Yang and Q. Xu, *Crystal Growth & Design*, 2017, **17**, 1450–1455.
88. S. Yuan, J.-S. Qin, J. Li, L. Huang, L. Feng, Y. Fang, C. Lollar, J. Pang, L. Zhang and D. Sun, *Nature communications*, 2018, **9**, 1–11.
89. O. Kozachuk, M. Meilikhov, K. Yussenko, A. Schneemann, B. Jee, A. V. Kuttatheyil, M. Bertmer, C. Sternemann, A. Pöppl and R. A. Fischer, *European Journal of Inorganic Chemistry*, 2013, **2013**.
90. B. Garai, V. Bon, S. Krause, F. Schwotzer, M. Gerlach, I. Senkovska and S. Kaskel, *Chemistry of Materials*, 2020, **32**, 889–896.
91. J.-Q. Shen, P.-Q. Liao, D.-D. Zhou, C.-T. He, J.-X. Wu, W.-X. Zhang, J.-P. Zhang and X.-M. Chen, *Journal of the American Chemical Society*, 2017, **139**, 1778–1781.
92. G. Férey, C. Mellot-Draznieks, C. Serre, F. Millange, J. Dutour, S. Surblé and I. Margiolaki, *Science*, 2005, **309**, 2040–2042.
93. K. Wang, D. Feng, T.-F. Liu, J. Su, S. Yuan, Y.-P. Chen, M. Bosch, X. Zou and H.-C. Zhou, *Journal of the American Chemical Society*, 2014, **136**, 13983–13986.
94. S. Lee, E. A. Kapustin and O. M. Yaghi, *Science*, 2016, **353**, 808–811.
95. C. C. McCrory, S. Jung, J. C. Peters and T. F. Jaramillo, *Journal of the American Chemical Society*, 2013, **135**, 16977–16987.
96. C. Li, G. Wang, K. Li, Y. Liu, B. Yuan and Y. Lin, *ACS applied materials & interfaces*, 2019.
97. S. Zhao, R. Jin, H. Abroshan, C. Zeng, H. Zhang, S. D. House, E. Gottlieb, H. J. Kim, J. C. Yang and R. Jin, *Journal of the American Chemical Society*, 2017, **139**, 1077–1080.
98. F. L. Li, P. Wang, X. Huang, D. J. Young, H. F. Wang, P. Braunstein and J. P. Lang, *Angewandte Chemie*, 2019, **131**, 7125–7130.
99. X. Li, D. D. Ma, C. Cao, R. Zou, Q. Xu, X. T. Wu and Q. L. Zhu, *Small*, 2019, **15**, 1902218.
100. Q. Ji, Y. Kong, C. Wang, H. Tan, H. Duan, W. Hu, G. Li, Y. Lu, N. Li and Y. Wang, *ACS Catalysis*, 2020, **10**, 5691–5697.

101. S. Zhao, Y. Wang, J. Dong, C.-T. He, H. Yin, P. An, K. Zhao, X. Zhang, C. Gao, L. Zhang, J. Lv, J. Wang, J. Zhang, A. M. Khattak, N. A. Khan, Z. Wei, J. Zhang, S. Liu, H. Zhao and Z. Tang, *Nature Energy*, 2016, **1**, 16184.
102. L. Huang, G. Gao, H. Zhang, J. Chen, Y. Fang and S. Dong, *Nano Energy*, 2020, **68**, 104296.
103. D.-J. Li, Q.-H. Li, Z.-G. Gu and J. Zhang, *Journal of Materials Chemistry A*, 2019, **7**, 18519-18528.
104. L.-L. Feng, G. Yu, Y. Wu, G.-D. Li, H. Li, Y. Sun, T. Asefa, W. Chen and X. Zou, *Journal of the American Chemical Society*, 2015, **137**, 14023-14026.
105. B. You, X. Liu, N. Jiang and Y. Sun, *Journal of the American Chemical Society*, 2016, **138**, 13639-13646.
106. B. Wang, J. Shang, C. Guo, J. Zhang, F. Zhu, A. Han and J. Liu, *Small*, 2019, **15**, 1804761.
107. Y. Zhao, X. Zhang, X. Jia, G. I. Waterhouse, R. Shi, X. Zhang, F. Zhan, Y. Tao, L. Z. Wu and C. H. Tung, *Advanced Energy Materials*, 2018, **8**, 1703585.
108. B. Wang, M. Zhao, L. Li, Y. Huang, X. Zhang, C. Guo, Z. Zhang, H. Cheng, W. Liu, J. Shang, J. Jin, X. Sun, J. Liu and H. Zhang, *National Science Review*, 2019, **7**, 46-52.
109. A. J. Clough, J. W. Yoo, M. H. Mecklenburg and S. C. Marinescu, *Journal of the American Chemical Society*, 2015, **137**, 118-121.
110. B. Wurster, D. Grumelli, D. Hötger, R. Gutzler and K. Kern, *Journal of the American Chemical Society*, 2016, **138**, 3623-3626.
111. K. Rui, G. Zhao, Y. Chen, Y. Lin, Q. Zhou, J. Chen, J. Zhu, W. Sun, W. Huang and S. X. Dou, *Advanced Functional Materials*, 2018, **28**, 1801554.
112. J.-N. Lu, J. Liu, L.-Z. Dong, S.-L. Li, Y.-H. Kan and Y.-Q. Lan, *Chemistry - A European Journal*, 2019, **25**, 15830-15836.
113. X. Zhao, X. Bu, E. T. Nguyen, Q.-G. Zhai, C. Mao and P. Feng, *Journal of the American Chemical Society*, 2016, **138**, 15102-15105.
114. W. Li, S. Xue, S. Watzele, S. Hou, J. Fichtner, A. L. Semrau, L. Zhou, A. Welle, A. S. Bandarenka and R. A. Fischer, *Angewandte Chemie International Edition*, 2020, **59**, 5837-5843.
115. B. Iqbal, M. Saleem, S. N. Arshad, J. Rashid, N. Hussain and M. Zaheer, *Chemistry - A European Journal*, 2019, **25**, 10490-10498.
116. Z. Xue, Y. Li, Y. Zhang, W. Geng, B. Jia, J. Tang, S. Bao, H.-P. Wang, Y. Fan, Z.-w. Wei, Z. Zhang, Z. Ke, G. Li and C.-Y. Su, *Advanced Energy Materials*, 2018, **8**, 1801564.
117. Y. Zhu, L. Peng, Z. Fang, C. Yan, X. Zhang and G. Yu, *Advanced materials*, 2018, **30**, 1706347.
118. H. Furukawa, U. Müller and O. M. Yaghi, *Angewandte Chemie International Edition*, 2015, **54**, 3417-3430.
119. L. Zhuang, L. Ge, H. Liu, Z. Jiang, Y. Jia, Z. Li, D. Yang, R. K. Hocking, M. Li and L. Zhang, *Angewandte Chemie*, 2019, **131**, 13699-13706.
120. M. Zhao, Q. Lu, Q. Ma and H. Zhang, *Small Methods*, 2017, **1**, 1600030.
121. G. Zhan and H. C. Zeng, *Advanced Functional Materials*, 2016, **26**, 3268-3281.
122. X. Bai, H. Chen, Y. Li, L. Shao, J. Ma, L. Li, J. Chen, T. Wang, X. Zhang and L. Zhang, *New Journal of Chemistry*, 2020, **44**, 1694-1698.
123. Z. Wan, D. Yang, J. Chen, J. Tian, T. T. Isimjan and X. Yang, *ACS Applied Nano Materials*, 2019, **2**, 6334-6342.
124. X. T. Ling, F. Du, Y. T. Zhang, Y. Shen, T. Li, A. Alsaedi, T. Hayat, Y. Zhou and Z. G. Zou, *RSC advances*, 2019, **9**, 33558-33562.
125. M. W. Xie, Y. Ma, D. M. Lin, C. G. Xu, F. Y. Xie and W. Zeng, *Nanoscale*, 2020, **12**, 67-71.
126. W. Li, W. Fang, C. Wu, K. N. Dinh, H. Ren, L. Zhao, C. Liu and Q. Yan, *Journal of Materials Chemistry A*, 2020, **8**, 3658-3666.
127. J. Xu, X. Zhu and X. Jia, *ACS sustainable chemistry & engineering*, 2019, **7**, 16629-16639.
128. G. Hai, X. Jia, K. Zhang, X. Liu, Z. Wu and G. Wang, *Nano Energy*, 2018, **44**, 345-352.
129. C. Li, Y. Liu, G. Wang, L. Guan and Y. Lin, *ACS sustainable chemistry & engineering*,

- 2019, **7**, 7496–7501.
130. L. Yang, G. Zhu, H. Wen, X. Guan, X. Sun, H. Feng, W. Tian, D. Zheng, X. Cheng and Y. Yao, *Journal of Materials Chemistry A*, 2019, **7**, 8771–8776.
131. F. Zheng, D. Xiang, P. Li, Z. Zhang, C. Du, Z. Zhuang, X. Li and W. Chen, *ACS sustainable chemistry & engineering*, 2019, **7**, 9743–9749.
132. S. Luo, R. Gu, P. Shi, J. Fan, Q. Xu and Y. Min, *Journal of Power Sources*, 2020, **448**, 227406.
133. Z. Zou, T. Wang, X. Zhao, W.-J. Jiang, H. Pan, D. Gao and C. Xu, *ACS Catalysis*, 2019, **9**, 7356–7364.
134. J. Du, S. Xu, L. Sun and F. Li, *Chemical communications*, 2019, **55**, 14773–14776.
135. M. Lu, Y. Li, P. He, J. Cong, D. Chen, J. Wang, Y. Wu, H. Xu, J. Gao and J. Yao, *Journal of Solid State Chemistry*, 2019, **272**, 32–37.
136. H.-W. Lin, D. Senthil Raja, X.-F. Chuah, C.-T. Hsieh, Y.-A. Chen and S.-Y. Lu, *Applied Catalysis B: Environmental*, 2019, **258**, 118023.
137. Z. Chen, B. Fei, M. Hou, X. Yan, M. Chen, H. Qing and R. Wu, *Nano Energy*, 2020, **68**, 104371.
138. J. Li, W. Huang, M. Wang, S. Xi, J. Meng, K. Zhao, J. Jin, W. Xu, Z. Wang, X. Liu, Q. Chen, L. Xu, X. Liao, Y. Jiang, K. A. Owusu, B. Jiang, C. Chen, D. Fan, L. Zhou and L. Mai, *ACS Energy Letters*, 2019, **4**, 285–292.
139. M. Cai, Q. Liu, Z. Xue, Y. Li, Y. Fan, A. Huang, M.-R. Li, M. Croft, T. A. Tyson, Z. Ke and G. Li, *Journal of Materials Chemistry A*, 2020, **8**, 190–195.
140. B. N. Khiarak, M. Hasanzadeh, M. Mojaddami, H. Shahriyar Far and A. Simchi, *Chemical communications*, 2020, **56**, 3135–3138.
141. C. Wang, J. Kim, J. Tang, M. Kim, H. Lim, V. Malgras, J. You, Q. Xu, J. Li and Y. Yamauchi, *Chem*, 2020, **6**, 19–40.
142. H.-F. Wang, L. Chen, H. Pang, S. Kaskel and Q. Xu, *Chemical Society reviews*, 2020, **49**, 1414–1448.
143. Z. Xie, H. Tang and Y. Wang, *ChemElectroChem*, 2019, **6**, 1206–1212.
144. K. Gong, F. Du, Z. Xia, M. Durstock and L. Dai, *Science*, 2009, **323**, 760–764.
145. X. Cui, P. Ren, D. Deng, J. Deng and X. Bao, *Energy & Environmental Science*, 2016, **9**, 123–129.
146. S. A. Shah, Z. Ji, X. Shen, X. Yue, G.-X. Zhu, K. Xu, A. Yuan, N. Ullah, J. Zhu and P. Song, *ACS Applied Energy Materials*, 2019, **2**, 4073–4083.
147. Z. Guo, F. Wang, Z. Li, Y. Yang, A. G. Tamirat, H. Qi, J. Han, W. Li, L. Wang and S. Feng, *Journal of Materials Chemistry A*, 2018, **6**, 22096–22105.
148. J. Sheng, L. Wang, L. Deng, M. Zhang, H. He, K. Zeng, F. Tang and Y.-N. Liu, *ACS applied materials & interfaces*, 2018, **10**, 7191–7200.
149. C. Feng, Y. Guo, Y. Xie, X. Cao, S. Li, L. Zhang, W. Wang and J. Wang, *Nanoscale*, 2020, **12**, 5942–5952.
150. Y. Feng, X.-Y. Yu and U. Paik, *Chemical communications*, 2016, **52**, 6269–6272.
151. C.-L. Zhang, B.-R. Lu, F.-H. Cao, Z.-L. Yu, H.-P. Cong and S.-H. Yu, *Journal of Materials Chemistry A*, 2018, **6**, 12962–12968.
152. Y. Li, S. Chen, D. Xi, Y. Bo, R. Long, C. Wang, L. Song and Y. Xiong, *Small*, 2018, **14**, 1702109.
153. J. Meng, C. Niu, L. Xu, J. Li, X. Liu, X. Wang, Y. Wu, X. Xu, W. Chen and Q. Li, *Journal of the American Chemical Society*, 2017, **139**, 8212–8221.
154. A. B. Jorge, R. Jervis, A. P. Periasamy, M. Qiao, J. Feng, L. N. Tran and M.-M. Titirici, *Advanced Energy Materials*, 2020, **10**, 1902494.
155. Y. Shen, L. Wang, P. Jiang, W. S. V. Lee and J. Xue, *ChemElectroChem*, 2019, **6**, 2741–2747.
156. X. Wang, L. Chai, J. Ding, L. Zhong, Y. Du, T.-T. Li, Y. Hu, J. Qian and S. Huang, *Nano Energy*, 2019, **62**, 745–753.
157. W. Hong, M. Kitta and Q. Xu, *Small Methods*, 2018, **2**, 1800214.
158. Y. P. Zhu, Y. Jing, A. Vasileff, T. Heine and S. Z. Qiao, *Advanced Energy Materials*, 2017, **7**, 1602928.
159. A. Dutta, A. K. Samantara, S. K. Dutta, B.

- K. Jena and N. Pradhan, *ACS Energy Letters*, 2016, **1**, 169–174.
160. D. Xiong, X. Wang, W. Li and L. Liu, *Chemical communications*, 2016, **52**, 8711–8714.
161. R. Subbaraman, D. Tripkovic, K.-C. Chang, D. Strmcnik, A. P. Paulikas, P. Hirunsit, M. Chan, J. Greeley, V. Stamenkovic and N. M. Markovic, *Nature materials*, 2012, **11**, 550–557.
162. J. Joo, T. Kim, J. Lee, S.-I. Choi and K. Lee, *Advanced materials*, 2019, **31**, 1806682.
163. Z. Jin, P. Li and D. Xiao, *Green Chemistry*, 2016, **18**, 1459–1464.
164. Z. Yang, L. Liu, X. Wang, S. Yang and X. Su, *Journal of alloys and compounds*, 2011, **509**, 165–171.
165. S. S. Li, L. Wang, S. Liu, B. R. Xu, N. Xiao, Y. Q. Gao, W. Y. Song, L. Ge and J. Liu, *ACS sustainable chemistry & engineering*, 2018, **6**, 9940–9950.
166. J. Ryu, N. Jung, J. H. Jang, H.-J. Kim and S. J. Yoo, *Acs Catalysis*, 2015, **5**, 4066–4074.
167. C. Guan, W. Xiao, H. Wu, X. Liu, W. Zang, H. Zhang, J. Ding, Y. P. Feng, S. J. Pennycook and J. Wang, *Nano Energy*, 2018, **48**, 73–80.
168. A. Mahmood, W. Guo, H. Tabassum and R. Zou, *Advanced Energy Materials*, 2016, **6**, 1600423.
169. H. Sun, Y. Min, W. Yang, Y. Lian, L. Lin, K. Feng, Z. Deng, M. Chen, J. Zhong and L. Xu, *ACS Catalysis*, 2019, **9**, 8882–8892.
170. Y. Jiao, Y. Zheng, M. Jaroniec and S. Z. Qiao, *Chemical Society reviews*, 2015, **44**, 2060–2086.
171. D. K. Zhong and D. R. Gamelin, *Journal of the American Chemical Society*, 2010, **132**, 4202–4207.
172. Y. Wang, S. Zhao, Y. Zhu, R. Qiu, T. Gengenbach, Y. Liu, L. Zu, H. Mao, H. Wang, J. Tang, D. Zhao and C. Selomulya, *iScience*, 2020, **23**, 100761.
173. C. Lin, D. Wang, H. Jin, P. Wang, D. Chen, B. Liu and S. Mu, *Journal of Materials Chemistry A*, 2020, **8**, 4570–4578.
174. H. Zhou, F. Yu, J. Sun, R. He, S. Chen, C.-W. Chu and Z. Ren, *Proceedings of the National Academy of Sciences*, 2017, **114**, 5607–5611.
175. L. Zhang, X. Wang, A. Li, X. Zheng, L. Peng, J. Huang, Z. Deng, H. Chen and Z. Wei, *Journal of Materials Chemistry A*, 2019, **7**, 17529–17535.
176. S. Anantharaj, S. R. Ede, K. Sakthikumar, K. Karthick, S. Mishra and S. Kundu, *Acs Catalysis*, 2016, **6**, 8069–8097.
177. L. Peng, S. S. A. Shah and Z. Wei, *Chinese Journal of Catalysis*, 2018, **39**, 1575–1593.
178. D. Wang, L. Tian, J. Huang, D. Li, J. Liu, Y. Xu, H. Ke and Q. Wei, *Electrochimica Acta*, 2020, **334**, 135636.
179. W. Liu, H. Niu, J. Yang, K. Cheng, K. Ye, K. Zhu, G. Wang, D. Cao and J. Yan, *Chemistry of Materials*, 2018, **30**, 1055–1068.
180. T. Liu, F. Yang, G. Cheng and W. Luo, *Small*, 2018, **14**, 1703748.
181. J. Yang, G. Zhu, Y. Liu, J. Xia, Z. Ji, X. Shen and S. Wu, *Advanced Functional Materials*, 2016, **26**, 4712–4721.
182. W.-D. Zhang, X. Yan, T. Li, Y. Liu, Q.-T. Fu and Z.-G. Gu, *Chemical communications*, 2019, **55**, 5467–5470.
183. M. Gong, Y. Li, H. Wang, Y. Liang, J. Z. Wu, J. Zhou, J. Wang, T. Regier, F. Wei and H. Dai, *Journal of the American Chemical Society*, 2013, **135**, 8452–8455.
184. J. Chen, F. Zheng, S.-J. Zhang, A. Fisher, Y. Zhou, Z. Wang, Y. Li, B.-B. Xu, J.-T. Li and S.-G. Sun, *ACS Catalysis*, 2018, **8**, 11342–11351.
185. X. Hu, S. Zhang, J. Sun, L. Yu, X. Qian, R. Hu, Y. Wang, H. Zhao and J. Zhu, *Nano Energy*, 2019, **56**, 109–117.
186. K. Qin, L. Wang, S. Wen, L. Diao, P. Liu, J. Li, L. Ma, C. Shi, C. Zhong and W. Hu, *Journal of Materials Chemistry A*, 2018, **6**, 8109–8119.
187. J. Tian, F. Jiang, D. Yuan, L. Zhang, Q. Chen and M. Hong, *Angewandte Chemie International Edition*, 2020, **59**, 13101.
188. M. Liu, L. Kong, X. Wang, J. He and X. H. Bu, *Small*, 2019, 1903410.
189. H. Lei, Z. Wang, F. Yang, X. Huang, J. Liu, Y. Liang, J. Xie, M. S. Javed, X. Lu, S. Tan

- and W. Mai, *Nano Energy*, 2020, **68**, 104293.
190. X. Wang, L. Yu, B. Y. Guan, S. Song and X. W. Lou, *Advanced materials*, 2018, **30**, 1801211.
191. J. Huang, P. Xu, T. Gao, J. Huangfu, X.-j. Wang, S. Liu, Y. Zhang and B. Song, *ACS sustainable chemistry & engineering*, 2020, **8**, 1319-1328.
192. C. Lin, D. Q. Wang, H. H. Jin, P. Y. Wang, D. Chen, B. S. Liu and S. C. Mu, *Journal Of Materials Chemistry A*, 2020, **8**, 4570-4578.
193. M. Jiang, J. Li, X. Cai, Y. Zhao, L. Pan, Q. Cao, D. Wang and Y. Du, *Nanoscale*, 2018, **10**, 19774-19780.
194. C.-N. Lv, L. Zhang, X.-H. Huang, Y.-X. Zhu, X. Zhang, J.-S. Hu and S.-Y. Lu, *Nano Energy*, 2019, **65**, 103995.
195. C. Xuan, J. Wang, W. Xia, Z. Peng, Z. Wu, W. Lei, K. Xia, H. L. Xin and D. Wang, *ACS applied materials & interfaces*, 2017, **9**, 26134-26142.
196. L.-M. Cao, Y.-W. Hu, S.-F. Tang, A. Iljin, J.-W. Wang, Z.-M. Zhang and T.-B. Lu, *Advanced science*, 2018, **5**, 1800949.
197. Y. Shen, L. Wang, P. Jiang, W. S. V. Lee and J. Xue, *ChemElectroChem*, 2019, **6**, 2741-2747.
198. Z. Haiyuan, H. Bowen, K. Panyong, Y. Jiaguo and F. Ke, *ACS applied materials & interfaces*, 2018, **10**, 22311-22319.
199. W. Zhu, T. Zhang, Y. Zhang, Z. Yue, Y. Li, R. Wang, Y. Ji, X. Sun and J. Wang, *Applied Catalysis B: Environmental*, 2019, **244**, 844-852.
200. C. Qin, A. Fan, D. Ren, C. Luan, J. Yang, Y. Liu, X. Zhang, X. Dai and M. Wang, *Electrochimica Acta*, 2019, **323**, 134756.
201. H. A. Hansen, V. Viswanathan and J. K. Nørskov, *The Journal of Physical Chemistry C*, 2014, **118**, 6706-6718.
202. J. K. Nørskov, J. Rossmeisl, A. Logadottir, L. Lindqvist, J. R. Kitchin, T. Bligaard and H. Jonsson, *The Journal of Physical Chemistry B*, 2004, **108**, 17886-17892.
203. H. B. Tao, J. Zhang, J. Chen, L. Zhang, Y. Xu, J. G. Chen and B. Liu, *Journal of the American Chemical Society*, 2019, **141**, 13803-13811.
204. Y. Zhu, J. Wang, H. Chu, Y.-C. Chu and H. M. Chen, *ACS Energy Letters*, 2020, **5**, 1281-1291.
205. X.-L. Wang, L.-Z. Dong, M. Qiao, Y.-J. Tang, J. Liu, Y. Li, S.-L. Li, J.-X. Su and Y.-Q. Lan, *Angewandte Chemie*, 2018, **130**, 9808-9812.
206. J. O. M. Bockris and T. Otagawa, *The Journal of Physical Chemistry*, 2002, **87**, 2960-2971.
207. I. C. Man, H. Y. Su, F. Calle - Vallejo, H. A. Hansen, J. I. Martinez, N. G. Inoglu, J. Kitchin, T. F. Jaramillo, J. K. Nørskov and J. Rossmeisl, *ChemCatChem*, 2011, **3**, 1159-1165.
208. M. T. Koper, *Journal of Solid State Electrochemistry*, 2013, **17**, 339-344.
209. L. An, J. Feng, Y. Zhang, Y.-Q. Zhao, R. Si, G.-C. Wang, F. Cheng, P. Xi and S. Sun, *Nano Energy*, 2019, **57**, 644-652.
210. J. Park, Y. J. Sa, H. Baik, T. Kwon, S. H. Joo and K. Lee, *ACS nano*, 2017, **11**, 5500-5509.
211. Y. Li, Z. Wang, J. Hu, S. Li, Y. Du, X. Han and P. Xu, *Advanced Functional Materials*, 2020, **30**, 1910498.
212. J. H. Montoya, L. C. Seitz, P. Chakthranont, A. Vojvodic, T. F. Jaramillo and J. K. Nørskov, *Nature materials*, 2017, **16**, 70-81.
213. I. C. Man, H.-Y. Su, F. Calle-Vallejo, H. A. Hansen, J. I. Martínez, N. G. Inoglu, J. Kitchin, T. F. Jaramillo, J. K. Nørskov and J. Rossmeisl, *ChemCatChem*, 2011, **3**, 1159-1165.
214. Z. W. Seh, J. Kibsgaard, C. F. Dickens, I. Chorkendorff, J. K. Nørskov and T. F. Jaramillo, *Science*, 2017, **355**, eaad4998.
215. X. Li, X. Hao, A. Abudula and G. Guan, *Journal of Materials Chemistry A*, 2016, **4**, 11973-12000.
216. A. Vojvodic and J. K. Nørskov, *National Science Review*, 2015, **2**, 140-143.
217. Z.-F. Huang, J. Song, Y. Du, S. Xi, S. Dou, J. M. V. Nsanzimana, C. Wang, Z. J. Xu and X. Wang, *Nature Energy*, 2019, **4**, 329-338.
218. C. L. Dong and L. Vayssieres, *Chemistry - A European Journal*, 2018, **24**, 18356-18373.
219. B. S. Yeo and A. T. Bell, *Journal of the*

- American Chemical Society*, 2011, **133**, 5587–5593.
220. Z. Chen, L. Cai, X. Yang, C. Kronawitter, L. Guo, S. Shen and B. E. Koel, *ACS Catalysis*, 2018, **8**, 1238–1247.
221. X. Su, Y. Wang, J. Zhou, S. Gu, J. Li and S. Zhang, *Journal of the American Chemical Society*, 2018, **140**, 11286–11292.
222. A. Deb, U. Bergmann, S. P. Cramer and E. J. Cairns, *Journal of applied physics*, 2006, **99**, 063701.
223. L. Huang, G. Gao, H. Zhang, J. Chen, Y. Fang and S. Dong, *Nano Energy*, 2019, **68**, 104296.
224. S. Zhao, C. Tan, C.-T. He, P. An, F. Xie, S. Jiang, Y. Zhu, K.-H. Wu, B. Zhang, H. Li, J. Zhang, Y. Chen, S. Liu, J. Dong and Z. Tang, *Nature Energy*, 2020.
225. C. Cao, D. D. Ma, Q. Xu, X. T. Wu and Q. L. Zhu, *Advanced Functional Materials*, 2019, **29**, 1807418.
226. H. Bin, J. Yao, Y. Yang, I. Angunawela, C. Sun, L. Gao, L. Ye, B. Qiu, L. Xue and C. Zhu, *Advanced materials*, 2018, **30**, 1706361.
227. J. W. Yoon, Y. K. Seo, Y. K. Hwang, J. S. Chang, H. Leclerc, S. Wuttke, P. Bazin, A. Vimont, M. Daturi and E. Bloch, *Angewandte Chemie International Edition*, 2010, **49**, 5949–5952.
228. X. Zheng, B. Zhang, P. De Luna, Y. Liang, R. Comin, O. Voznyy, L. Han, F. P. G. de Arquer, M. Liu and C. T. Dinh, *Nature chemistry*, 2018, **10**, 149.
229. N. Sivasankar, W. W. Weare and H. Frei, *Journal of the American Chemical Society*, 2011, **133**, 12976–12979.
230. W.-H. Li, W.-H. Deng, G.-E. Wang and G. Xu, *EnergyChem*, 2020, **2**, 100029.



Songsong Li

Songsong Li is a Ph. D candidate under the supervision of Prof. Lei Ge in College of New Energy and Materials of China University of Petroleum, Beijing (CUPB). At the same time, she is studying under the guidance of Prof. Pingyun Feng as a joint training student at the University of California, Riverside (UCR). Her research is focused on the design and synthesis of photocatalytic and electrocatalytic materials.



Yangqin Gao

Yangqin Gao is currently an Assistant Professor at the Department of Materials Science and Engineering, China University of Petroleum-Beijing (CUPB). He received his Ph.D. in Materials Science and Engineering from King Abdullah University of Science and Technology (KAUST), Saudi Arabia. His current research interests focus on the application of semiconductor photoelectrodes in photoelectrochemical water splitting and photoelectrocatalytic organic degradation



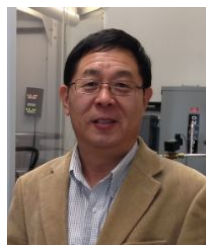
Ning Li

Ning Li is a lecturer in Department of Materials Science and Engineering, College of science, China University of Petroleum Beijing. She received her Ph.D. in Material physics and chemistry from Shanghai institute of Ceramics, Chinese Academy of Sciences in 2017. Her research interests include synthesis of 2D layered nanomaterials, their full-spectrum photocatalytic water splitting and chromic properties.



Lei Ge

Lei Ge received his B.S, M.S and Ph. D degrees in material from Tianjin University. He was a post-doctor of the University of California-Riverside from 2011 to 2012. In 2014, he become a Professor at China University of Petroleum-Beijing. His main research interests include novel photocatalytic functional materials, photocatalytic H₂ evolution and organic pollutant degradation and so on.



Xianhui Bu

Xianhui Bu received his Ph. D. in chemistry from State University of New York at Buffalo in 1992 with Philip Coppens. Between 1992 and 2003, he did his research with Galen Stucky at University of California Santa Barbara. He joined the Faculty at California State University Long Beach in 2003. His research area includes synthesis, crystal structure, and property characterization of crystalline porous materials.



Pingyun Feng

Pingyun Feng received her Ph. D. in Chemistry from University Santa Barbara in 1998 with Galen Stucky where she also did postdoctoral work at the Department of Chemical Engineering between 1998 and 2000 with David Pine. She joined the faculty at University of California Riverside in 2000. Her interest centers on the development of synthetic methodologies to prepare novel materials for energy conversion and storage.